NUMERICAL INVESTIGATION OF STATIC AND DYNAMIC STALL OF SINGLE AND FLAPPED AIRFOILS

A Thesis
Presented to
The Academic Faculty

by

Nicholas D. Liggett

In Partial Fulfillment
of the Requirements for the Degree
Doctor of Philosophy in the
School of Aerospace Engineering

Georgia Institute of Technology
December 2012

NUMERICAL INVESTIGATION OF STATIC AND DYNAMIC STALL OF SINGLE AND FLAPPED AIRFOILS

Approved by:

Dr. Marilyn J. Smith, Committee Chair
School of Aerospace Engineering
Georgia Institute of Technology

Dr. Olivier A. Bauchau
School of Aerospace Engineering
Georgia Institute of Technology

Dr. Mark Costello
School of Aerospace Engineering
Georgia Institute of Technology

Dr. Carlos E. S. Cesnik
Department of Aerospace Engineering
University of Michigan

Dr. Narayanan M. Komerath
School of Aerospace Engineering
Georgia Institute of Technology

Date Approved: August 24, 2012

TABLE OF CONTENTS

LIST OF TABLES

LIST OF FIGURES

CHAPTER I

NOMENCLATURE

a_1	=	Menter eddy viscosity parameter
arg_2	=	Blending parameter argument for Menter two-equation model
$C_{l,d,m}$	=	Two-dimensional lift, drag, pitching moment coefficients, respectively
C_ℓ	=	Turbulent $(kl)^{sgs}$ production constant
C_N	=	Total normal force coefficient
c	=	Airfoil chord
c_v	=	Constant volume specific heat
$C_{\varepsilon,k}$	=	Turbulent kinetic energy dissipation constant
C_ν	=	Eddy viscosity constant
e	=	Total energy
e_0	=	Internal energy
F_2	=	Blending parameter for Menter two-equation model
F_N	=	Integrated normal force on the cavity floor
h	=	Enthalpy
h_0	=	Total enthalpy
k	=	Kinetic energy, reduced frequency of oscillation
k^{sgs}	=	Turbulent kinetic energy
L	=	Length of the cavity in the streamwise direction
l^{sgs}	=	Sub-grid turbulent length scale
M_∞	=	Freestream Mach number
N	=	Current Newton subiteration
N_{sub}	=	Total number of Newton subiterations
n	=	Rossiter mode number, order of accuracy (superscript), iteration (subscript)
Pr	=	Prandtl number
p	=	Pressure
R	=	Universal gas constant
res	=	Residence periods

S_{ij}	=	Strain tensor
SPL	=	Sound pressure level, $p_{ref} = 2.0 \times 10^{-5} \mu$Pa
s	=	Nondimensional time, $s = U_\infty t/c$
s_{le}	=	Leading edge circumferential grid spacing
s_{max}	=	Circumferential maximum grid spacing
S_{ref}	=	Reference area for normal force coefficient calculation
s_{te}	=	Trailing edge circumferential grid spacing
T	=	Temperature, time steps/dynamic stall cycle $\times$ subiterations
t	=	Physical time
U_∞	=	Freestream flow velocity
u_i	=	Primitive velocity in the i-direction
$\tilde{u}_i$	=	Mass-weighted average flow speed in the i-direction
x_i	=	Physical coordinate in the i-direction
y	=	Distance to nearest surface
y^+	=	Distance to nearest surface in viscous length scales
α	=	Angle of attack, deg
α_0	=	Mean angle of attack, deg
β_1	=	Menter $k-\omega$ SST inner parameter
β^*	=	Menter $k-\omega$ SST turbulent kinetic energy destruction parameter
γ	=	Rossiter equation empirical parameter
γ^1	=	Menter $k-\omega$ SST turbulent dissipation inner production parameter
Δ	=	Grid length scale
Δt	=	Time step
$\Delta\alpha$	=	Angle of attack oscillation amplitude
δ_{ij}	=	Kronecker delta
ε	=	Turbulent dissipation, Percent error
κ	=	Menter $k-\omega$ SST parameter, Rossiter equation empirical parameter
μ	=	Molecular viscosity
ν	=	Kinematic viscosity

ν_t	=	Turbulent viscosity
ρ	=	Local flow density
ρ_∞	=	Freestream flow density
σ	=	Viscous work
σ_k	=	Prandtl-Schmidt number for turbulent kinetic energy
σ_{k1}	=	Menter turbulent kinetic energy inner Prandtl-Schmidt number
σ_{k2}	=	Menter turbulent kinetic energy outer Prandtl-Schmidt number
σ_{kl}	=	Prandtl-Schmidt number for $(kl)^{sgs}$
$\sigma_{\omega 1}$	=	Menter turbulent dissipation inner Prandtl-Schmidt number
$\sigma_{\omega 2}$	=	Menter turbulent dissipation outer Prandtl-Schmidt number
τ_{ij}	=	Resolved stress on the i-face in the j-direction
τ_{ij}^{sgs}	=	Sub-grid scale stress on the i-face in the j-direction
ϕ	=	Blended $k-\omega$ shear stress transport variable
Ψ_t	=	Turbulent terms to be linearly combined
Ω	=	Absolute value of the vorticity
ω	=	Turbulent dissipation rate, frequency of oscillation
$\overline{(.)}$	=	Mean quantity
$\widetilde{(.)}$	=	Mass-averaged quantity

CHAPTER II

SUMMARY

Separated flows about single and multi-element airfoils are featured in many scenarios of practical interest, including: stall of fixed wing aircraft, dynamic stall of rotorcraft blades, and stall of compressor and turbine elements within jet engines. In each case, static and/or dynamic stall can lead to losses in performance. More importantly, modeling and analysis tools for stalled flows are relatively poorly evolved and designs must completely avoid stall due to a lack of understanding. The underlying argument is that advancements are necessary to facilitate understanding of and applications involving static and dynamic stall.

The state-of-the-art in modeling stall involves numerical solutions to the governing equations of fluids. These tools often either lack fidelity or are prohibitively expensive. Ever-increasing computational power will likely lead to increased application of numerical solutions. The focus of this thesis is improvements in numerical modeling of stall, the need of which arises from poorly evolved analysis tools *and* the spread of numerical approaches. Technical barriers have included ensuring unsteady flowfield and vorticity reproduction, transition modeling, non-linear effects such as viscosity, and convergence of predictions.

Contributions to static and dynamic stall analysis have been been made. A hybrid Reynolds-Averaged Navier-Stokes/Large-Eddy-Simulation turbulence technique was demonstrated to predict the unsteadiness and acoustics within a cavity with accuracy approaching Large-Eddy-Simulation. Practices to model separated flows were developed and applied to stalled airfoils. Convergence was characterized to allow computational resources to be focused only as needed. Techniques were established for estimation of integrated coefficients, onset of stall, and reattachment from unconverged data. Separation and stall onset were governed by turbulent transport, while the location of reattachment depended on the mean flow. Application of these methodologies to oscillating flapped airfoils revealed flow through

the gap was dominated by the flap angle for low angles of attack. Lag between the aerodynamic response and input flap scheduling was associated with increased oscillation frequency and airfoil/flap gap size. Massively separated flow structures were also examined.

CHAPTER III

INTRODUCTION

Separated flows about single and multi-element airfoils are featured in many scenarios of practical interest. Some examples of these scenarios include: stall of fixed wing aircraft, dynamic stall of the flow about rotorcraft blades, and stall of compressor and turbine elements within jet engines. In each of these cases, static and/or dynamic stall could lead to a loss in performance. More importantly, modeling and analysis tools for stalled flows are poorly evolved when compared with similar tools for attached flows. The need to design to avoid scenarios involving stall is a direct result of a lack of modeling approaches. The underlying argument is that advancements in approaches are necessary to facilitate understanding of and applications involving static and dynamic stall.

Approaches that supply understanding of static and dynamic stall can be distilled into several categories. These categories include experiments, numerical predictions, and theoretical predictions. Each category complements the knowledge of the other categories. Experiments usually provide the most physically accurate representation of the flow. This accuracy can come at significant financial cost and time investment. Numerical predictions provide data on the entire flowfield, which can vastly improve understanding of stall. They also allow individual physical phenomena to be added and removed from models to assess their relative importance. However, numerical approaches can require large computational resources and adequate models must be developed. Finally, theory often provides the quickest turnaround for predictions and understanding of the trends resulting from the underlying physics; but, the simplifications required to make the problem tractable can make the results specific to only a small subset of applications.

The ever-increasing power of computers will likely lead to an increase in the application of numerical approaches. In light of poorly evolved static and dynamic stall predictive tools *and* an increased application of numerical approaches, the need for improved tools arises.

This thesis focuses on improving these numerical approaches. Physical phenomena of static and dynamic stall that should be considered were derived from literature on experiments. The methodology necessary for examining static and dynamic stall has been developed. Using this methodology, numerical predictions were carried out on single and multi-element airfoils with an emphasis on accurately reproducing the physics.

Technical barriers for numerical analysis of static and dynamic stall have included ensuring correct unsteady flowfield and vorticity reproduction, transition modeling, non-linear effects such as compressibility and viscosity, and numerical and physical convergence of predictions.

3.1 Static and Dynamic Stall

Research indicates that active control concepts have promise in mitigating numerous adverse phenomena associated with the aeromechanics of lifting surfaces. These techniques are being applied to delay stall of fixed wing aircraft, as well as to eliminate or mitigate vibratory loads, blade-vortex interaction, and dynamic stall of the flow about rotorcraft and wind turbine blades [2–8], These phenomena are nonlinear and unsteady for rotating systems, which add yet another layer of complexity on the physics of the flow. While a plethora of different active control techniques are being explored, the use of trailing edge flaps appears to be one of the more viable and cost-effective concepts.

Experimental studies have examined airfoils with flaps for both stationary [9–12] and oscillating [13] angles of attack. In addition to flow separation, the importance of other effects such as flow energy content and compressibility has been investigated. Petz [14] examined trailing edge flaps deployed on an airfoil at a static angle of attack with and without an active pulsed jet within the airfoil-flap gap. At high stalled angles of attack, excitation of the jet resulted in reattachment of the flow depending on the frequency of the jet. Not only the amount of separation, but also the frequency content of the separation is found to be important. Carr [15] observed shocks within gaps between leading edge slats and airfoils and noted that compressibility had a strong effect on downstream pressure distributions.

Experiments on static multi-element airfoils have shown that the turbulent flow within airfoil-control surface gaps is sensitive to many parameters [2, 3]. The jet-like flow emanating from the gaps injects additional turbulence and vorticity into the downstream flow over the main airfoil or the control surface. Using hot-wire and twin pulsed wire anemometry, Savory et al. [2] have quantified both the mean velocity and turbulence intensity within slat and flap gap flows over a range of static angles of attack. Flow through slat gaps was much more sensitive to angle of attack change than flow through flap gaps, but both the maximum turbulence intensity and the extent of the region of high turbulence in the gaps increase with angle of attack. Watanabe et al. [3] found that large-scale separation on the flap upper surface was primarily dependent on the flap deflection angle and the size of the flap gap, and secondarily on the Reynolds number. The separation was accompanied by a large recirculation region on the flap into which the energized turbulent flow from the component gap travels to influence the behavior about the entire airfoil.

The flow field within gaps has been characterized [16, 17] as detached shear layers that are unstable and roll up into vortices. These vortices may then impinge on the downstream gap wall, leading to a feedback loop where the vortices travel upstream against the gap wall back to their point of origination. This feedback loop bears striking resemblance to the feedback mechanism observed in cavity flows [18]. It is also one source of noise emanating from gaps. As these vortices are ejected from the gap, they alter the flow about the airfoil, which in turn modifies the flow within the gap.

A series of computational and experimental studies was performed on airfoils with both slats and flaps at NASA Langley Research Center [17, 19, 20]. Their efforts explored the source and prediction of airframe noise from the flow through airfoil component gaps. They also noted the importance of the detached shear layer and vortex instabilities in determining the flow physics, as well the need in computational simulations to accurately represent the geometry and sensitivity of vorticity within gaps to overly dissipative numerical schemes. Initial predictions by the authors used simplified sharp trailing edges for the component geometries rather than the actual finite trailing edges. The unsteadiness within the component gaps could not be captured with the simplified geometry as vortex shedding from

the finite trailing edges is an underlying mechanism of the flow unsteadiness. Moreover, the airframe noise was not accurately reproduced with dissipative fully turbulent unsteady Reynolds-Averaged Navier-Stokes (URANS) solvers employing the two-equation Menter $k\omega$ Shear Stress Transport (SST) turbulence model. The dissipative turbulence model was identified as an issue after significant grid refinement in the slat and variation of the numerical scheme did not improve correlations. Reproduction of experimental airframe noise was finally improved by the prescription of laminar regions within the vicinity of the gap. This greatly reduced dissipation, and resulted in a large region of recirculation with many discrete unsteady vortices within the slat. Recent experiments by Makiya et al. [21] confirmed these noise mechanisms studying a slat-airfoil configuration.

The jet-like flows emanating from airfoil component gaps also influence airfoil separation. Studies [22, 23] correlate stall hysteresis with the separation resulting from component gaps. Previous efforts to characterize the jet-like flows from gaps based on simple angles from the geometry were deemed insufficient. The characteristics of these jets require reproduction of the flow field about the entire airfoil including the gap. Batali [24] found that the surface pressure distribution far upstream near the suction peak can be affected by deflection of the trailing edge flap. A trailing edge flap can also lead to a confluent boundary layer on the upper surface [25] due to flow injection through the flap gap. This could alter sensitivities in regions where trailing edge flow reversal is important. Zhong et al. [26, 27] predicted the flow about a high-lift wing featuring a slat and flap. As with the aforementioned airframe noise predictions [17, 19, 20], large discrepancies can exist between experiments and simulations depending on the turbulence modeling technique of the predictions. Overly dissipative schemes do not correctly reproduce gap and flap upper surface vorticity obtained from experiments. Large-scale separation on the upper surface of the flap is suppressed with application of RANS techniques.

Modeling separated flows about airfoils is complex even for static angles of attack. Airfoils at static angles of attack beyond the linear regime have been well-studied [24, 28–30], but still present many challenges. Traditional unsteady Reynolds-Averaged Navier-Stokes (URANS) approaches model turbulence at all scales of the flow, and may not capture the

highly unsteady vortical flow field behind the airfoil observed by Wokoeck [28]. Strong vorticity within the gap between the airfoil and the flap must be reproduced if boundary layer behavior, separation, and drag are to be properly reproduced.

While a significant body of knowledge exists for static multi-element airfoils, data featuring oscillating multi-element airfoils is scarce. The strong influence of flap gap vorticity and fluid injection on the flow fields for static multi-element airfoils suggests oscillating airfoils will be similarly affected. The limited research that is available (e.g., [6, 31]) on oscillating multi-element airfoils does not investigate the physics within the component gaps, but rather provides only for integrated coefficients or pressure distributions.

The flow through gaps demands further attention as gaps on oscillating multi-element airfoils can leads to performance losses that have been documented as part of work by Boeing on the SMART rotor [32–35]. Data were compiled as part of a series of experiments that aimed to reduce rotor noise via active trailing edge flaps [32]. Kottapalli correlated a comprehensive analysis, which employs a structural model with airfoil tables, with these data [33, 34]. Several issues arose during this work by Kottapalli that indicated the need for computational fluid dynamics, such as sensitivity to the wake model and overall correlations that require improvement. Predictions by Potsdam, Fulton, and Dimanlig [35] on the SMART rotor explain some of the modeling difficulties. These predictions were carried out via two methods: comprehensive analysis with airfoil tables, and a loosely-coupled fluid/structural dynamics solver. The comprehensive analysis did not account for flap gap effects, while the coupled fluid/structural solver mesh had explicitly modeled flap gaps. Leakage of flow through the flap gaps between the upper and lower surface of the rotor occurred for the coupled solver. The flow through the gaps led to an increased collective pitch necessary for the SMART rotor to attain the same lift as an equivalent rotor with no gaps. Compared to this no-gap rotor at the same lift, the SMART rotor lift production moved from the outboard to the inboard portion of the rotor, the blades had increased chord-wise forces, and there was an additional nose-down pitching moment component on the blade. Other problems included convergence, efficiency, smoothness, and accuracy of the solutions, which were also all adversely affected. Reduction in performance due to leakage

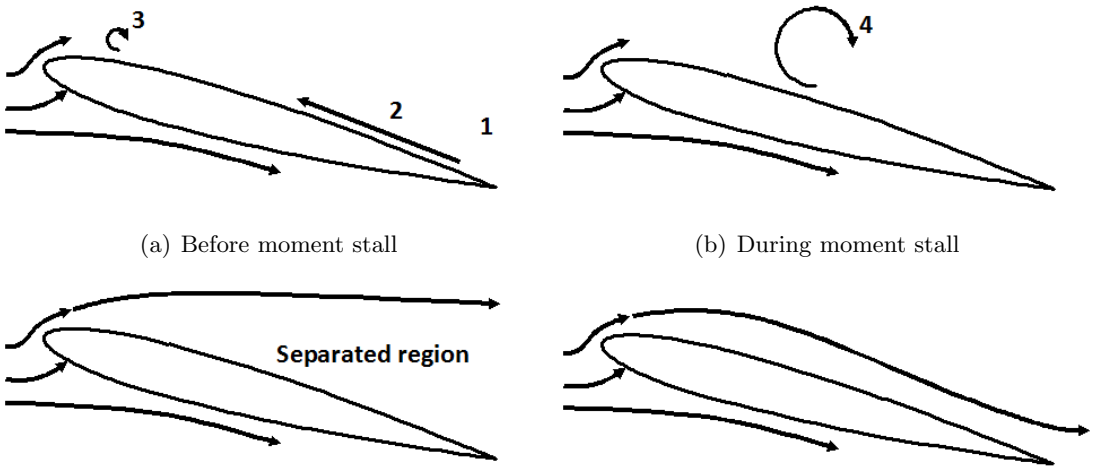

(a) Before moment stall

(b) During moment stall

(c) Fully stalled upper surface

(d) Reattached flow

Figure 1: Example flowfield during dynamic stall.

across gaps is not unique to the SMART rotor and has been observed by other authors on similar geometries [36].

Dynamic stall was examined by McCroskey [37] and Carr [38]. The flowfield generally involves the sequence of phenomena of reversal, vortex shedding, and full separation (Fig. 1). Reversal often begins near the trailing edge during the upstroke, as indicated by point 1 (Fig. 1(a)). The region of flow reversal travels up the surface of the airfoil along the path labeled as point 2 (Fig. 1(a)) with larger eddies appearing in the boundary layer. These events occur as the lift increases before a large increase in negative moment. A vortex forms near the leading edge at point 3 as the angle of attack further increases (Fig. 1(a)). This vortex grows and travels downstream along the upper surface as diagrammed in point 4 (Fig. 1(b)). As the vortex completes its passage the airfoil reaches a fully stalled state and the lift drops.

It is important to note that this chronology is generally associated with dynamic stall, but there are competing mechanisms involved including laminar bubble bursting and leading edge shocks [38, 39]. As outlined by Carr [38] even relatively low Mach number flows can reach supersonic conditions over the leading edge of an oscillating airfoil. The effect of trailing edge flaps on the pressure distribution on the upper surface of the airfoil can be significant.

Three-dimensional effects are also known to be important as demonstrated by three-dimensional dynamic stall experiments on a rotor blade [40]. The three-dimensional structure of the flow during dynamic stall was carefully captured by imaging techniques. Repeating stall cells were observed with the spacing of these cells equal to the height of the dynamic stall events. Any modeling and analysis techniques should be three-dimensional.

3.2 Modeling Unsteady Flowfield Physics

The modeling of separated flows about airfoils is more complex than attached flows even for static angles of attack. Airfoils at static angles of attack beyond the linear regime through stall have been well-studied [24, 28, 29, 41], but still present many challenges. Traditional unsteady Reynolds-Averaged Navier-Stokes (URANS) approaches model turbulence at all scales of the flow, and may not capture the highly unsteady vortical flowfield behind the airfoil as demonstrated by Wokoeck [28]. Over prediction of the maximum lift coefficient was associated with a delay in stall and higher pressure peaks than encountered in experiments.

The studies by Wokoeck focused on single element airfoils, whereas trailing edge flaps have long been employed to improve performance. This presents additional challenges as the trailing edge flap can significantly affect onset of stall and post-stall behavior. For example, the surface pressure distribution far upstream near the suction peak can be affected by deflection of the trailing edge flap [24]. A trailing edge flap can also lead to a confluent boundary layer on the upper surface [25] due to flow injection through the flap gap. The could alter sensitivities in regions where trailing edge flow reversal is important. Strong vorticity within the gap between the airfoil and the flap must be reproduced if boundary layer behavior, separation, and drag are to be properly reproduced.

The highly unsteady flow characterized by strong vorticity present in static and dynamic stall may be paralleled to cavities, which although geometrically simple provide similar, complex flow phenomena. The intricacies present in cavity flows include a detached shear layer, vortex growth, and acoustics. Komerath [42] extensively surveyed existing cavity studies in 1987. Cavities were classified based on the type of fluid interactions observed in the cavities: fluid dynamic, fluid-resonant, or fluid-elastic. Cavities below a certain

threshold or cavities with a low free-stream Mach number were immune from oscillations and resonance. Cavities with harmonic oscillations were categorized based on: the modal traits, the frequency in relation to the geometry and Mach number, and the boundary or shear layer characteristics. The speed of sound within a cavity was best approximated by the stagnation speed of sound, rather than the free speed of sound. This modifies the frequencies of any harmonic modes. Accurate modeling of the physics of separated flow cavities can provide a baseline methodology for the modeling of stall flows.

Using Large-Eddy Simulation (LES), Levasseur [18] captured unsteady flow physics within a 0.508 m long, 0.1016 m deep, and 0.1016 m wide cavity at a Mach number of 0.85 and Reynolds number of 7 million (using the cavity length as the reference length). Capability of LES to capture unsteady physics was demonstrated by reproducing harmonic modes between 350 and 900 Hz in terms of the amplitudes and frequencies to within 3% of values obtained from experiments by Henshaw [1]. The inability of differing unsteady RANS approaches to capture the unsteady physics of the experiments by Henshaw to the same degree as LES was observed in simulations by Allen [43] and Syed [44]. The predictive power of LES in capturing unsteady physics comes at the price of up to two orders of magnitude increase in the required computational resources [45].

Hybrid Reynolds-Averaged Navier-Stokes/Large-Eddy Simulation (RANS/LES) techniques such as the method of Sanchez-Rocha [29] blend RANS and LES models with the goal of obtaining the accuracy of LES and the lower costs of RANS. In simulations by Sanchez-Rocha this approach captured surface pressure distributions and vorticity in the separated regions of a stall airfoil more accurately than traditional unsteady RANS. This accuracy was attributed resolution of large scale turbulent eddies and modeling of the subgrid-scales. Improved post-stall predictions of NACA0015 airfoil loads demonstrated the need for three-dimensional simulations with advanced turbulence modeling within the separated flow regime. This thesis will expand the work of Sanchez-Rocha by capturing unsteady physics of the Henshaw experimental cavity case. Subsequently, the hybrid technique was employed in predictions of separated airfoils and gaps.

3.3 Numerical Techniques and Convergence

Computation of rotor/wing flows, characterized by viscous unsteady flow and body motion, requires a simulation based on the unsteady Navier-Stokes equations. These equations are usually simulated discretely using the unsteady Reynolds-Averaged Navier-Stokes model equations, Large Eddy Simulations or some hybrid of the two. In this process, temporal integration is achieved using either implicit or explicit techniques. Explicit methods can be less expensive than implicit methods for a single time step, but often have strict stability requirements characterized by the Courant-Friedrichs-Lewy (CFL) number. Implicit methods are advantageous as the time step can be determined by flow features or motion of the configuration, rather than the stability limits of the solver. Implicit methods incur penalties during the costly inversion of very large matrices. The addition of a pseudo-time derivative of the vector of conserved field variables added to the Navier-Stokes equations [46–48] avoids direct matrix inversion and applies iterative methods to converge the pseudo-time derivative to zero. When this convergence is achieved, the physical time derivatives are obtained.

Many current codes employ fixed point Newton subiterations [49] at each physical time step to advance the solver in time and to increase the nominal order of the temporal accuracy [50, 51]. For a given time step, Δt, where $t_{n+1} = t_n + \Delta t$, as the number of subiterations is increased, the equations will converge to the solution at t_{n+1}, provided stability requirements of the problem are met. The required number of subiterations to reach convergence is sensitive to many parameters, such as the initial guess, step size, and governing equation type. Typically, URANS codes will include separate fixed-point iterations for any turbulence quantities that are modeled, such as kinetic energy and dissipation rate. It has been demonstrated that convergence of the turbulence terms and convergence of the mean flow terms have limited correlation [52], so that separated fixed-point iteration loops are necessary to avoid wasted resources. Unfortunately, a methodology for assessing or understanding the relative importance of the differing terms is lacking.

In prior efforts, Rumsey et al. [47] explored subiteration strategies and established convergence characteristics of second-order accurate temporal integration schemes for attached

transonic flows. Their efforts were also limited to simulations that applied the one-equation Spalart-Allmaras turbulence model.

A series of static and dynamic stall numerical studies by European rotorcraft researchers [53–58] have analyzed grids, spatial convergence, and turbulence models for two-dimensional airfoils. Early efforts [53, 54] focused primarily on grid dependence for static stall with several turbulence models. Costes [55] achieved the closest grid independent solution, which revealed non-physical flow phenomena even though the solutions appeared to be converged. These phenomena included chord-wise oscillations in the suction peaks and skin friction profiles resembling transition that were strictly numerical effects.

Subsequent dynamic stall evaluations [56, 57] identified boundary layer reattachment as the feature most sensitive to spatial and temporal resolution. Based on visual inspection of stall onset and flow reattachment, they recommended 360,000 time steps/cycle $\times$ subiterations for convergence. Klein, Richter, and Altmikus [58] reaffirmed the sensitivity of reattachment to time step size and recommended 1000 to 2000 time steps per cycle with 100 subiterations for temporal convergence.

Morton et al. [59], who examined the time-accurate vortex shedding from an aircraft wing in stall with detached eddy simulations (DES) utilized flow field power spectra of turbulence content at selected flow field locations to visually confirm temporal convergence. They found one hundred time steps to traverse the reference chord, along with an unspecified number of Newton subiterations was sufficient for convergence.

Studies such as these have typically presented their results in disparate ways, demonstrating one of the shortcomings of the understanding of convergence: there is no systematic method of analysis that may be applied to a variety of phenomena or an estimation of the requirements of convergence. Efforts are typically focused on qualitative and some quantitative determinations of convergence for a particular parameter usually only as a step to other purposes. Sources of error are outlined by authors, including the previously mentioned non-physical artifacts, delay in separation or reattachment, transition, or turbulence model deficiencies. These error sources are often the item of interest, rather than convergence.

To date, temporal convergence of static and dynamic stall simulations has been established via qualitative assessment of various integrated performance parameters and/or select flow field quantities. With the advent of advanced turbulence techniques such as DES and hybrid RANS/LES, the behavior between these methods and the traditional RANS turbulence models during temporal convergence should also be assessed. This thesis examines the temporal behavior and convergence characteristics of static and dynamic time-accurate airfoil simulations using the RANS Menter $k\omega$-Shear Stress Transport (SST) model [60] and a hybrid RANS/LES technique [29, 61] based on the same RANS model.

3.4 Transition to Turbulence

Transition to turbulence is one aspect of airfoil flows that has been demonstrated to be important in prediction of stall [41]. Improper prediction of boundary layer energy can lead to delay in onset of stall. Studies by Shelton employing unsteady RANS on SC1095 and NACA0012 airfoils with the inclusion of Michel's criterion [62] to model laminar to turbulent transition improved predictions of post-stall integrated coefficients. This warrants the use of transition modeling for airfoils.

Transition occurs as the Reynolds number of an initially laminar flow increases. Disturbances created by discontinuities in the geometry, freestream turbulence, and other sources are damped by relatively strong viscosity as low Reynolds numbers. At higher Reynolds numbers, strong inertial forces lead to magnification of instabilities and result in turbulent flow.

An example of transition occurring on an airfoil is diagrammed in Fig. 2. As the body travels through the flow, the fluid moving towards the airfoil slows and stops at the leading edge stagnation point. The flow then accelerates over the top and bottom of the geometry. Between the stagnation point and the transition points, the fluid is stable and laminar. Downstream the transition point, the fluid slowly transitions to fully turbulent.

Proper prediction of both static and dynamic stall may require explicit transition modeling. As outlined in Schlichting[63], transition leads directly to a change in the shape of the boundary layer profile. Drag is directly proportional to the tangential velocity gradient

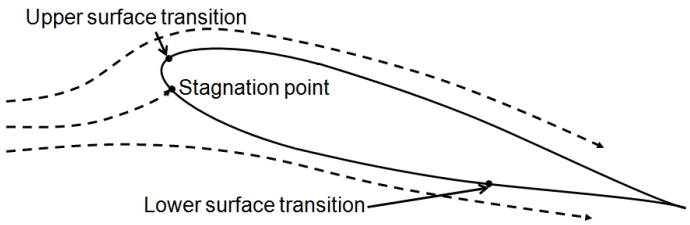

Figure 2: Transition on an airfoil.

at the surface of a geometry. The initial laminar flow over a plate or airfoil will have a different drag value than the turbulent flow after transition. Incorrect drag may result if a fully turbulent flow over the entire geometry is assumed.

The shape of the velocity profile is also an indication of the kinetic energy in the boundary layer. Improper reproduction of this profile leads to fluid with too much or too little energy. Incorrect prediction of separation follows this incorrect prediction of boundary layer energy. Proper thrust calculation requires both accurate drag and precise stall correlations. This necessitates transition modeling.

Popular e^N-methods [64, 65] are transition criteria based on local, linear stability theory, and the parallel flow assumption. It is one of the commonly used models in research. This method correlates separation with experimental data via the shape factor, Reynolds number with the displacement thickness as the reference length, and reduced frequency of the Tollmien-Schlichting waves. Cross flow and Tollmien-Schlichting instabilities can be modeled with these methods.

Complexity of e^N-methods makes inclusion into already existing code bases a prohibitive process. Other empirical methods exist which focus on direct correlation with experimental data, rather than modeling the transition processes. Michel's criterion is one such model [62] that is discussed in the Development section. This model provides a relatively inexpensive alternative to e^N-methods that may implemented into an already existing code base.

3.5 Objectives

The objective of this thesis is to enhance numerical techniques for predicting separated and stalled flows and to contribute to the understanding of these flows. This work has advanced

the state-of-the-art as follows:

1. A hybrid RANS/LES turbulence technique predicted the unsteady physics and acoustics within a cavity with accuracy approaching the level of LES without the associated costs. Best practices to reproduce the highly unsteady flow were developed and applied to separated flows about airfoils.

2. Characterization of convergence and novel convergence criteria will allow computational resources to be focused as needed. Prediction of integrated coefficients, onset of stall and reattachment is now possible from unconverged data. Separation and stall onset were governed by turbulent transport equations, while the location of reattachment depended on the mean flow equations.

3. The numerical methodology established herein was applied to flapped oscillating airfoils. Phase shifts appeared in the lift coefficient hysteresis as lags between the flap deflection angle input scheduling and lift response of the airfoil. The phase angle increased with increasing gap size and increasing flap oscillating frequency.

CHAPTER IV

METHODOLOGY

4.1 Baseline Solver

In order to study the flowfield around static and dynamic bodies, numerical integration of the fluid transport equations through time is carried out with consideration to temporal parameters, transition, and acoustics. Accuracy of solutions are assessed in the form of the integrated forces and moment coefficients, as well as the ability of the methodology to accurately reproduce sound pressure levels for known configurations. To this end, the fully compressible mass, momentum, energy, and turbulence conservation equations are solved using an implicit finite-difference scheme and integrated in a time-accurate manner with the fully viscous Navier-Stokes flow solver OVERFLOW [66, 67]. OVERFLOW is capable of time-accurate simulations of complex geometries with many elements that may move relative to each other with any desired motion.

An overset grid approach is utilized where several structured grids are used to simulate complex geometries, combining body-fitted near-body grids with background grids to cover the entire domain of interest. For these overlapping grids, nodes existing within solid geometry (e.g. background nodes overlapping an airfoil) are removed with the hole cutting algorithm outlined by Meakin [68].

Points on the interior of the meshes are solved in a conventional manner with the conservation equations. The conserved field variables at any nodes lying on the boundary of the holes or the outer edges of overlapping grids are interpolated from surrounding grids. At physical features, such as viscous walls or far-field inlets, standard boundary conditions are used as outlined in each case.

The governing equations solved by OVERFLOW [69] are outlined. The Navier-Stokes equations may be written in vector form with respect to a generalized coordinate system as

$$\frac{\partial \overrightarrow{q}}{\partial t} + \frac{\partial \overrightarrow{E}}{\partial \xi} + \frac{\partial \overrightarrow{F}}{\partial \eta} + \frac{\partial \overrightarrow{G}}{\partial \zeta} = 0 \tag{1}$$

The generalized coordinates are ξ, η, and ζ, whereas the fluxes in each direction are denoted as $\overrightarrow{E}$, $\overrightarrow{F}$, and $\overrightarrow{G}$. The vector of conserved scalars is

$$\frac{\overrightarrow{q}}{V} = \begin{bmatrix} \rho \\ \rho u_1 \\ \rho u_2 \\ \rho u_3 \\ \rho e_0 \end{bmatrix} \tag{2}$$

Here, ρ, $\vec{u}$, p, and e are the unknown field variables of density, velocity in each of the three Cartesian directions, pressure, and total energy per unit mass, respectively, over the control volume V. These equations are linearized and a pseudo-time term is added to allow sub-iteration and faster iterative numerical schemes to be employed. The resulting system is

$$\left[I + \frac{\Delta t}{(1+\theta)\,\Delta\tau} + \frac{\Delta t}{1+\theta}\left(\partial_\xi A + \partial_\eta B + \partial_\zeta C\right)\right]\Delta q^{n+1,m+1} = \tag{3}$$

$$-\left[\left(q^{n+1,m} - q^n\right) - \frac{\theta}{1+\theta}\Delta q^n + \frac{\Delta t}{1+\theta} RHS^{n+1,m}\right] \tag{4}$$

To provide second-order temporal accuracy $\theta = 1/2$ is used in this study. The fluxes create the right-hand side term as

$$RHS = \frac{\partial \overrightarrow{E}}{\partial \xi} + \frac{\partial \overrightarrow{F}}{\partial \eta} + \frac{\partial \overrightarrow{G}}{\partial \zeta} \tag{5}$$

With five equations and six unknowns, a state equation is needed to close the system. Using the perfect gas assumption, the internal energy per unit mass can be related to the temperature by

$$e_0 = c_v T \tag{6}$$

The proportionality constant is c_v, the specific heat at constant volume. The internal energy per unit mass is now related to the total energy per unit mass using tensor notation for repeated indices by

$$e = e_0 + \frac{1}{2} u_k u_k \tag{7}$$

Finally, the system of equations is now closed using the state relation

$$p = \rho R T \tag{8}$$

4.2 Turbulence Approach

The governing equations could be solved with no further analysis using discretization methods with appropriate integration and boundary conditions. Unfortunately, such an approach would likely lead to the need of tremendous amounts of computer resources to resolve even a small control volume of interest. To alleviate the necessity for such a restrictive grid, the turbulent length scales can be split into resolved and unresolved regimes. The resolved portions may be solved with a grid fine enough to reproduce the flow features, while the unresolved parts may be modeled to reduce computational requirements of the problem. The unresolved subgrid-scale stresses use an eddy viscosity model and are calculated from

$$\tau_{ij}^{sgs} = 2\bar{\rho}\nu_t \left(\tilde{S}_{ij} - \frac{1}{3}\tilde{S}_{kk}\delta_{ij} \right) - \frac{2}{3}\bar{\rho}k^{sgs}\delta_{ij} \tag{9}$$

The turbulent eddy viscosity, ν_t, and the turbulent kinetic energy, k^{sgs}, can be calculated using one of several turbulence approaches. Several different two-equation techniques are employed for closure of the turbulence modeling in this study.

4.2.1 Menter $k-\omega$ SST

A popular turbulence closure model is the Menter $k-\omega$ SST (shear stress transport) two-equation model [60], developed as an alternative to the standard $k-\omega$ model [70], which transports the turbulent kinetic energy, k, and turbulent dissipation rate, ω, via the following transport equations:

$$\frac{\partial \rho k}{\partial t} + \frac{\partial \rho u_j k}{\partial u_j} = \tau_{ij}\frac{\partial u_i}{\partial x_j} - \beta^* \rho \omega k + \frac{\partial}{\partial x_j}\left[(\mu + \sigma_k \mu_t)\frac{\partial k}{\partial x_j} \right] \tag{10}$$

$$\frac{\partial \rho \omega}{\partial t} + \frac{\partial \rho u_j \omega}{\partial u_j} = \frac{\gamma}{\nu_t}\tau_{ij}\frac{\partial u_i}{\partial x_j} - \beta \rho \omega^2 + \frac{\partial}{\partial x_j}\left[(\mu + \sigma_\omega \mu_t)\frac{\partial \omega}{\partial x_j} \right] + 2(1-F_2)\rho\sigma_{\omega 2}\frac{1}{\omega}\frac{\partial k}{\partial x_j}\frac{\partial \omega}{\partial x_j} \tag{11}$$

The constants are calculated by the blending function, ϕ, where

$$\phi = F_2\phi_1 + (1-F_2)\phi_2 \tag{12}$$

and the blending parameter is

$$F_2 = tanh\left(arg_2^4 \right) \tag{13}$$

$$arg_2 = max\left(2\frac{\sqrt{k}}{0.09\omega y}; \frac{500\nu}{y^2\omega}\right) \tag{14}$$

where y is the distance to the nearest viscous surface. The turbulent eddy viscosity is computed from

$$\nu_t = \frac{a_1 k}{max\left(a_1\omega; \Omega F_2\right)} \tag{15}$$

where Ω is the absolute value of the vorticity with $a_1 = 0.31$. The SST inner variables are $\sigma_{k1} = 0.85$, $\sigma_{\omega 1} = 0.5$, $\beta_1 = 0.0750$, $\beta^* = 0.09$, and $\kappa = 0.41$. The turbulent dissipation inner production parameter is

$$\gamma_1 = \frac{\beta_1}{\beta^*} - \sigma_{\omega 1}\frac{\kappa^2}{\sqrt{\beta^*}} \tag{16}$$

The outer layer constants include $\sigma_{k2} = 1.0$, $\sigma_{\omega 2} = 0.856$, $\beta_2 = 0.0828$, $\beta^* = 0.09$, and $\kappa = 0.41$. The turbulent dissipation outer production parameter is computed as

$$\gamma_2 = \frac{\beta_2}{\beta^*} - \sigma_{\omega 2}\frac{\kappa^2}{\sqrt{\beta^*}} \tag{17}$$

4.2.2 DES (DES-SST)

The detached eddy simulation (DES) approach [71] relies on a redefinition of the length scale used in the Menter $k-\omega$ SST equations for dissipation of the turbulent kinetic energy. The length scale of the Menter $k-\omega$ SST model in terms of the transport variables is

$$l = \frac{k^{\frac{1}{2}}}{\beta^*\omega} \tag{18}$$

In DES, the length scale is recomputed as

$$l_{DES} = \min\left[l, C_{DES}\max\left(\Delta x, \Delta y, \Delta z\right)\right] \tag{19}$$

Here, C_{DES} is blended using the Menter blending function (Eqs. 12-14), where $C_{DES_1} = 0.78$ and $C_{DES_2} = 0.61$. This new definition alters the turbulent kinetic energy dissipation term from $D^k = \rho\beta^* k\omega = \rho k^{3/2}/l$ to $D^k = \rho k^{3/2}/l_{DES}$. The effect of this change is an increase in the turbulent kinetic energy dissipation in regions where the grid size is smaller than the estimated turbulent length scales, allowing the solver to resolve rather than model larger eddies.

4.2.3 Hybrid RANS-LES (GT-HRLES)

The GT-HRLES [29] and DES-SST techniques both employ the Menter $k-\omega$ SST base model, but utilize differing approaches for the unresolved turbulence. This method uses the subgrid length scale as a filter and explicitly blends the kinetic energy of the two-equation SST model with a one-equation subgrid-scale kinetic energy model using the Menter blending function. This differs from the DES-SST method which redefines the length scale as a filtering method, but uses the Menter equations to perform this subgrid modeling. The GT-HRLES approach was added to OVERFLOW 2.0y by Shelton [72] and originally relied on a DES-like assumption. This work extends the implementation to include the subgrid-scale turbulence model as formulated by Sanchez-Rocha [29]. Beginning with the Menter two-equation $k-\omega$ SST formulation as given in Eqns. 10 and 11 for the transport of turbulent kinetic energy and dissipation, respectively, the addition of a an LES turbulent kinetic energy equation gives

$$\frac{\partial \bar{\rho} k^{sgs}}{\partial t} + \frac{\partial \bar{\rho} \tilde{u}_i k^{sgs}}{\partial u_i} = \tau_{ij}^{sgs} \frac{\partial \tilde{u}_i}{\partial x_j} - C_\varepsilon \bar{\rho} \frac{(k^{sgs})^{3/2}}{\bar{\Delta}} + \frac{\partial}{\partial x_i} \left[\bar{\rho} \left(\frac{\nu}{Pr} + \frac{\nu_t}{Pr_k} \right) \frac{\partial k^{sgs}}{\partial x_i} \right] \tag{20}$$

Here, the eddy viscosity is

$$\nu_t = C_\nu \bar{\Delta} \sqrt{k^{sgs}} \tag{21}$$

The length scale is

$$\bar{\Delta} = (\Delta x \Delta y \Delta z)^{\frac{1}{3}} \tag{22}$$

The turbulent terms of the Menter $k-\omega$ SST and the LES turbulent kinetic energy terms may be linearly combined [73] to form

$$\Psi_t = F_2 \Psi_t^{RANS} + (1 - F_2)\, \Psi_t^{sgs} \tag{23}$$

The blending function F_2 is defined in Eqn. 13.

4.2.4 LES-VLES (KES)

The last addition to OVERFLOW is the LES-VLES (KES) turbulence technique, developed by researchers at Georgia Tech [74, 75] and implemented in the OVERFLOW 2.0y code by Shelton [72] and added to the 2.1z version by the author, which resolves two k and kl

turbulence equations, and provides an approach that adjusts and may resolve scales when grids are employed in Direct Numerical Simulation up to very Large-Eddy Simulation. This approach differs from the other approaches in that it directly calculates the length scale, rather than relying on the grid spacing. The Favre filtered transport equations are for the subgrid k^{sgs} and $(kl)^{sgs}$ are

$$\frac{\partial \bar{\rho} k^{sgs}}{\partial t} + \frac{\partial \bar{\rho} \tilde{u}_i k^{sgs}}{\partial u_i} = \tau_{ij}^{sgs} \frac{\partial \tilde{u}_i}{\partial x_j} - C_{\varepsilon,k} \bar{\rho} \frac{(k^{sgs})^{3/2}}{l^{sgs}} + \frac{\partial}{\partial x_i} \left[\bar{\rho} \left(\frac{\nu}{Pr} + \frac{\nu_t}{\sigma_k} \right) \frac{\partial k^{sgs}}{\partial x_i} \right] \tag{24}$$

$$\frac{\partial \bar{\rho} (kl)^{sgs}}{\partial t} + \frac{\partial \bar{\rho} \tilde{u}_i (kl)^{sgs}}{\partial u_i} = C_l l^{sgs} \tau_{ij}^{sgs} \frac{\partial \tilde{u}_i}{\partial x_j} - C_{\varepsilon,kl} \bar{\rho} (k^{sgs})^{3/2} + \frac{\partial}{\partial x_i} \left[\bar{\rho} \left(\frac{\nu}{Pr} + \frac{\nu_t}{\sigma_{kl}} \right) \frac{\partial (kl)^{sgs}}{\partial x_i} \right] \tag{25}$$

These equations give the subgrid velocity scale, $(k^{sgs})^{1/2}$, and the subgrid length scale l^{sgs}. The constants used for these equations are set to $C_{\varepsilon,k} = 0.916$, $C_l = 1.06$, $\sigma_k = 0.9$, $\sigma_{kl} = 2$. The dissipation coefficient for $(kl)^{sgs}$ is

$$C_{\varepsilon,kl} = 0.58 + 2 \frac{C_\nu}{\sigma_{kl}} \left(\frac{\partial l^{sgs}}{\partial x_j} \right)^2 \tag{26}$$

where the eddy viscosity constant is $C_\nu = 0.0067$.

CHAPTER V

TRANSITION

5.1 Purpose

The addition of transition modeling to the flow solver must be verified through correlation with analytical and experimental data. Analytical solutions are of the flow over a flat plate provide an excellent opportunity to study in detail the various boundary layer distributions, determining if computational results match expectations. Beyond flat plate flows, the NACA 0012 airfoil is considered in terms of transition location and performance variation with angle of attack. As outlined previously, transition can greatly affect the energy of the flow in the boundary layer. The boundary layer shape is directly related to the separation location, making transition an important phenomenon for the prediction of the stall location on the airfoil, stall angle, maximum lift, and flowfield in regime near stall. Even before stall, large initial laminar regions on the airfoil can greatly alter the viscous drag on the airfoil, meaning any simulations must account for transition to correctly predict the integrated viscous coefficients.

5.2 Computational Setup

Transition is modeled via Michel's criterion [62]. This method was chosen due to its low computational cost. Despite the low cost, the correlations maintain an acceptable level of accuracy. The Michel criterion is based on experimental correlation of the local Reynolds number and momentum thickness Reynolds number with the transition point. Transition onset takes place where

$$Re_{\theta,tr} = 1.174\left(1 + \frac{22400}{Re_{x,tr}}\right) Re_{x,tr}^{0.46} \tag{27}$$

The local Reynolds number using the distance from the stagnation point as the reference length is

$$Re_{x,tr} = \frac{u\rho x}{\mu} \tag{28}$$

Here, x is the distance along the airfoil surface from the stagnation point to the testing point for transition. The momentum thickness of the boundary layer is

$$\theta = \int_0^\infty \frac{u\rho}{(u\rho)_{edge}} \left[1 - \frac{u\rho}{(u\rho)_{edge}}\right] dy \tag{29}$$

The Reynolds number using the momentum thickness as the reference length is

$$Re_{\theta,tr} = \frac{u\rho\theta}{\mu} \tag{30}$$

The surface of the body of interest (e.g. airfoil, flat plate) is traversed. The stagnation point is determined for the case of an airfoil as the reference point, or the leading edge for the case of a flat plate. At each computation node the Reynolds numbers are calculated and Michel's criterion is assessed. Once satisfied turbulence is tripped and further downstream nodes are considered turbulent. For the case of a flat plate one transition point exists, whereas for the case of an airfoil there are transition points on both the upper and lower surfaces. Once turbulence is tripped an intermittency calculation is performed via using the method of Chen and Thyson [76] with modifications by Cebeci [77]. This intermittency is multiplied by the turbulent eddy viscosity to give a smooth transition region from laminar to fully turbulent flow.

$$\gamma = 1 - \left(\frac{u_{edge}^3}{\nu^2 G}\right) Re_{x,tr}^{-1.34} (x - x_{tr}) \int_{x_{tr}}^{x} \frac{dx}{u_{edge}} \tag{31}$$

Where,

$$G = 71 \left[\log_{10}(Re_{x,tr}) - 4.7323\right] \tag{32}$$

Implementation of Michel's criterion is validated through flat plate with a zero pressure gradient and NACA 0012 simulations. Comparisons are carried out between fully laminar flows, fully turbulent flows, and free transition flows with transition modeled via Michel's criterion. Turbulence is modeled using the Menter $k - \omega$ SST and HRLES turbulence techniques.

Application of Michel's criterion to a NACA 0012 airfoil has been performed in by other authors [41, 78, 79]. These studies demonstrate applicability of Michel's criterion at low angles of attack. As the angle of attack is increased, surface curvature and strong pressure

gradients lead to errors between the predictions and experiment. Transition in this study is examined at a Reynolds number of 3 million and static angles of attack of 0, 3, 5, 8, and 10°. A normalized time step of $\Delta t = 0.0025$ with 10 Newton sub-iterations provided the necessary residual drop and second-order temporal accuracy. Spatial derivatives were approximated by centrally-differenced fourth-order accurate Euler discretizations. Temporal integration was carried out via the ARC3D diagonalized Beam-Warming scalar pentadiagonal scheme with a generalized thin-layer Navier-Stokes (TLNS3D) scheme used to smooth the enthalpy. The second and fourth-order smoothing coefficients were 2.0 and 0.04, respectively, respectively. No hole cutting or overset grid fringing was necessary for these transition validation cases.

The integrated lift, drag, and moment as a function of angle of attack for each NACA 0012 flow assumption case are compared against experimental values. From previous studies it is expected that the free transition drag is lower than the fully turbulent drag and closer to experiment. The effect of free transition on the pressure coefficient distribution over the airfoil surface is determined by comparison with experiment. Differences in drag due to transition are further highlighted by the study of skin friction distributions.

5.3 Flat Plate Grid

The flat plate mesh is two-dimensional with 110 nodes in the stream-wise direction with clustering near the edges and 101 nodes in the normal direction (Fig. 3). The first 19 nodes occur before the plate with the plate beginning at node 20. The simulation domain extends 1 plate length in the vertical direction. Viscous grid spacing is $y^+ < 1$ and grid stretching is maintained below 10%.

The boundary layer thickness at a Reynolds number of 3 million on the flat plate differs greatly between laminar and turbulent flow (Fig. 4). Analytically, the turbulent boundary layer increases with an inverse power-law profile, whereas the laminar boundary layer increases with the inverse of the square root of the Reynolds number, and turbulent boundary layer thickening is much more rapid owing to more effective convective mixing processes. For transition via Michel's criterion, the boundary layer thickness increases following the laminar curve until transition begins to occur at $x_{cr}/L = 0.413$, corresponding to a Reynolds

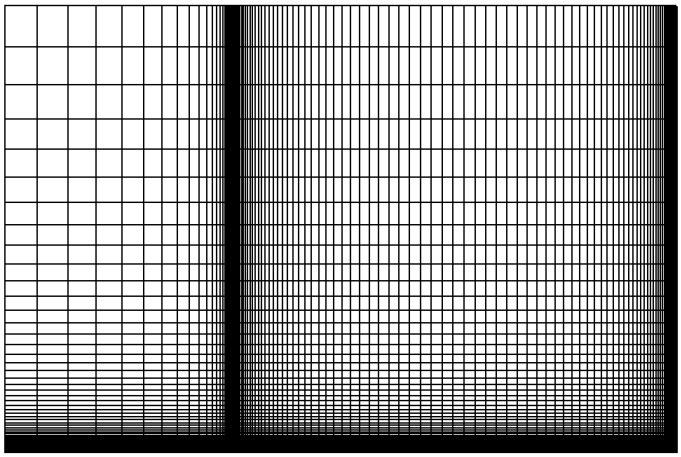

Figure 3: Flat plate mesh for transition verification.

number of 1.24 million and fitting experimental observations. The flow transitions to turbulent and the boundary layer begins thickening following a similar inverse power-law pattern as the fully turbulent flow.

Comparison of the fully turbulent profile with the analytical values gives errors of less than 6% for most of the plate (Fig. 4(b)). Near the leading edge of the plate the relative error is larger owing to the very small values of the boundary layer thickness. The simulated Michel's criterion data is compared with a profile that grows at a laminar rate until the the simulated flow transitions, and then grows at a turbulent rate after the transition point. The error for this case is around 6% for the laminar regime and drops to less than 2% for the turbulent regime.

The velocity profiles at $x/L = 0.27$ before transition (Fig 5.3) give additional verification of expected behaviors. The fully turbulent boundary layer profile matches the analytical curve, following a power-law profile, with an error less than 5% with the exception of velocities that are very small close to the surface. Prior to transition the computational solution for the case employing Michel's criterion matches the analytical laminar curve with errors less than 2% away from the surface.

After transition at $x/L = 0.96$ (Fig. 5.3) the fully turbulent curve still matches the fully turbulent analytical values with errors less than 3%. The data differ for Michel's criterion where the flow is clearly no longer laminar, but it also does not match the fully turbulent

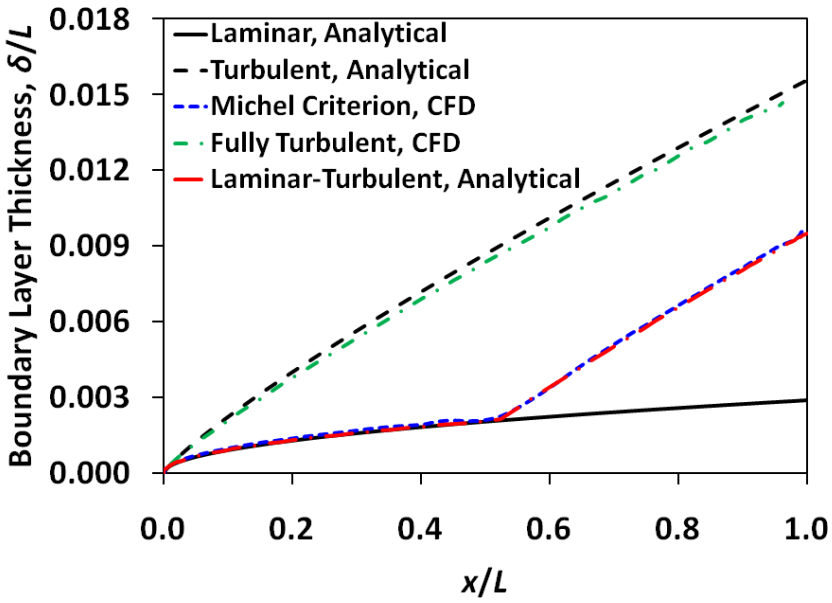

(a) Boundary layer thickness

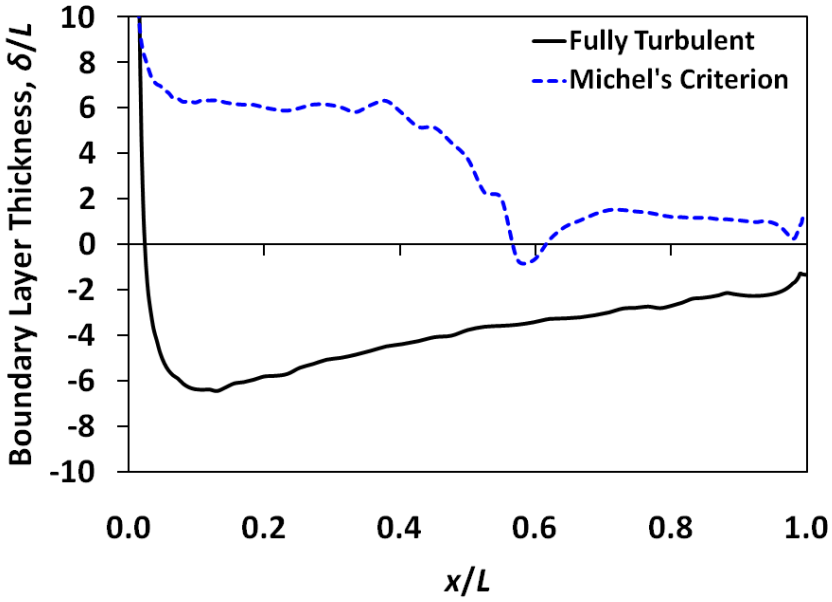

(b) Boundary layer thickness error

Figure 4: Boundary layer thickness along flat plate at a Reynolds number of 3 million.

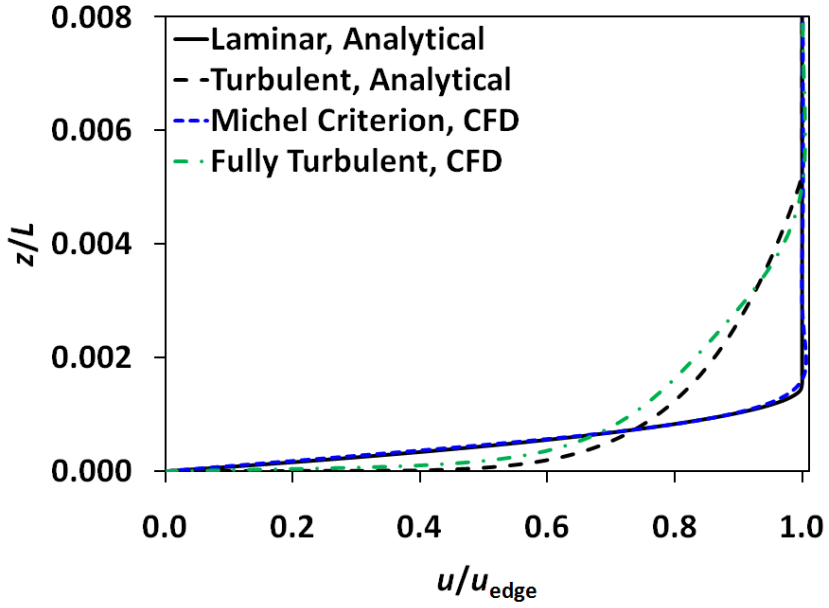

(a) Velocity profile

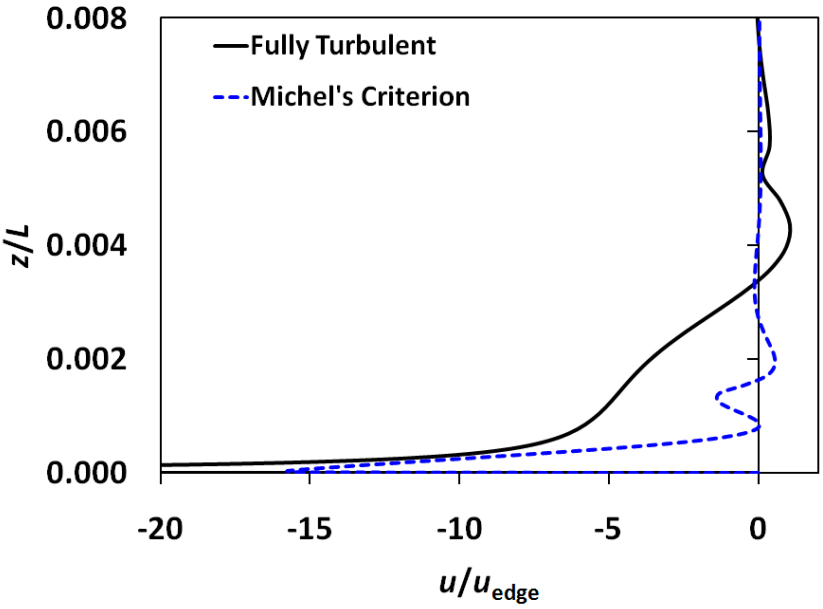

(b) Velocity profile error

Figure 5: Velocity profile before transition, $x/L = 0.27$, for a flat plate at a Reynolds number of 3 million.

curve. The Michel criterion velocity profile follows a power-law turbulent profile, but it does so with the boundary layer thickness of $\delta/L = 0.0090$ from the Michel criterion boundary layer thickness curve (Fig. 6(a)) at the $x/L = 0.96$ station. This would be expected as the boundary layer is fully turbulent, but has not grown as much as the cases that are turbulent starting from the leading edge. The error between the Michel's criterion data and the turbulent profile with the altered boundary layer thickness is less than 5% away from the surface.

The shape factor profiles (Fig. 7) further illuminate the flows and provide additional evidence of transition modeling capabilities. The analytical laminar, Michel criterion, and turbulent CFD shape factors all begin near the expected value of 2.59 for a laminar flat plate flow. With increasing distance from the leading edge, the turbulent CFD curve quickly drops and approaches the analytical turbulent value of 1.3 as the flow develops, whereas the Michel criterion case remains around the higher laminar value. The flow transition to turbulence and the Michel criterion curve begins to drop towards the turbulent value in nearly the exact same manner as the turbulent CFD case at the leading edge.

The decrease in shape factor with turbulent flow results from the increase of momentum at the surface. This increased momentum gives larger velocity gradients at the surface and higher skin friction coefficients (Fig. 8). All skin friction curves begin very high at the leading edge where the velocity gradients are extremely high due to initial boundary layer development very close to the surface of the plate. The turbulent CFD predictions follow the same trend as the analytical turbulent expectations. The Michel's criterion data overlap the laminar curve until transition occurs and the skin friction rises very quickly to follow the fully turbulent trends. The Michel's criterion data after transition to turbulence have consistently higher skin friction than the fully turbulent cases. The reason can be traced to the velocity profiles. Once fully turbulent flow has developed, the Michel's criterion case has a power-law profile as with the fully turbulent cases, but with a thinner boundary layer. This leads to a higher velocity gradient and thus higher skin friction.

The sensitivity of transition to Reynolds number is considered. For a Reynolds number

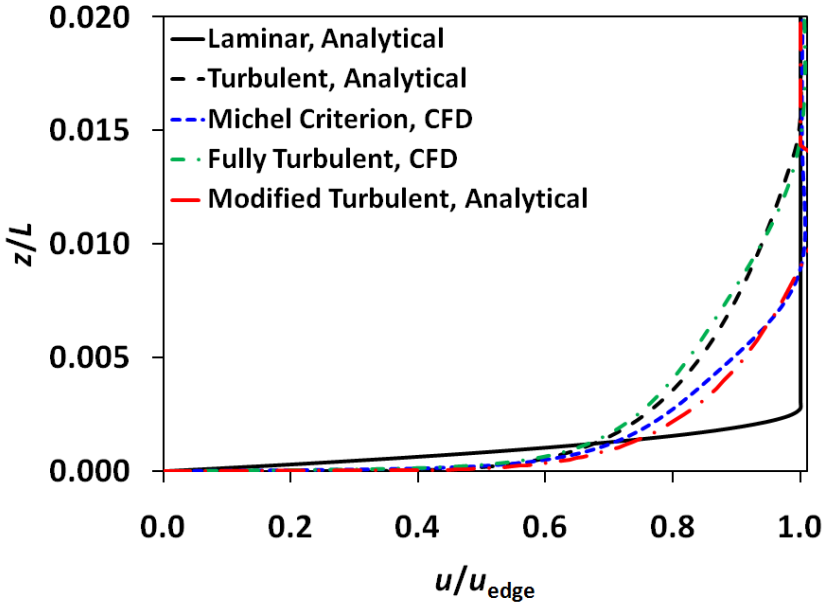

(a) Velocity profile

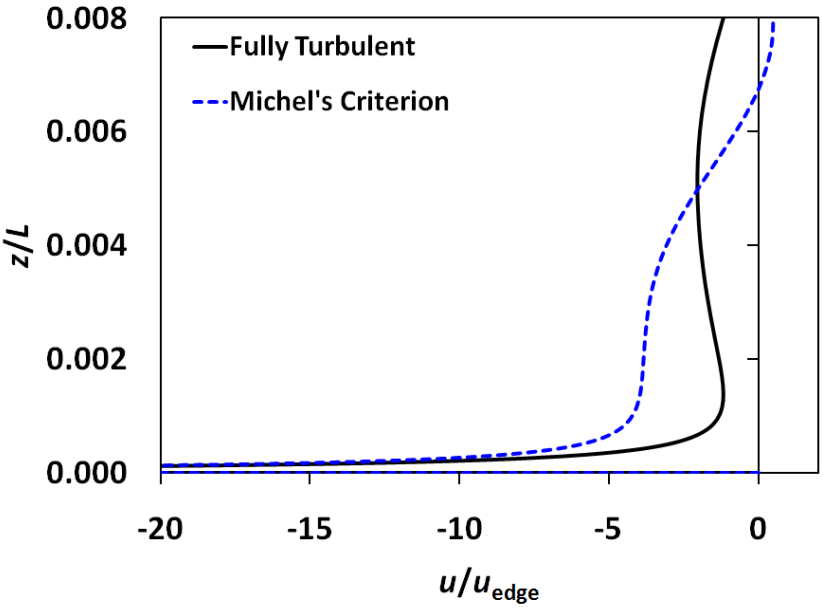

(b) Velocity profile error

Figure 6: Velocity profile after transition, $x/L = 0.96$, for a flat plate at a Reynolds number of 3 million.

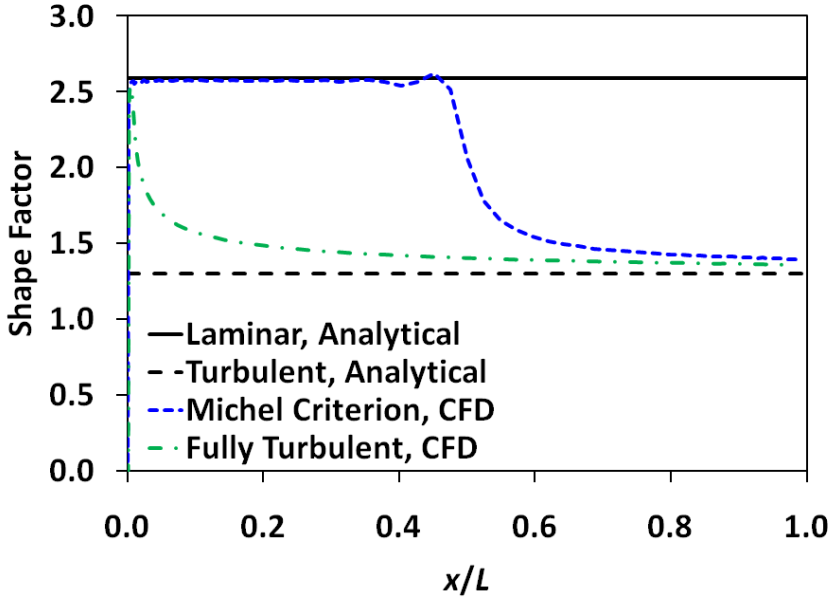

Figure 7: Shape factor along a flat plate at a Reynolds number of 3 million.

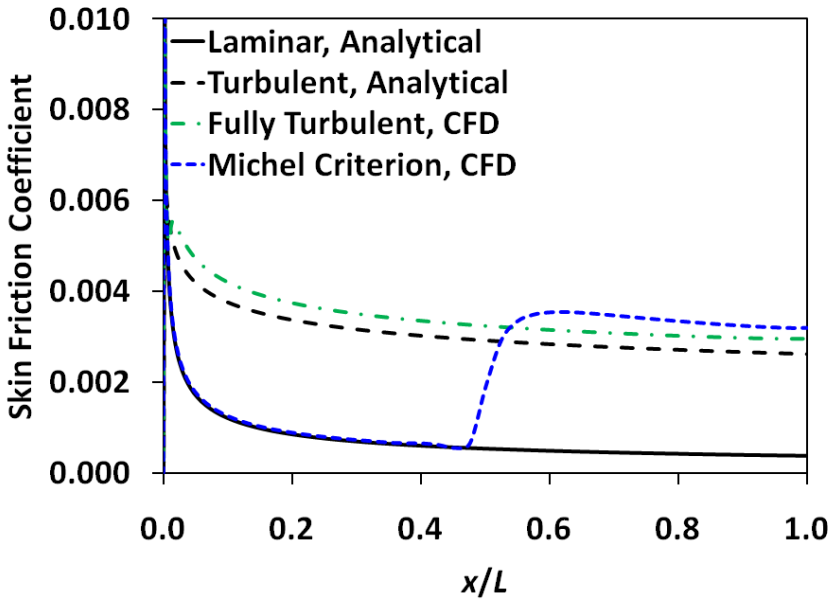

Figure 8: Skin friction distribution for a flat plate at a Reynolds number of 3 million.

of 4 million analytical expectations and computational results of the boundary layer thickness (Fig 9) remain in agreement. In the absence of transition, the boundary layer becomes thinner at the end of the flat plate for a higher Reynolds number of 4 million. For the fully turbulent boundary layer, it is 4% thinner, whereas for a fully laminar flow it would be 15% thinner. This is not true for the transitional case with Michel's criterion, in which the boundary layer thickens by 9% with the increased Reynolds number. This thickening is due to the transition point moving towards the leading edge of the flat plate, causing more turbulent boundary layer growth for the higher Reynolds number and a thicker boundary layer at the end of the plate. Transition begins at $x/L = 0.314$ for this higher freestream Reynolds number, but the local Reynolds number is 1.26 million, which is a change of less than 1% from the lower freestream Reynolds number case. The transition length to reach fully turbulent flow decreases by 7% with the increase in Reynolds, due to the negative exponent containing a freestream Reynolds number dependence in the Chen-Thyson intermittency calculation.

Comparison of the fully turbulent profile with the analytical data gives an error distribution of less than 6% for the majority of the plate. Michel's criterion results are again compared with a profile that grows at a laminar rate until transition and a turbulent rate after transition. The errors are less than 6% and transition drops the errors to less than 1%.

The velocity profiles at the higher Reynolds number (Figs. 5.3 and 5.3) reinforce the findings from the lower Reynolds number previous velocity profiles. Prior to transition (Fig. 5.3), the fully turbulent profiles match, while the Michel's criterion and laminar data overlap. The profiles are thinner than in the lower Reynolds number of 3 million case. The error for both the Michel's crition and fully turbulent data compared with the laminar and fully turbulent analytical curves, respectively, are both less than 5% away from the surface.

After transition (Fig. 5.3), the turbulent curves still overlap with errors less than 3% for most of the profile, and are thinner than the lower Reynolds number case. As with the lower Reynold's number case, the Michel's criterion values no longer follow a laminar profile.

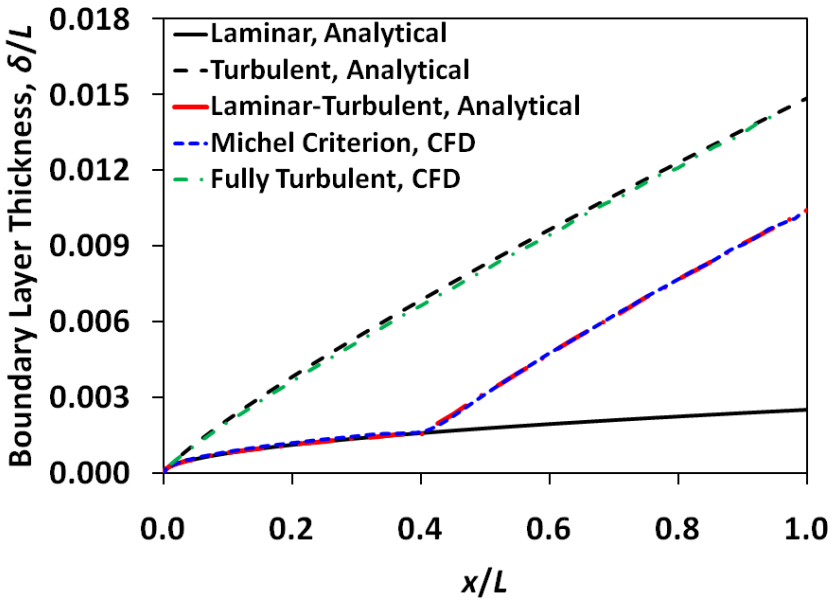

(a) Boundary layer thickness

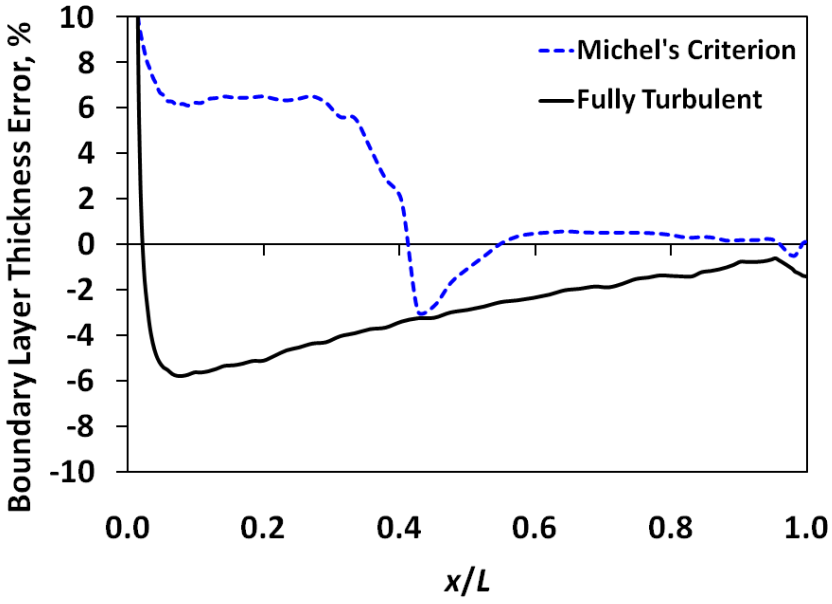

(b) Boundary layer thickness error

Figure 9: Boundary layer thickness along flat plate at a Reynolds number of 4 million.

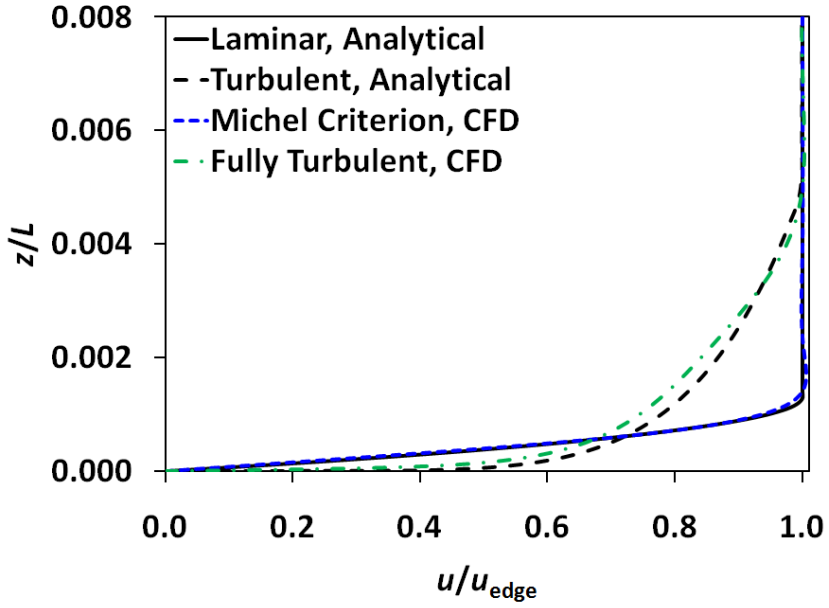

(a) Velocity profile

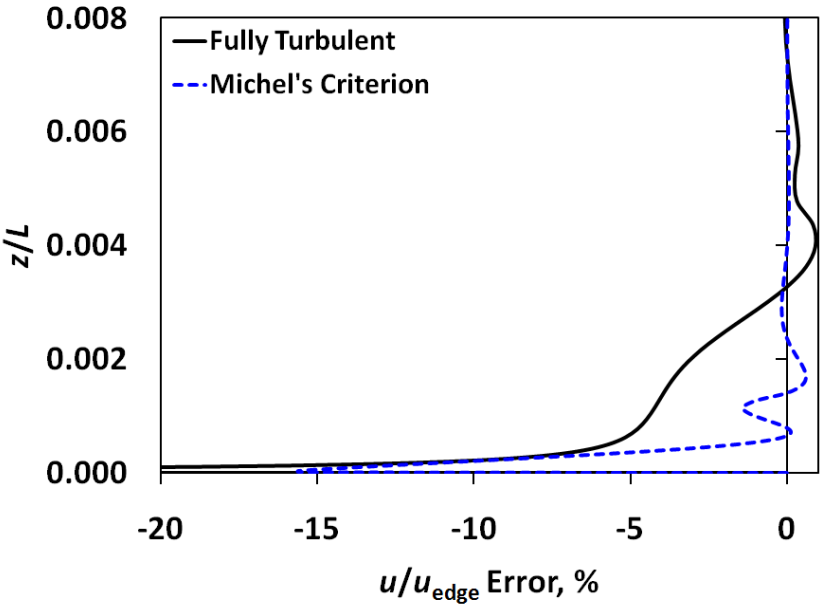

(b) Velocity profile error

Figure 10: Velocity profile before transition, $x/L = 0.27$, for a flat plate at a Reynolds number of 4 million.

The transition point moves toward the leading edge with the higher Reynolds number and gives more turbulent growth. More of the plate is covered by turbulent boundary layer development, leading to boundary layer thicknesses that are closer to fully turbulent than the lower Reynolds number data. As with the lower Reynolds number, the Michel's criterion results follow power-law expectations with a thinner boundary layer, $\delta/L = 0.0099$, with errors less than 3% for the majority of the boundary layer.

Further differences are determined through the shape factor distribution (Fig. 12) at a Reynolds number of 4 million. The turbulent CFD predictions are slightly lower for the higher Reynolds number, which is indicative of the higher degree of turbulence at higher Reynolds numbers. The shape factor also begins to decrease at a lower value of x/L. The shape factor is given by

$$H = \frac{\delta^*}{\theta} \tag{33}$$

Before transition, the displacement thickness is approximated by $\delta^* = 1.721 x Re_x^{-\frac{1}{2}}$, whereas the momentum thickness is approximated by $\theta = 0.664 x Re_x^{-\frac{1}{2}}$, which results in a shape factor of $H = 2.6$ for laminar flow. This value observed before transition for the simulations. After transition, the displacement and momentum thickness growth from the transition point can be approximated by $\Delta\delta^* = 0.02 \Delta x Re_x^{-\frac{1}{7}}$ and $\Delta\theta = 0.01556 \Delta x Re_x^{-\frac{1}{7}}$, respectively. Just after transition, the growth rate of the displacement thickness drops relative to the growth rate of the momentum thickness. This is the cause of the shape facter dropping slowly to the turbulent value of 1.3 just after transition. Transition occurs at a lower value of x/L for the higher Reynolds number of 4 million, and thus the shape factor begins dropping at the same lower value of x/L as well.

The analytical expectations for laminar and turbulent shape factors do not change, as the Reynolds number dependencies of the displacement and momentum thicknesses offset each other. Differences between the skin friction distributions due to Reynolds number (Fig. 13) are similar to those for the shape factor results. Transition at an earlier point on the flat plate leads to a rise in the skin friction closer to the leading edge for the Michel's criterion curve. The inverse relationship of skin friction to Reynolds number is apparent as a drop in the overall values of all skin friction results compared with the lower Reynolds

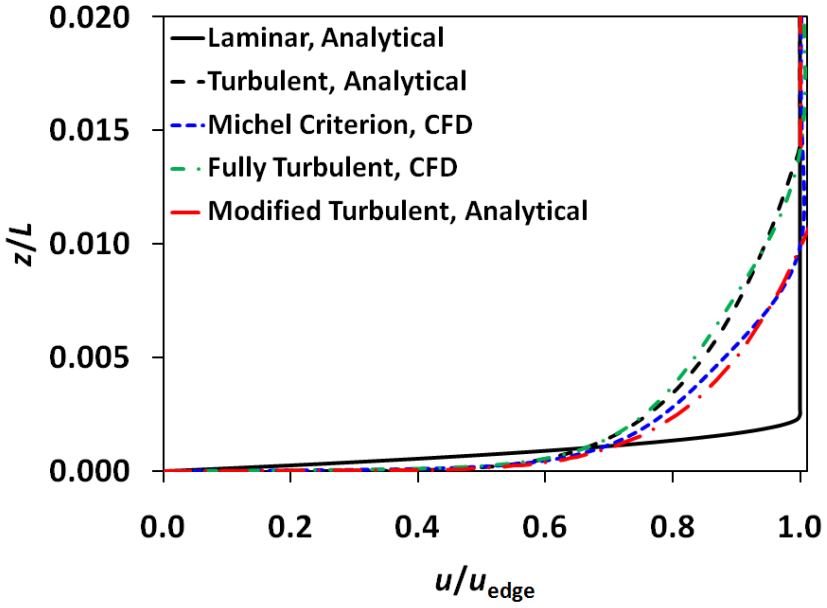

(a) Velocity profile

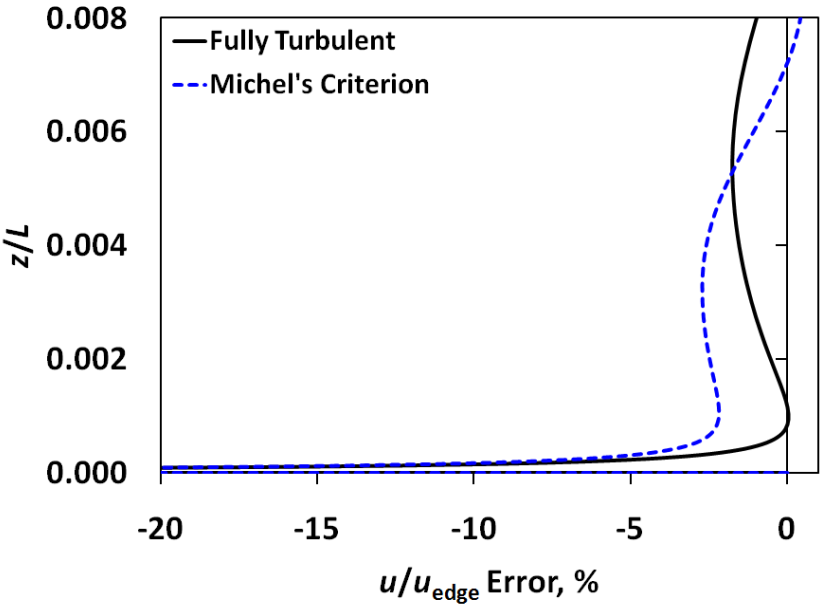

(b) Velocity profile error

Figure 11: Velocity profile before transition, $x/L = 0.96$, for a flat plate at a Reynolds number of 4 million.

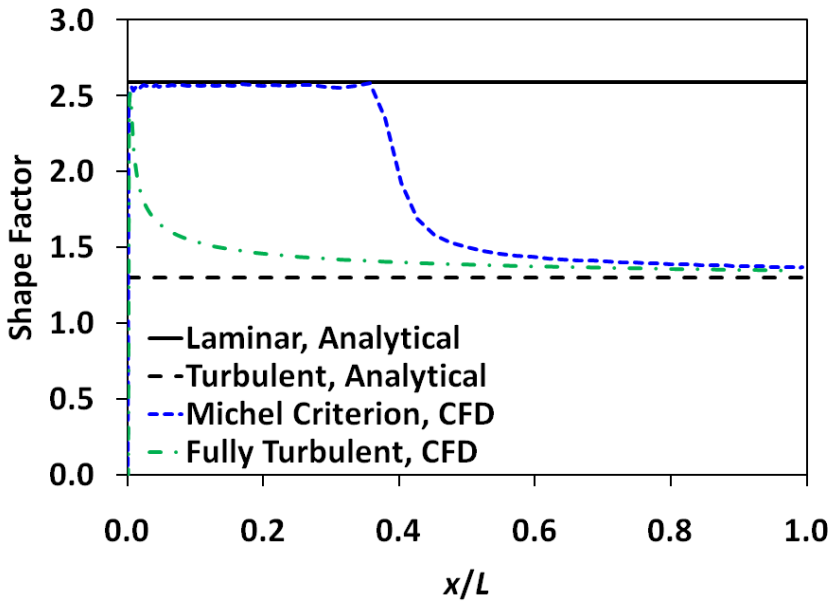

Figure 12: Shape factor along a flat plate at a Reynolds number of 4 million.

number values.

5.4 Airfoil Transition

Analysis of flat plate flows has provided verification of results with analytical expectations when no pressure gradient is present. Flows with curvature and pressure gradients must also be considered, and the prediction of transition on the NACA 0012 airfoil provides this correlation. The transition point as calculated using Michel's criterion moves towards the leading edge of the airfoil with increasing angle of attack (Fig. 14(a)) as anticipated. Increasing the angle of attack leads to additional acceleration and a higher local Reynolds number. This is the source of translation of the transition point forward as the pitch angle increases. Data are provided for the upper and lower surface transition locations.

The relative errors compared with experiment [80] are less than 16% for the lower surface transition location predictions (Fig. 14(b)), but are larger for the upper surface. As the angle of attack increases, the pressure gradient increases. On the upper surface, the transition point moves toward the leading edge and the absolute error remains near $0.02c$, but the smaller values result in much larger relative errors.

There is no strong effect of transition on the lift coefficient for the angle of attack regime

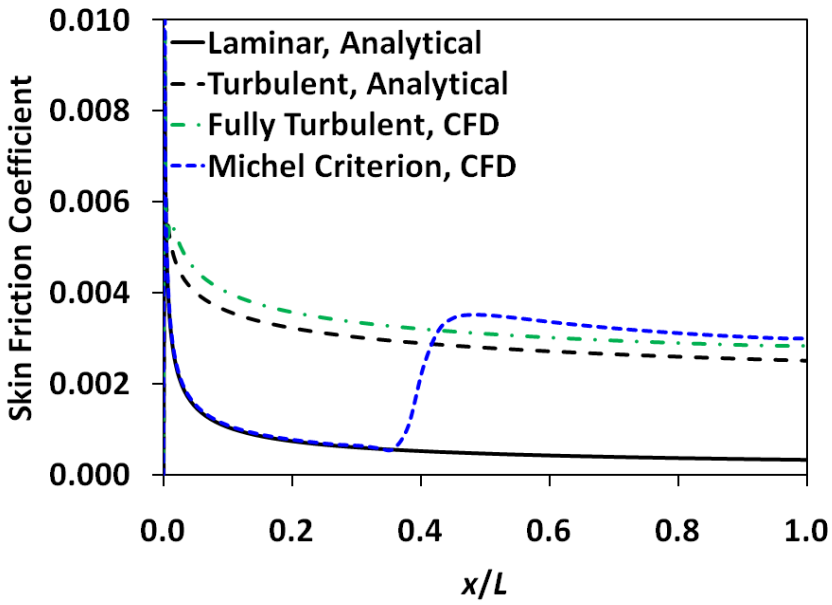

Figure 13: Skin friction distribution for a flat plate at a Reynolds number of 4 million.

considered here (Fig. 15). Results with and without transition provide accurate prediction of lift. The relative error is less than 4% for the angle of attack greater than 0° for both fully turbulent and Michel's criterion data (Fig. 15(b)).

The effect is much more pronounced on the drag coefficients (Fig. 16). Drag is over predicted by the fully turbulent simulations, whereas the addition of transition shifts the drag curve in line with experimental observations. The relative error is reduced from 40-80% down to less than 10% for the angle of attack range investigated (Fig. 16(b)). Investigation of the source of differences between the data may provide additional insights. The skin friction coefficients as a function of angle of attack (Fig. 17(a) through 17(e)). At all angles of attack studied the fully turbulent profiles on the upper surface rapidly rise and slowly decline as the boundary layer thickens while traversing the airfoil chord. Higher angles of attack lead to higher skin frictions via increased acceleration. A less dramatic rise and subsequent decrease is observed for the lower surface fully turbulent profiles. The Michel's criterion data demonstrate similar behavior as in the flat plate verification, where initial laminar skin friction behavior from the stagnation point is followed by turbulent behavior with a value above the fully turbulent profile after transition. The reduced skin friction

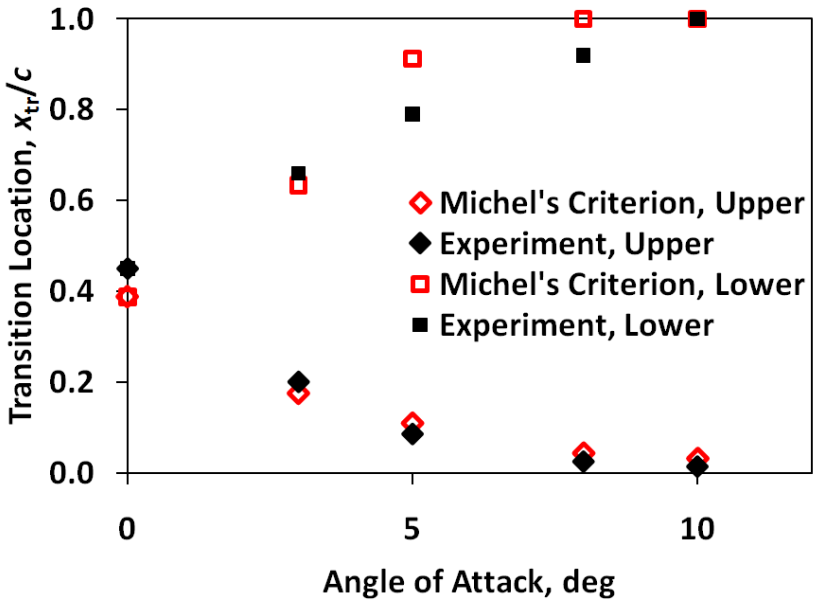

(a) Transition location

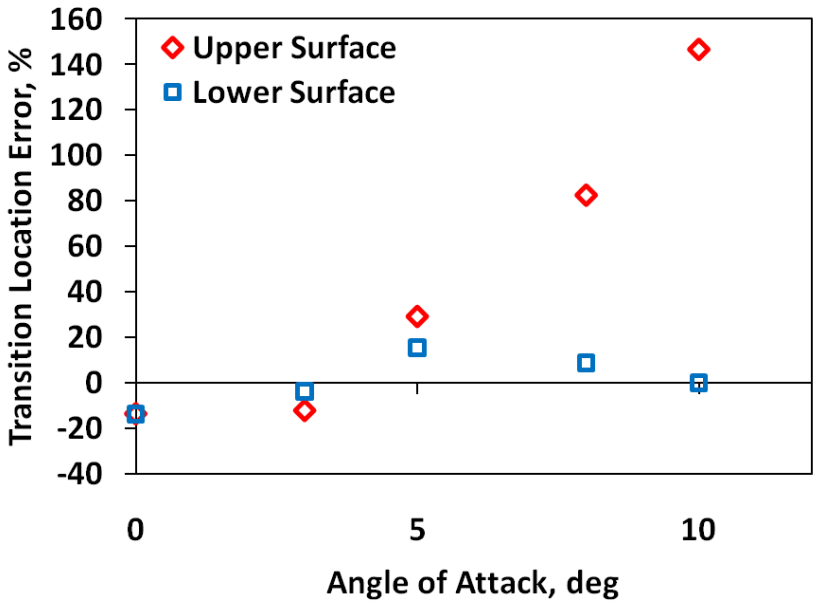

(b) Transition location relative error

Figure 14: NACA 0012 transition location as a function of angle of attack.

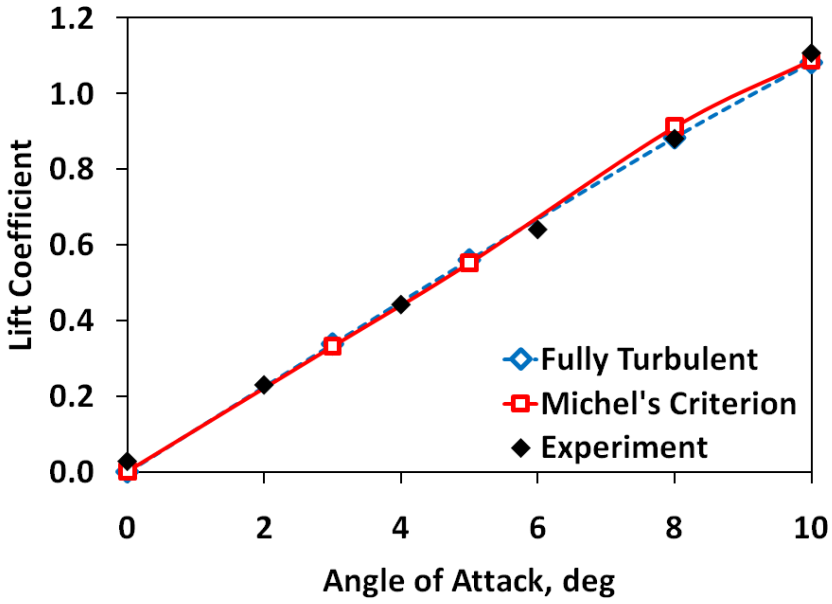

(a) Value

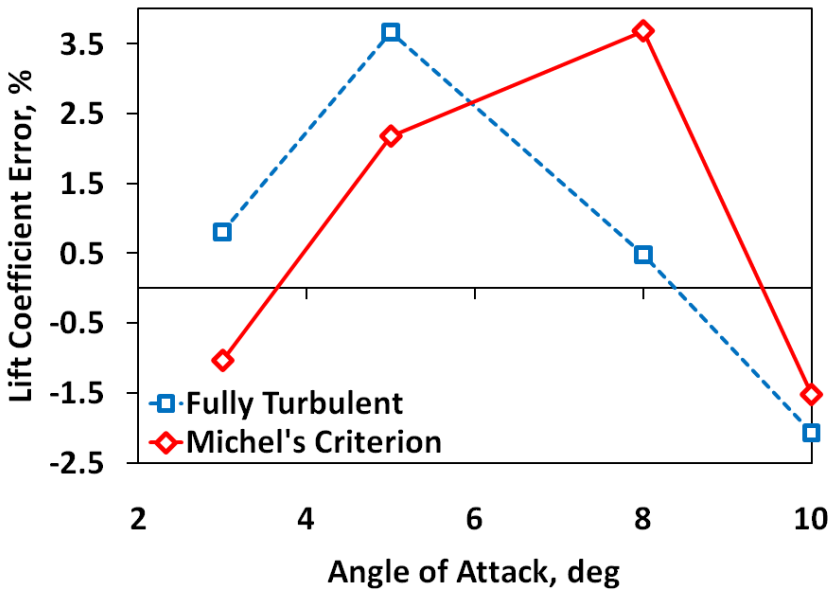

(b) Error

Figure 15: Integrated lift coefficient as a function of angle of attack for NACA 0012 with and without transition.

during the initial laminar region explains reduced drag coefficients, but these profiles have also revealed flow reversal at angles of attack of 8 and 10°, which are not present in the fully turbulent data.

Pressure coefficient distributions (Figs. 18(a) through 18(e)) have little change between fully turbulent and Michel's criterion data below an 8° pitch angle. The point at which the reaches fully turbulent is marked on the pressure coefficient distributions as a vertical red line. The affected region of transition is primarily the boundary layer, whereas the pressure distribution may be approximated as impressed on the boundary layer by the flow at the edge of the boundary layer. For this reason, the pressure coefficients are not strongly affected until transitional effects become much stronger. At lower angles of attack, a slight increase in suction before fully turbulent flow is reached is observed. As the angle of attack pitches higher, the effect increases modestly, but at 8° the pressure undergoes small oscillations before fully transitioning. The same effect is present at 10°.

The velocity flowfield at the leading edge of the airfoil at an angle of attack 8 and 10° (Figs. 19(a) and 19(b), respectively) highlight the flow reversal occurring with Michel's transition. The flow at the leading edge undergoes acceleration and a stronger adverse pressure gradients at higher angles of attack. The initial laminar region does not have the mixing capacity to bring in freestream energy and overcome the pressure leading to flow reversal. The reversal is small at 8°, but the affected region grows much larger at 10°. Transition occurs during this flow reversal leading to enhanced turbulent mixing, which overcomes the pressure gradient and leads to downstream oriented velocity profiles as the flow traverses the chord. It is important to point out that this phenomenon is completely missed by the fully turbulent simulations. As a result of the stronger turbulent mixing starting at the leading edge, the fully turbulent data exhibit no flow reversal as the fluid travels across the airfoil.

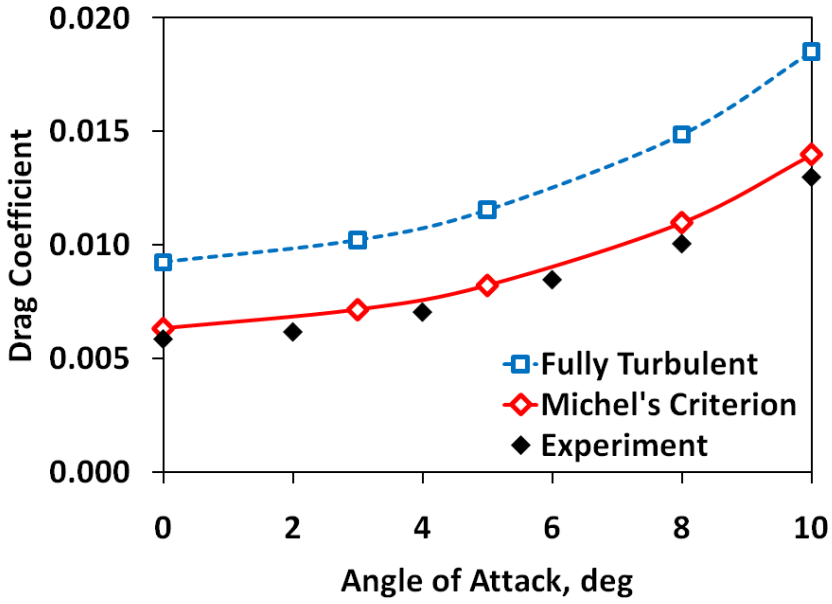

(a) Value

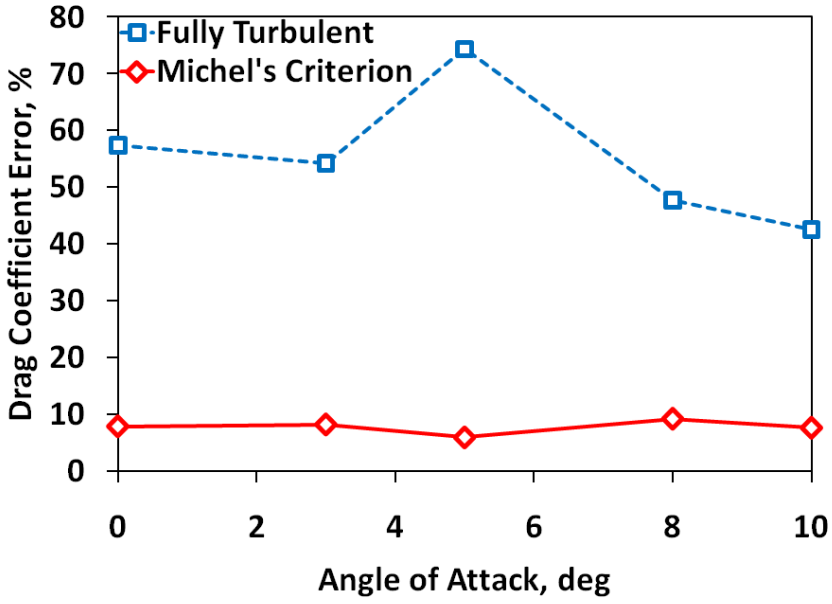

(b) Error

Figure 16: Integrated drag coefficient as a function of angle of attack for NACA 0012 with and without transition.

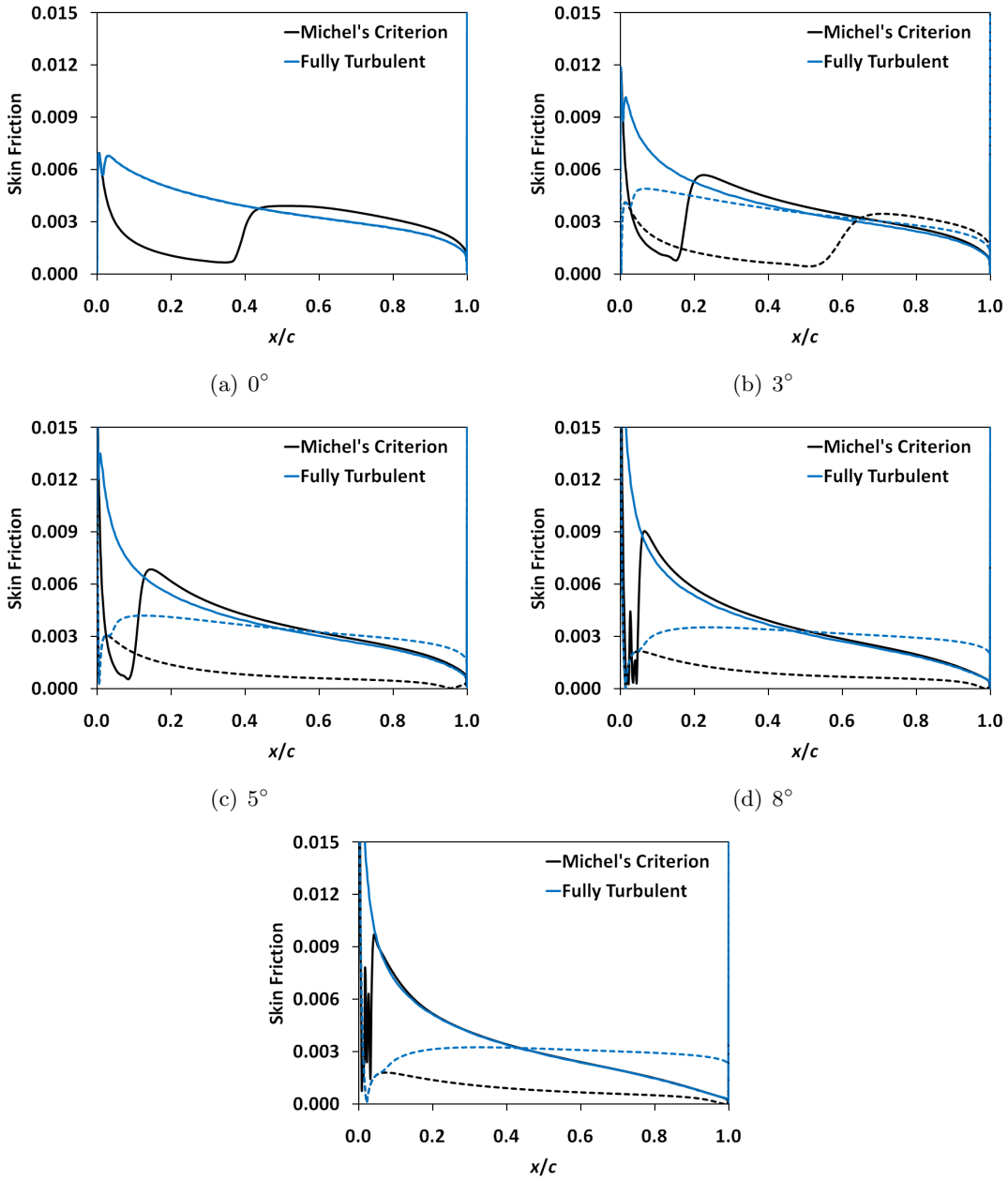

(a) 0°

(b) 3°

(c) 5°

(d) 8°

(e) 10°

Figure 17: Skin friction coefficient distributions with and without transition for static NACA 0012 airfoil. Solid lines are upper surface and dashed lines are lower surface.

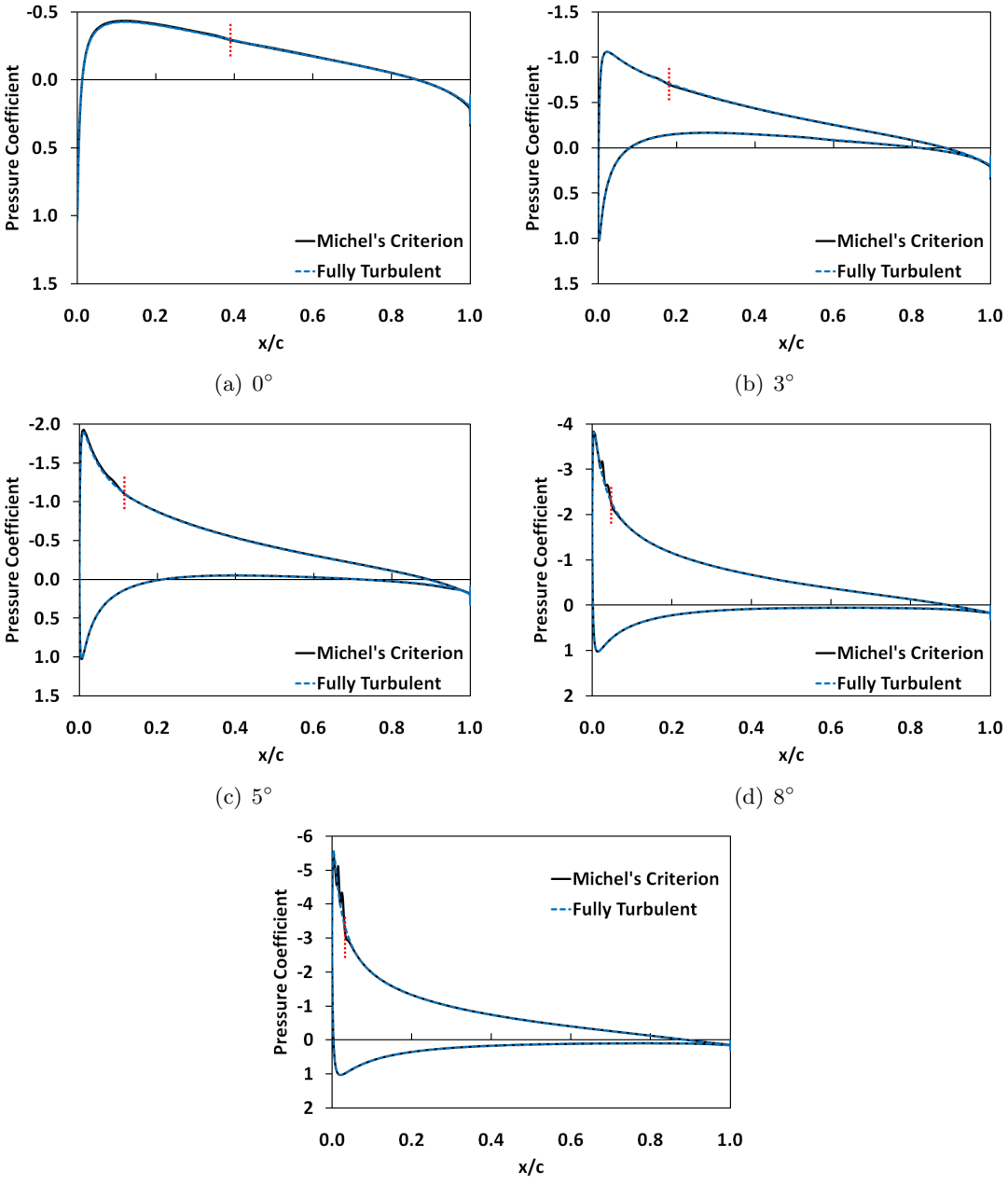

(a) 0°

(b) 3°

(c) 5°

(d) 8°

(e) 10°

Figure 18: Pressure coefficient distributions with and without transition for static NACA 0012 airfoil.

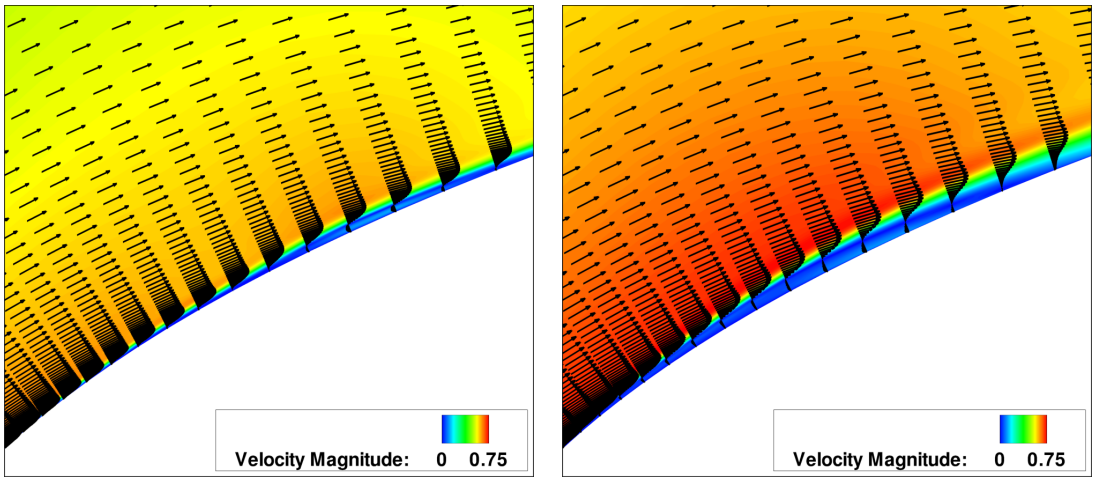

(a) 8° (b) 10°

Figure 19: Velocity field for leading edge of NACA 0012.

CHAPTER VI

CONVERGENCE OF TIME-ACCURATE SIMULATIONS

6.1 Purpose

Airfoils and wings undergoing static and dynamic stall still elude accurate simulation by computational methods. While significant emphasis has been placed on the quantification of grid dependence, as well as influence of the turbulence method, many elements defining temporal convergence remain *ad hoc*. To address this, convergence and accuracy for two different turbulence methods were examined for both static and dynamic stall. New approaches to define numerical convergence that include an assessment of the physical accuracy have been developed and evaluated via a blind analysis at other stall conditions. A key finding is the need to ensure that the combination of time step and subiterations achieves a true second order accurate solution. It was also observed that accurate prediction of separation was controlled primarily by the turbulent transport terms, while the mean flow equations influenced reattachment. Temporal convergence of dynamic stall can be quantitatively assessed by an approach developed in this effort.

6.2 Experiment Correlation

Experimental data used for validation in this study were obtained by McCroskey et al. [81]. This series of static and dynamic stall experiments for different airfoils, including the NACA0012 and VR7 airfoils, was performed in the atmospheric pressure solid-wall 2 $\times$ 3 m wind tunnel at the U.S. Army Aeromechanics Laboratory. These two airfoils are selected for study herein because they are representative of a wide variety of airfoils; taken together, they give rise to both trailing and leading-edge separation [39, 81]. The models, with a chord of 0.61 m and (full) span of 2 m, were rotated in pitch about the 25% chord. Static data were obtained at Mach numbers of 0.11 through 0.30 for an angle of attack range of $-5^\circ \leq \alpha \leq 20^\circ$. Reynolds number varied with $14{\times}10^6 M_\infty$. While most tests were performed with free transition, some run series were repeated using a tripped boundary-layer

located "at the leading edge."

The angle of attack scheduling of the dynamic stall experiments was

$$\alpha(t) = \alpha_0 + \Delta\alpha \sin(\omega t). \tag{34}$$

For this effort, static and dynamic test cases at 0.185 Mach number were evaluated. Dynamic stall data were examined for mean angles of attack of $\alpha_0 = 5^\circ$ and $\alpha_0 = 15^\circ$ with an amplitude of oscillation of $\Delta\alpha = 10^\circ$, at a reduced frequency of $k = \omega c/2U_\infty = 0.10$.

Pressure coefficients were averaged over 50 pitching cycles at 26 Kulite pressure tap locations along the airfoil surface. The resolution was 200 samples per oscillation, and the accuracy of the pressure data was reported to be ± 0.02 psi, while the accuracy of the angle of attack was reported to be $\pm 0.05^\circ$. The maximum error in the cycle oscillation frequency was ± 0.03 Hz. Airfoil lift, moment, and drag data were integrated using a trapezoidal scheme. Integration errors were not observed to be significant compared with uncertainty in the experiments. The authors compared their results with experiments in other facilities and identified the presence of wind tunnel wall effects for static data. Wind tunnel wall effects were reported to be minimal for the dynamic data due to the large aspect ratio of the airfoil and boundary layer control. Recently, Duraisamy, McCroskey, and Baeder[82] have noted that during dynamic stall testing, acoustic disturbances can reflect off wind tunnel walls and significantly alter the magnitude and phase of aerodynamic forces. Therefore, wind tunnel walls were included in this current study to account for these effects.

6.3 Computational Setup

The ARC3D diagonalized Beam-Warming scalar pentadiagonal scheme was employed for temporal integration with spatial differencing by 4^{th}-order accurate Euler terms and smoothing via the TLNS3D scheme. Interpolation between overset grids was performed via 3 fringing points to provide appropriate accuracy for the numerical scheme, while overset mesh hole cutting occurred up to 0.0002 chords away from the solid surfaces.

The boundary conditions for the inlet and exit of the wind tunnel were characteristic Riemann invariants, while the walls were treated as inviscid solid walls. The airfoil surface

was treated with a viscous, adiabatic boundary condition. The initial conditions were uniform flow in the stream-wise direction.

6.4 Grids

Airfoil grid sizing criteria were based on attached and separated flow results from grid studies on NACA0012 and SC1095 profiles using OVERFLOW with the two turbulence methods [83]. These grids had between 811 and 971 nodes around the circumference of the airfoil to achieve integrated force and moment results that were nominally converged within 2-4% of their asymptotic values for separated flows. For all grids, the viscous spacing was $y^+ < 1$ to resolve the boundary layer, with the first wall off-body cell spacing of 3.5×10^{-6} chord. A grid stretching of less than 10% was maintained in all directions, resulting in 50 – 60 boundary layer nodes, well within the limits identified by earlier studies such as [55] and [57]. Spanwise grid spacing was limited to 6.7% chord, providing 49 span stations along the airfoil, although only the midspan station was used to provide correlation results. This spanwise spacing provides sufficient resolution to capture three-dimensional effects as observed in similar approaches with stalled airfoils [83].

In order to study the temporal convergence and flow field characteristics, mesh independence was first verified for the OVERFLOW solver with both Menter $k - \omega$ SST and GT-HRLES turbulence models for 0.185 Mach number, Reynolds number of 2.59 million, and angle of attack of 20°. Simulations were carried out at nondimensional time steps of $\Delta t = 0.0025$ with sufficient subiterations to drop the residual of the L2-norm by at least three orders of magnitude. The time steps were nondimensionalized by the chord and free stream velocity so that a time step of $\Delta t = 0.0025$ is equivalent to a free stream particle traveling $0.25\%c$ during each time step.

To determine the required number of circumferential nodes for accurate resolution of the airfoil flows, static stall was predicted via five VR7 grids of increasing refinement. A configuration without including the wind tunnel test section (to reduce computational costs) was evaluated using an O-grid topology to replicate the blunt trailing edge VR7 airfoil. An O-grid topology was chosen on the basis of the study performed by Smith et al. [30] where

Table 1: VR7 extents and spacings for mesh dependency.

Case	Surface Nodes	$\Delta s_{\text{le}}/c$ %	$\Delta s_{\text{te}}/c$ %
A	203	0.2800	0.0400
B	406	0.1400	0.0200
C	811	0.0700	0.0100
D	1621	0.0350	0.0050
E	3243	0.0175	0.0025

Table 2: Relative change in VR7 integrated loads with increasing mesh refinement.

Case	Turbulence Model	Lift Change %	Drag Change %	Moment Change %
A	Menter $k\omega-$SST	18.4	-34.9	-25.3
B	Menter $k\omega-$SST	8.5	-28.8	-30.7
C	Menter $k\omega-$SST	1.8	-2.7	1.7
D	Menter $k\omega-$SST	0.6	-0.8	-1.8
A	GT-HRLES	11.2	-15.3	-8.9
B	GT-HRLES	1.4	-16.5	-17.4
C	GT-HRLES	1.8	-3.0	-2.3
D	GT-HRLES	0.5	-0.7	-1.3

the importance of its modeling in the stalled regime was quantified. In particular, the shedding of the vorticity at higher (and reverse) angles of attack can be influenced by the geometric modeling of the trailing edge. The spacing for the leading and trailing edges for the coarsest grid, 203 circumferential nodes, were $\Delta s_{le}/c = 0.28\%$ and $\Delta s_{te}/c = 0.04\%$, respectively. Each spacing was halved with increasing refinement (Table 1). As separation occurred solely on the airfoil upper surface, a node distribution of 48.0%, 43.5%, and 8.5% of the total nodes defined the upper surface, lower surface, and blunt trailing edge, respectively. There were 150 nodes in the normal direction for each grid.

The variation of the average integrated pressure lift, drag, and moment coefficients as a function of the number of circumferential nodes provided the determination of mesh independence (Fig. 20). The most sensitive integrated coefficient is usually the pitching moment (Fig. 20(c)); for the free air VR7 grid, mesh independence was achieved with 811 nodes for both turbulence approaches. Mesh independence was confirmed(Table 2) by examining the relative change in the integrated lift, drag, and moment coefficients.

The distance of the far field from the near body was increased as 10, 30, and 60 chords.

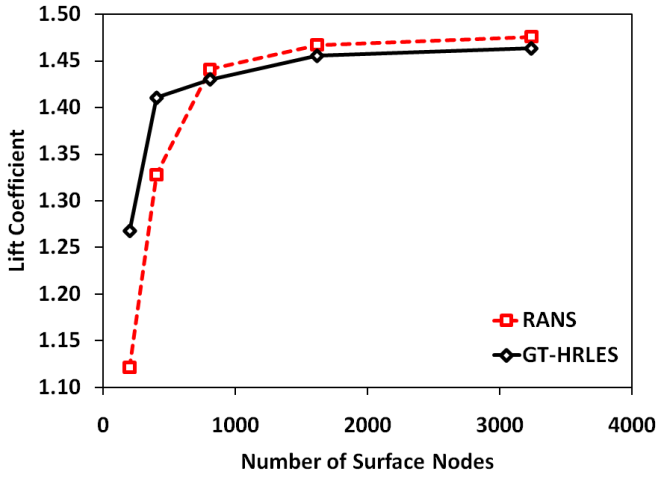

(a) Lift coefficient

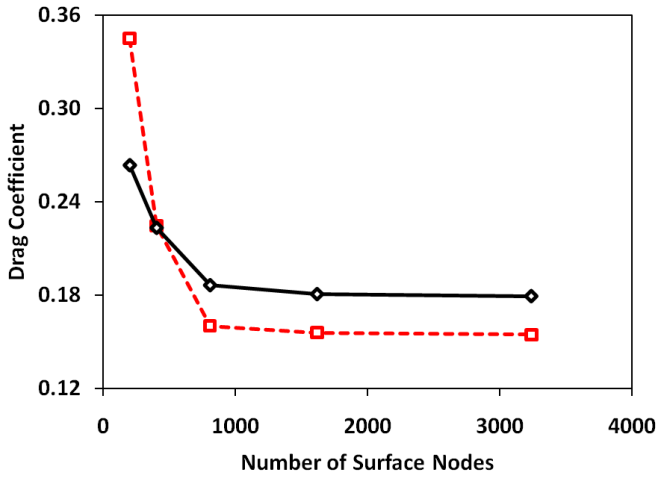

(b) Drag coefficient

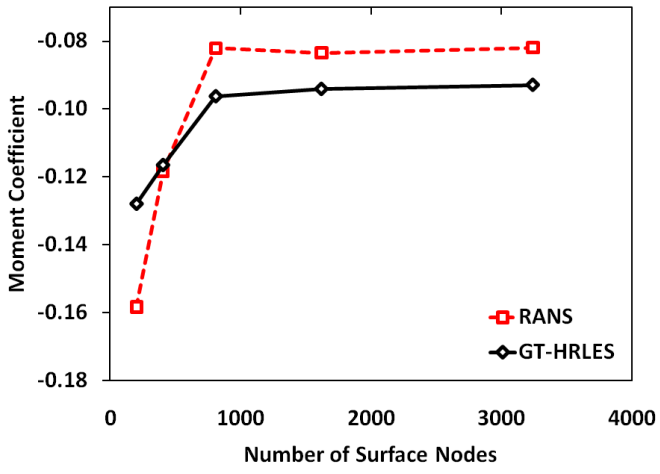

(c) Moment coefficient

Figure 20: Convergence of the integrated coefficients with increasing streamwise point distributions using both URANS and hybrid RANS/LES methods.

The integrated coefficients were examined during this process to verify the minimum domain size that avoided contamination of the solution from the boundary conditions. The lift, drag, and integrated moment coefficients obtained using the baseline 811 nodes mesh C changed by less than 2 to 3% from the smallest to the largest domains (Fig. 21). The use of the 10 chord far field boundary for mesh refinement was justified both through the converged coefficients with increasing far field distance and the fact that the time step/sub-iteration study was carried out within a wind tunnel such that the importance of the far field distance was diminished.

6.4.0.1 Convergence Study Mesh

Based on the grid convergence study, a final grid for characterization of time-accurate convergence with the airfoil within the wind tunnel was developed. Three overset structured meshes were used for the VR7 simulations (Fig. 22). An O-grid was used for the VR7 near-body region with 811 nodes in the circumferential direction and 200 nodes in the direction normal to the airfoil surface with the outer boundary of the grid 2.25 chords away from the surface. Grid points were clustered near the leading and trailing edges to capture larger local gradients. The blunt trailing edge included 71 nodes across the thickness to resolve shed vorticity. The wind tunnel background grid had 465 nodes in the stream-wise direction and 141 nodes in the vertical direction with points clustered near the airfoil. The inlet was located 5 chords upstream the leading edge, while the exit was located 10 chords downstream the trailing edge. A wake grid was utilized with higher resolution of physics downstream the airfoil with 204 nodes in the streamwise direction and 181 nodes in the vertical direction. The grid normal spacing at the airfoil surface was such that the viscous spacing was $y^+ < 1.0$ everywhere with at least 30 and generally 50 points in the boundary layer based on the different Reynolds numbers evaluated. Grid stretching was maintained less than 10% in all directions.

6.5 Static Stall

The VR7 airfoil was evaluated at an angle of attack of 20° (stalled flow) for time steps ranging from $\Delta s = \Delta t U_\infty / c = 0.01$ to 0.000625. For each time step the number of Newton

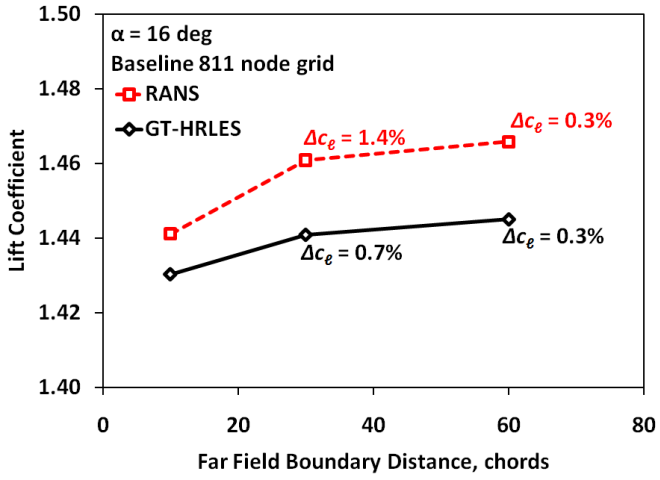

(a) Lift coefficient

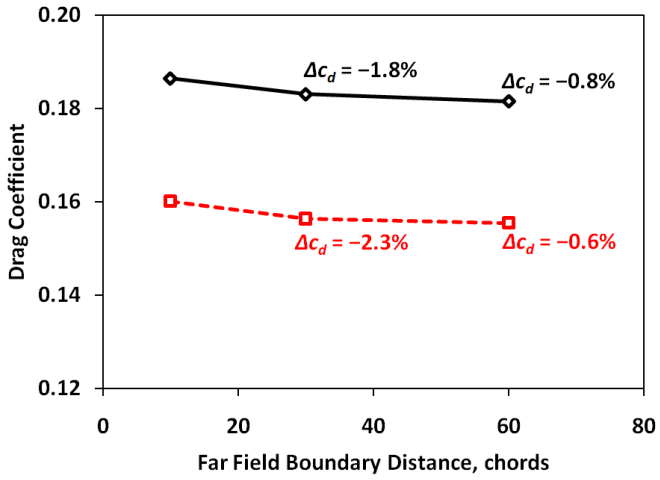

(b) Drag coefficient

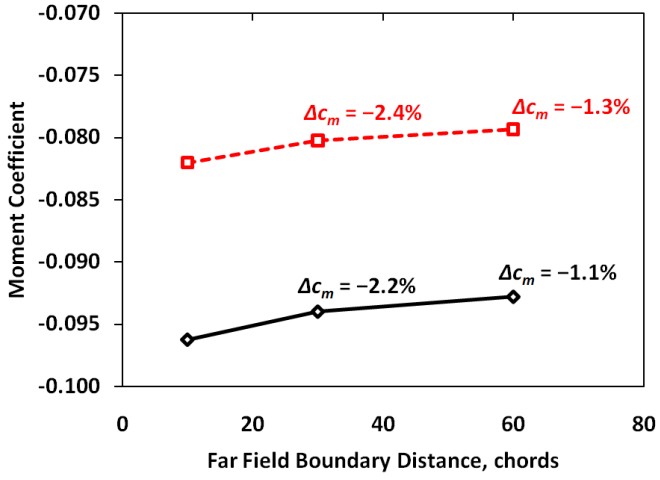

(c) Moment coefficient

Figure 21: Integrated coefficient variation with distance of the far field boundary from the airfoil surface.

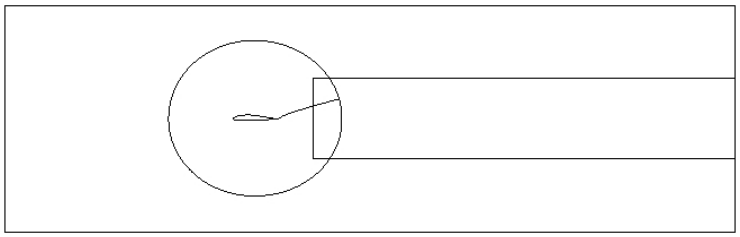

Figure 22: Overall view of the VR7 airfoil time step/sub-iteration study mesh including wind tunnel walls.

subiterations was increased from zero until variation in the averaged integrated lift, drag, and moment coefficients dropped below 1%. Once initial transients in the flow were no longer present, the character of the solution was assessed. If oscillatory behavior representing the natural frequency of the flow separation was present, the solution was averaged over several cycles of this periodic behavior to obtain the mean performance coefficients. To determine the required number of subiterations for a given time step size, the convergence criterion must be defined. Consider for example the drag coefficient at a nondimensional time step of 0.0050 (Fig. 23). Visually, the drag is converged using 20 subiterations. Using a traditional error calculation

$$\varepsilon = 100\% \times \frac{C_d\left(N_{sub}\right) - C_{d,converged}}{C_{d,converged}} \tag{35}$$

and a convergence criterion of 1% error, convergence occurs with 40 subiterations. However, this calculation requires that the converged value be known in order to compute the error, requiring additional calculations. For three-dimensional simulations with advanced turbulence approaches, this method may be prohibitively expensive. An alternative is to examine the rate of convergence

$$\left(\frac{\partial C_d}{\partial N_{sub}}\right)_{relative} \approx \frac{100\%}{0.5\left[C_d\left(N_{sub,2}\right) + C_d\left(N_{sub,1}\right)\right]} \times \frac{C_d\left(N_{sub,2}\right) - C_d\left(N_{sub,1}\right)}{N_{sub,2} - N_{sub,1}} \tag{36}$$

The 1% convergence criterion can be further restricted when applying to convergence rate to ensure that convergence has occurred.

Using the 1% convergence criterion, an analysis of a sweep of time steps of Δs = 0.0100, 0.0050, and 0.0025 for an angle of attack of 20° was examined for the lift, drag

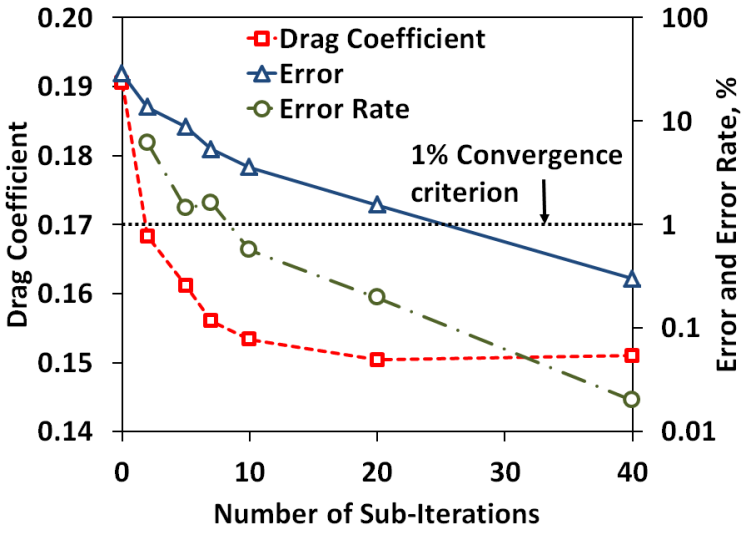

Figure 23: Drag coefficient convergence for RANS approach with $\Delta t = 0.0050$, VR7 at $\alpha = 20°$.

and pitching moment (Fig. 24). As the time step is decreased, fewer subiterations are necessary to satisfy convergence criteria for all coefficients. The reduction of subiterations with decreasing time step is linearly related when the hybrid RANS/LES turbulence method is applied. A higher-order relation exists for the Menter $k\omega$-SST model between the time step and required number of subiterations, in this case a power-law correlation with an exponent between 1 and 2. The accuracy of the pitching moment is also observed to be much more sensitive at larger time steps with the RANS turbulence model, requiring 2.5 times the number of subiterations. An interesting observation is that as the time step size decreases, the number of subiterations for both turbulence methods converge to similar values (within ± 2 subiterations).

Another measure of convergence is reduction of the residual of the variable L2-norms during each subiteration. The L2-norms for these unsteady cases were calculated as averages over several unsteady cycles. For the converged simulations illustrated in Fig. 25, the behavior of the L2-norms is examined. The trends of the L2-norms (Fig. 25) partially reflect those in Fig. 24, in particular the larger residual reductions that occur during the increased number of subiterations. The solutions at the smaller, more accurate time steps may be initially closer to the converged solutions than for larger time steps, such that

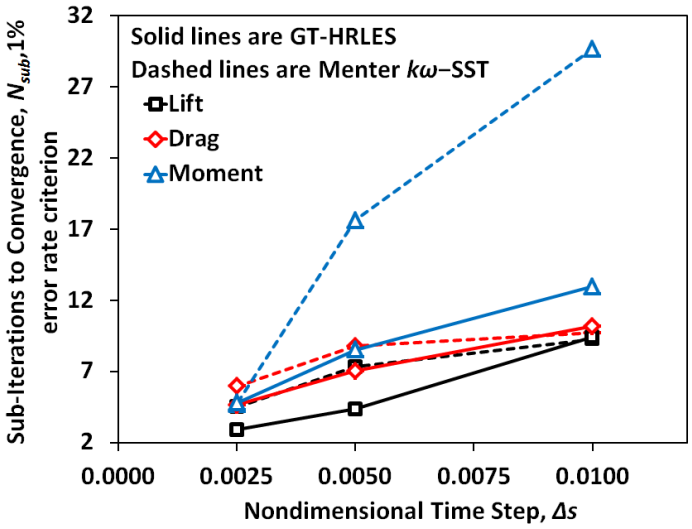

Figure 24: Number of subiterations required to reach 1% convergence rate for differing time steps for lift, drag, and moment, VR7 at $\alpha = 20°$.

fewer sub-iterations and thus lower residual drops were necessary to reach the convergence criterion. Although the convergence criterion was met with only a few subiterations at the smaller time steps (with relatively large residuals), if a larger number of subiterations was employed (i.e., more than 7) the residuals were observed to reduce to even lower values. The hybrid RANS/LES turbulence method results in lower or equal residual reduction compared to the two-equation RANS turbulence model.

The linear behavior observed in Fig. 24 implies that the physical and numerical models of the physics are reasonably well-behaved due to their smooth convergence. Similar fluid phenomena will exist over a range of stalled angles of attack, suggesting that the number of subiterations needed for an accurate simulation in static stall can be estimated for other angles of attack. Using lift as the convergence variable, the number of subiterations can be estimated from Fig. 24 for the RANS and hybrid RANS/LES turbulence methods, respectively, as

$$N_{subs} = 600\Delta s + 3.5 \text{ subiterations}$$
$$\text{error} = \pm 0.8 \text{ subiterations} \tag{37}$$

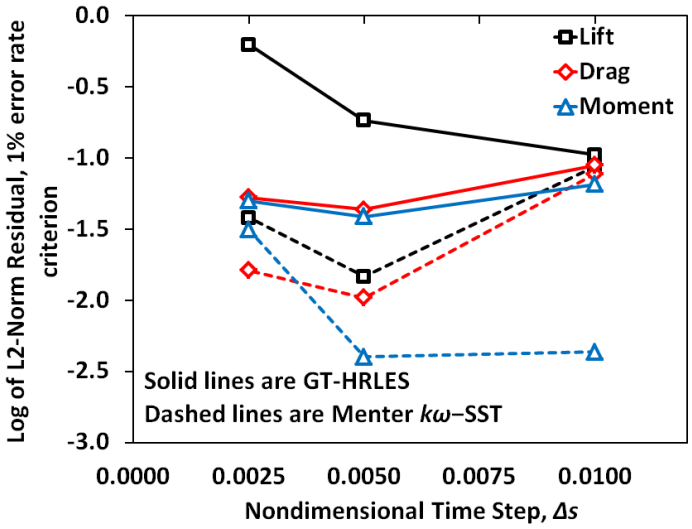

Figure 25: L2-norm residual reduction to achieve the 1% convergence rate criterion of Fig. 24, VR-7 at $\alpha = 20°$.

Table 3: Number of subiterations to reach 1% convergence rate for blind predictions of the VR7 airfoil at different stalled angles of attack.

Angle of Attack, deg deg	Menter $k\omega$-SST, $N_{sub,converged1\%}$	GT-HRLES, $N_{sub,converged1\%}$
18	4.8	2.2
22	5.0	2.8
30	4.7	2.7

$$N_{subs} = 890\Delta s + 0.4 \text{ subiterations}$$

$$\text{error} = \pm 0.3 \text{ subiterations} \tag{38}$$

These equations were used to predict needed subiterations for a 1% convergence rate for angles of attack of $\alpha = 18°$, $22°$, and $30°$ with a time step of $\Delta s = 0.0025$. The number of subiterations was estimated to be 5.0 ± 0.8 and 2.6 ± 0.3 for the Menter $k\omega$-SST and GT-HRLES approaches, respectively. Table 3 confirms that the approach is extensible to other angles of attack, as all simulations reached the convergence criteria within these estimated subiterations. Although this hypothesis is illustrated for a single time step, the aforementioned smooth convergence provides similarly predictive capability at other time steps.

6.5.1 Prediction of Stall Angle

The angle of attack at which the maximum lift ($c_{\ell_{max}}$) occurs is often not well predicted with CFD methods [83, 84]. It is not understood if this poor estimate is a function of the turbulence or transition model, or if it is due to the numerical options applied during the simulation, such as time step. The lift as a function of attack of attack was predicted and a second-order polynomial was applied to determine the angle of maximum lift. It is apparent that for the VR7 airfoil (Fig. 26), whose stall is characterized by trailing edge separation, that temporal convergence does not play a role in the prediction of the maximum stall angle.

6.5.2 Second-Order Temporal Accuracy

Newton subiteration or a similar algorithm are routinely applied to increase the temporal accuracy of the URANS integration scheme. The temporal convergence error at a given time step, $\varepsilon(\Delta s)$, can calculated by extrapolation to a time step of $\Delta s = 0$. The *order of accuracy*, n, is the exponent of the power-law relationship between between the time step and convergence error change

$$\frac{\varepsilon(\Delta s_2)}{\varepsilon(\Delta s_1)} = \left(\frac{s_2}{s_1}\right)^n. \tag{39}$$

Temporal convergence errors of the lift, moment and drag as a function of time step (Fig. 27) indicate that care should be taken in choosing time step size to ensure second-order temporal accuracy. It is not until a nondimensional time step of $\Delta s = 0.0025$ or less is applied that formal second-order temporal accuracy is achieved. All of the integrated quantities (lift, drag, pitching moment) predict the same behavior, so that any of these can be used to verify formal accuracy of the simulation.

The influence of the formal accuracy on the physics of the simulation can be observed by the shed vorticity from the main and secondary separated flows. The most visible illustration of this behavior can be seen from the blunt trailing edge of VR7 airfoil (Fig. 28), which can occur during both attached and stalled flows. During first-order integration the shed vorticity is smeared, while for second-order accurate solutions, periodic vortices are shed, as physically expected for a blunt body at these flow conditions.

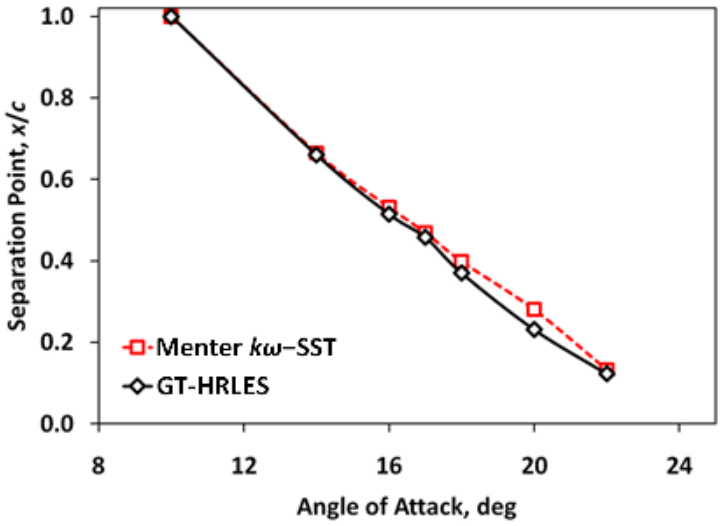

(a) Static stall separation point.

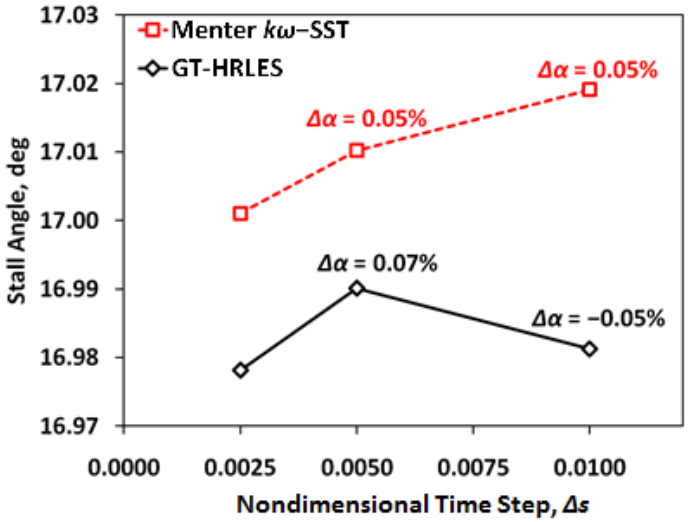

(b) Stall angle variation with time step.

Figure 26: Prediction of the VR7 static airfoil characteristics using the RANS and GT-HRLES methods.

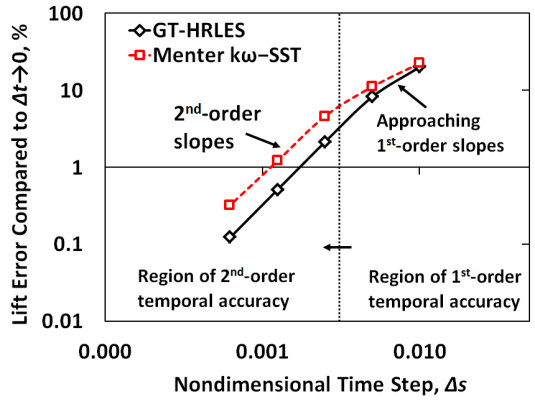

(a) Lift

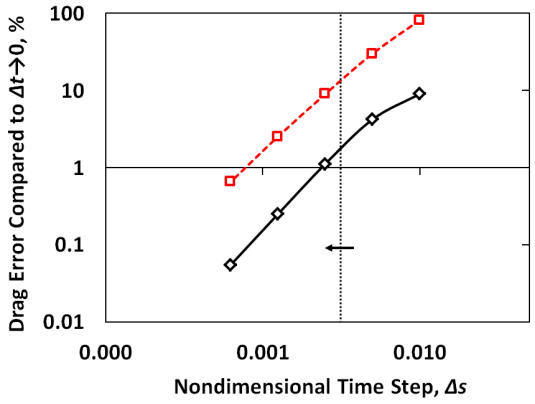

(b) Drag

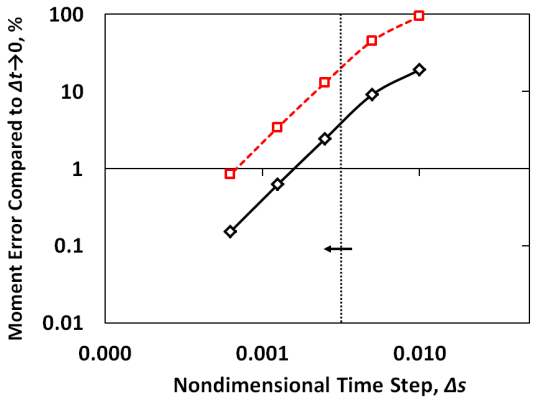

(c) Moment

Figure 27: Illustration of the impact of the recovery of second-order accuracy on the integrated performance coefficients for the VR7 airfoil for static post-stall angles of attack.

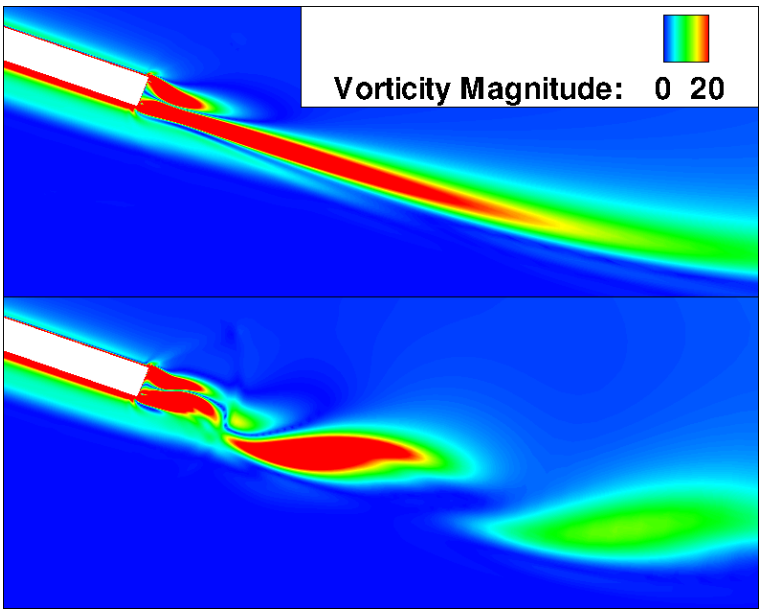

Figure 28: Vorticity at blunt trailing edge for stalled VR7 flow at the same physical time with two different time steps; $\Delta s = 0.01$ on top and $\Delta s = 0.005$ on bottom.

6.5.3 Cost

Doubling the number of mean flow subiterations increases the computational requirements by 56% for the Menter $k\omega$-SST simulations and 63% for the GT-HRLES simulations. The cost per subiteration using the GT-HRLES method is 13% higher than for the Menter $k\omega$-SST method due to the additional subgrid-scale hybridization. Doubling the number of subiterations does not double the computational costs for either approach, since only a portion of the flow solver loop is repeated. The cost of the predictions to satisfy the 1% convergence criterion decreases with increasing time step (Fig. 29). This observation is important, as the most computationally efficient simulation will be obtained with the largest allowable time step, even though this will require an increased number of subiterations. However, an unbounded time step will not usually be satisfactory; the upper limit on the time step is governed by the need to maintain accuracy by remaining within the second-order accurate domain.

Using the 1% error rate criterion on the integrated coefficients, the GT-HRLES simulations were actually 20% *less* expensive than the RANS simulations for a converged solution at a given time step. This result was due to the requirement of fewer subiterations to reach

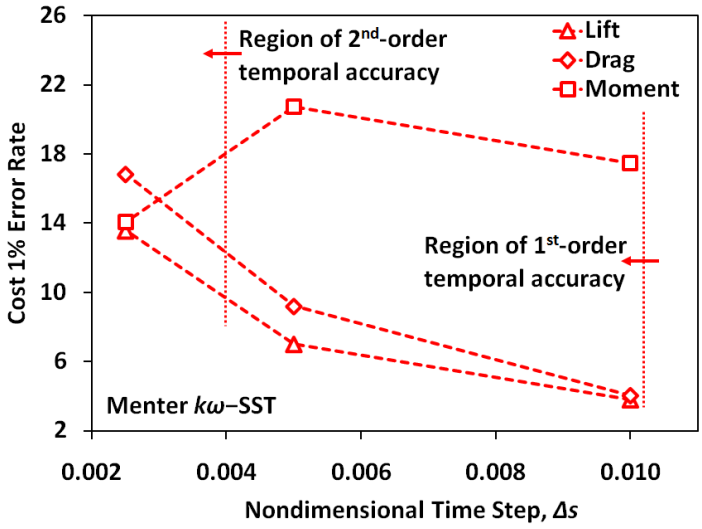

(a) Menter $k\omega$-SST cost

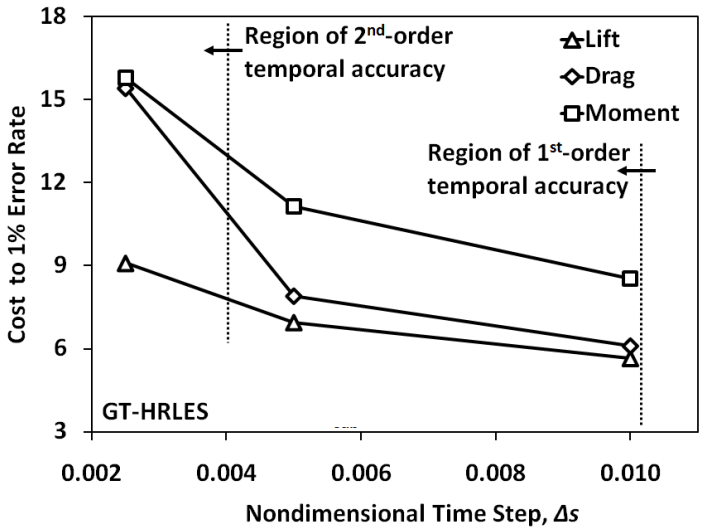

(b) GT-HRLES cost

Figure 29: Cost of static post-stall simulations as a function of the effective time step; costs are normalized by the baseline cost of GT-HRLES with 1 subiteration and $\Delta s = 0.01$.

convergence for GT-HRLES (Fig. 25).

6.6 Dynamic Stall

Accurate numerical simulation of dynamic stall is a continuing area of concern and research for rotating systems, such as rotorcraft and wind turbines. To address this concern, the VR7 airfoil with a reduced frequency of $k = 0.10$ in dynamic stall has been studied with the Menter $k\omega-$SST and GT-HRLES turbulence approaches. This particular case was chosen as it is characterized by double dynamic stall where primary and secondary stall events, as well as reattachment, have presented significant modeling difficulties for CFD. The angle of attack scheduling was $\alpha = 15^\circ + 10^\circ \sin(ks)$ about the quarter-chord at a Mach number of 0.185 and nominal Reynolds number of 2.59 million. Data were averaged over several cycles, where repeatability of data from cycle to cycle was observed. Modeling via RANS turbulence methods can lead to some deficiencies, including smearing of spanwise flowfield characteristics. These deficiencies are the primary reason RANS methods were not utilized for moderate to high angle of attack airfoils in previous studies [30, 83]. These deficiencies do not prevent cycle averaging of the results for collection of data, because as previously mentioned the cycle to cycle results, particularly with RANS turbulence models, are repeatable.

6.6.1 Dynamic Stall Convergence

Current practice to determine the convergence of a dynamic stall simulation is to repeat the stall cycle until there is visually little change in the integrated forces and moments between cycles. However, that inspection does not ensure that the simulation has converged to the correct physical behavior, as has been noted by Moulton and Smith [85], with regard to reattachment and other complex flow physics. Convergence was studied using a variety of time steps per cycle and Newton subiterations, based on the observations from the static stall analysis.

A dynamic stall case that is representative of dynamic stall phenomena including the attached upstroke ($\alpha = 5^\circ$ to 20°), the post-stall ($\alpha = 23^\circ$up to $\approx 20^\circ$down), and the downstroke post-reattachment ($\alpha = 20^\circ$ to 5°) was chosen. For a hysteresis cycle (Fig. 33),

the behavior of the integrated lift, drag, and pitching moment was examined. A new parameter, T, is defined as the number of time steps/cycle $\times$ subiterations. The $lim(1/T) \rightarrow 0$ as the number of time steps $\times$ subiterations is increased to infinity, and characterizes the prediction accuracy of the simulation.

For angles of attack along the cycle upstroke, a linear relationship between the integrated coefficients and $1/T$ (Fig. 30) can be observed. This was not the case, however, for the integrated coefficients in the post-stall region (Fig. 31) where the data convergence was non-monotonic. The region of convergence has been outlined by the dashed lines. For angles of attack after flow reattachment occurred during the downstroke, linear convergence of the coefficients was again observed. This implies that, for a particular grid, physical convergence can be determined by examining the convergence of the integrated quantities when the flow is attached during the dynamic stall cycle. Interestingly, while in the limit of $1/T \rightarrow 0$ the lift converged to its most accurate correlation with the experimental data, a similar observation cannot be guaranteed for the drag and pitching moment. Thus, it may appear that a simulation is converged due to improved drag and/or pitching moment values, but this may not be the case. An estimate of the accuracy of the simulation can be determined by applying a least-squares fit to the integrated coefficients at angles of attack when the flow is attached and extrapolating to 0 (for $1/T$). For example, in Fig. 30 a) for the GT-HRLES simulations, a linear least-squares fit of the data yields the expression:

$$C_\ell = \frac{-5040}{T} + 1.7069 \tag{40}$$

The extrapolated value of the converged lift coefficient as $T \rightarrow \infty$ yields a $C_\ell = 1.7069$, which has an error of 6.8% compared to the experimental value.

The importance of subiterations is illustrated by the case of 9,000 steps per cycle (Fig. 33), which nominally meets 2^{nd} order temporal accuracy in the static stall analysis. While fewer subiterations clearly capture most of the attached flow characteristics ($s = 0.00 - 0.10$ and $s = 0.75 - 1.00$), a significant phase and amplitude error of the stall features compared with experiment is observed. This phase shift improves with increasing numbers of subiterations.

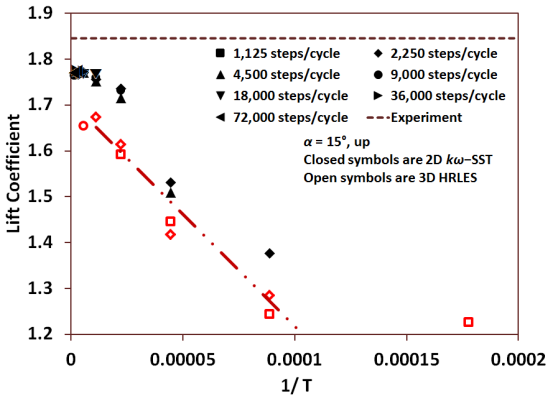

(a) Lift coefficient

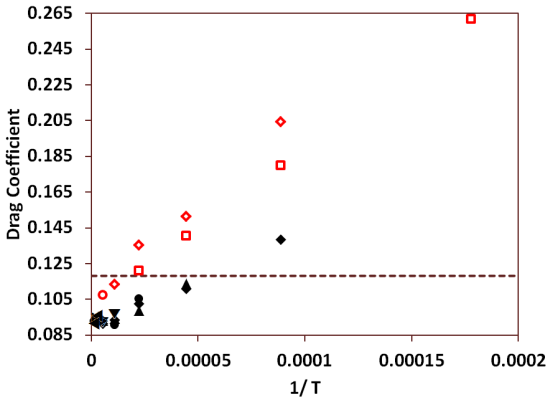

(b) Drag coefficient

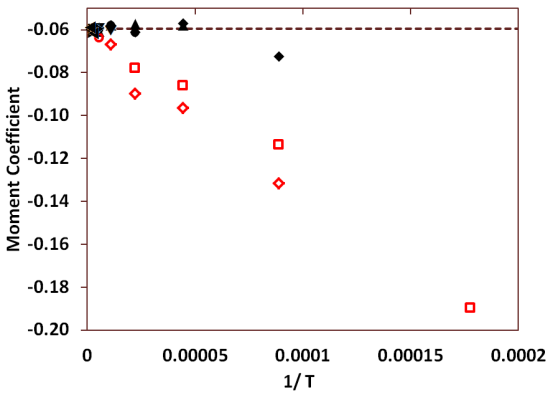

(c) Moment coefficient

Figure 30: Convergence of the VR7 airfoil integrated coefficients on the dynamic stall attached upstroke for $\alpha = 15°$ and a reduced frequency of $k = 0.10$.

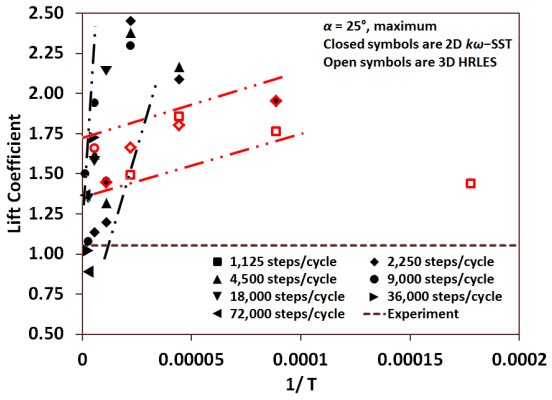

(a) Lift coefficient

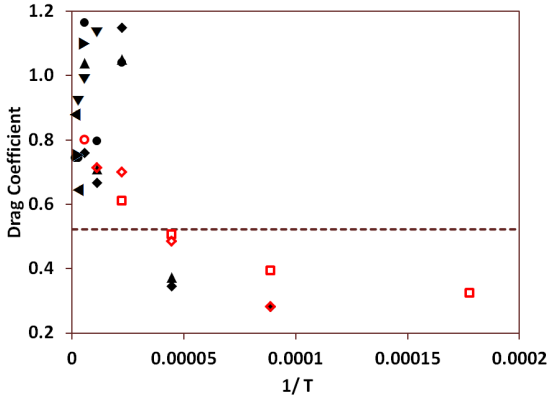

(b) Drag coefficient

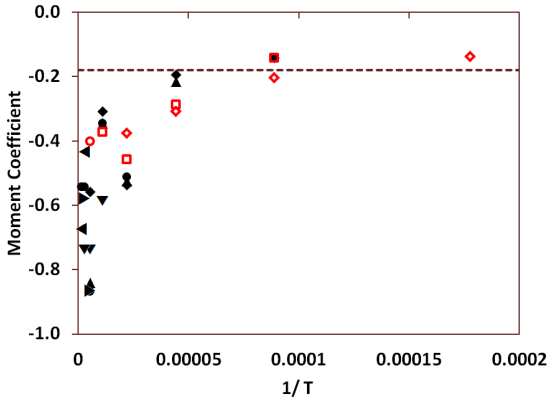

(c) Moment coefficient

Figure 31: Convergence of the VR7 airfoil integrated coefficients in post-stall for $\alpha = 25°$ and a reduced frequency of $k = 0.10$.

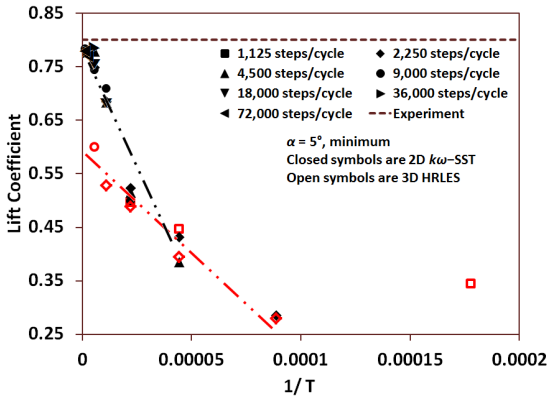

(a) Lift coefficient

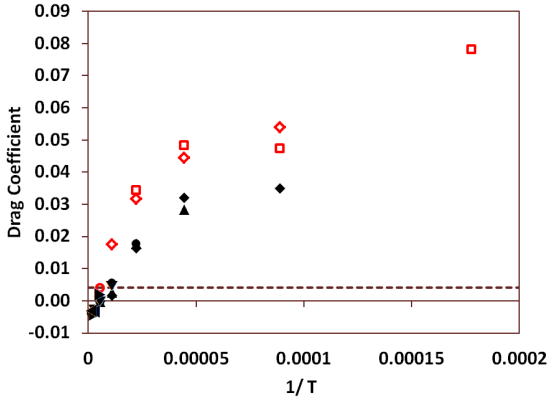

(b) Drag coefficient

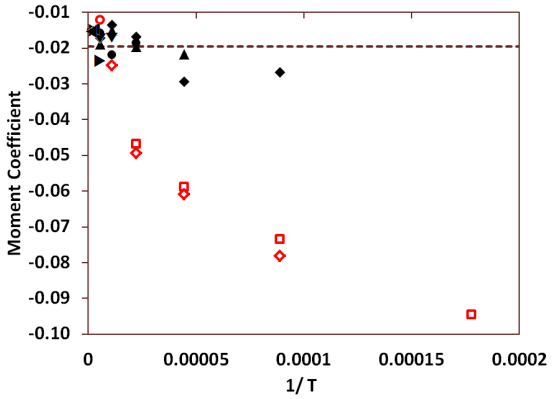

(c) Moment coefficient

Figure 32: Convergence of the VR7 airfoil integrated coefficients in post-reattachment for $\alpha = 5°$ and a reduced frequency of $k = 0.10$.

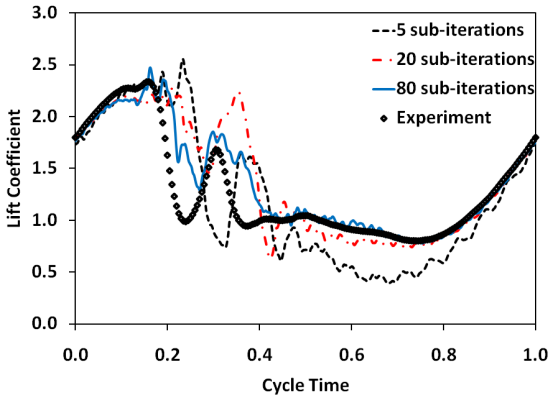

(a) Lift coefficient

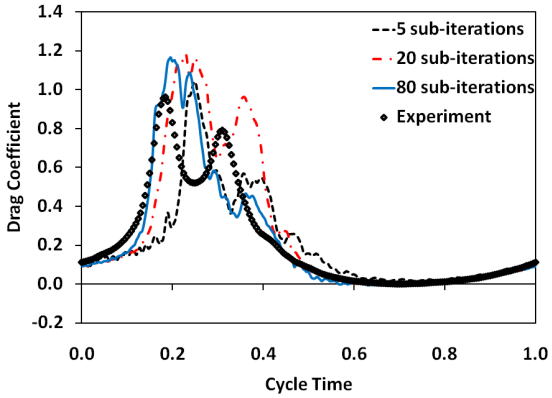

(b) Drag coefficient

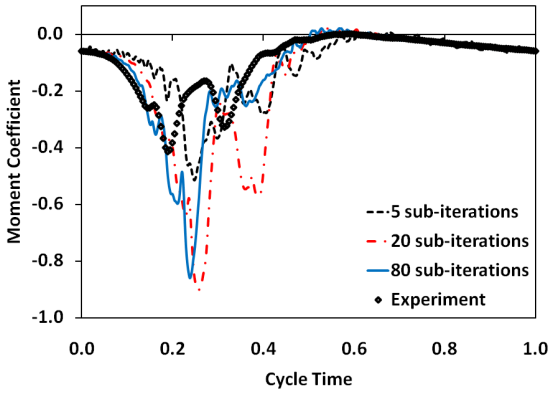

(c) Moment coefficient

Figure 33: Coefficient history for VR7 airfoil for a $k = 0.10$ dynamic stall with 9,000 steps/cycle and the Menter $k\omega$-SST turbulence model.

The selection of time step size from the T parameter is next examined. Based on a series of simulations, linearity of the M parameter with different time step values was confirmed. The linearity of the time steps (that provide second-order temporal accuracy) with T is illustrated by comparing the integrated coefficients for 9,000 steps/cycle $\times$ 20 subiterations and 36,000 steps/cycle $\times$ 5 subiterations (Fig. 34) with the Menter $k\omega - SST$ turbulence model. Each of the coefficient response curves predict similar behavior in the stalled region and are coincident when the flow is attached. It is important to point at that this behavior is consistent only when the time step ensures second-order temporal accuracy as previously determined for static stall, indicating that the physics are being correctly captured.

It should be noted that an error controller that limits the number of subiterations based on a predefined residual reduction can be applied to significantly reduce the number of subiterations over the regions of the simulation where the flow remains attached. Using the results of this study as a guide, the cost of performing simulations using the 9,000 steps/cycle with a maximum of 20 subiterations per time step with a residual reduction of 1.8 to ensure second order accuracy, the cost of one cycle of the simulation was reduced by 60%. On the upstroke and after flow reattachment on the downstroke, as few as 4–5 subiterations per time step were needed, and for other portions of the simulation, the residual reduction was met with fewer than 20 subiterations. During the strong first and second dynamic stall events, the maximum number of subiterations was needed to reduce the residual. These results may vary depending on the type of error controller, but serve to illustrate the usefulness of the error controller.

6.6.2 Prediction of Stall Onset and Reattachment

The dependence of the location of the onset of stall and reattachment can be correlated with the number of subiterations. Although stall and reattachment are processes rather than instantaneous events, for the purposes of analysis a point in time must be defined that can be called the *event time*. The stall event time is defined as the point in the cycle where the lift reaches a maximum and begins to significantly decrease of a small period of time (or change in angle of attack). The location of reattachment is defined as the angle

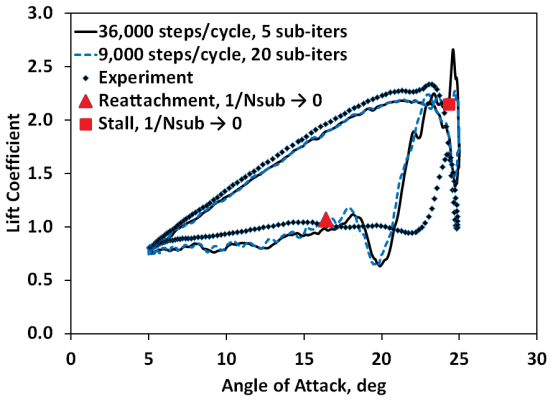

(a) Lift coefficient

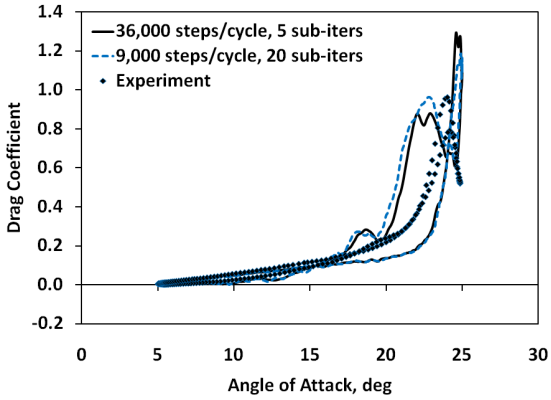

(b) Drag coefficient

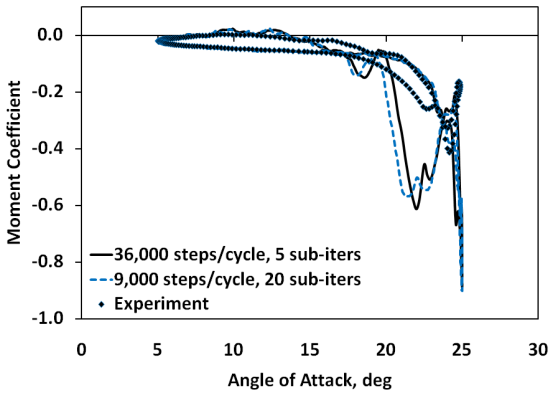

(c) Moment coefficient

Figure 34: Coefficient history for the VR7 airfoil for a $k = 0.10$ dynamic stall with 180,000 time steps $\times$ subiterations per cycle and the Menter $k\omega$-SST turbulence model.

of attack which corresponds to the end of the large scale coefficient oscillations associated with vortex shedding and the rearward movement of zero-shear stress point on the upper surface. The times at which stall and reattachment occurred were examined at various time step and subiteration combinations.

The dependence of the location of the onset of stall and reattachment can be correlated with the number of subiterations. Although stall and reattachment are processes rather than instantaneous events, for the purposes of analysis a point in time must be defined that can be called the *event time*. The stall event time is defined as the point in the cycle where the lift reaches a maximum and begins to significantly decrease of a small period of time (or change in angle of attack). The location of reattachment is defined as the angle of attack which corresponds to the end of the large scale coefficient oscillations associated with vortex shedding and the rearward movement of zero-shear stress point on the upper surface. The times at which stall and reattachment occurred were examined at various time step and subiteration combinations.

A strong linear correlation with $1/N_{sub}$ was observed for all parametric sweeps. For example, a time step of $\Delta s = 0.0035$ is examined over a range of subiterations from 10 to 80. As the inverse of the number of subiterations, $1/N_{sub}$, approaches zero, the accuracy of the simulation to predict these events can be extracted (Fig. 35). The $1/N_{sub} \to 0$ separation and reattachment event times are noted on the lift coefficient hysteresis plot for the VR7 $k = 0.10$ results (Fig. 34(a)). This linear behavior was also confirmed for a higher reduced frequency of $k = 0.20$ (Fig. 36) for the VR7 airfoil, as well as for a NACA0012 that was tested at a reduced frequency of $k = 0.145$ and Mach number of 0.302 with a different angle of attack scheduling (Fig. 37). As noted previously for some of the integrated performance quantities, the prediction of the event location in the limit may not result in most accurate correlation with experiment, but instead provides an evaluation of the converged accuracy of the numerical simulation.

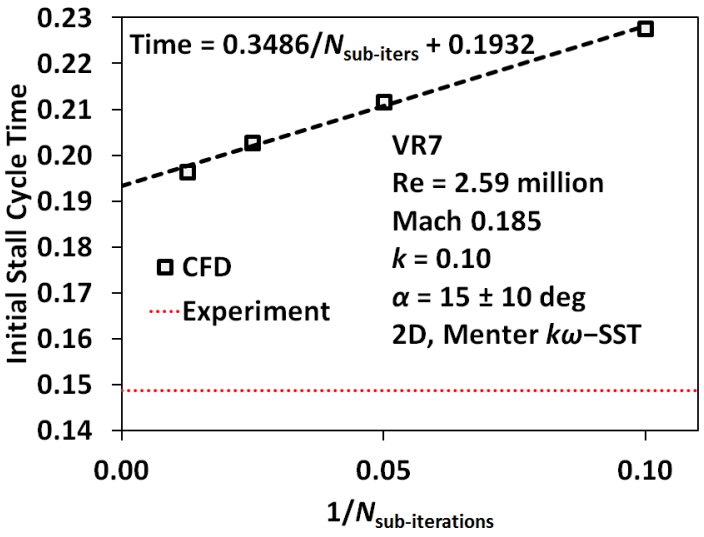

(a) Time of initial stall event

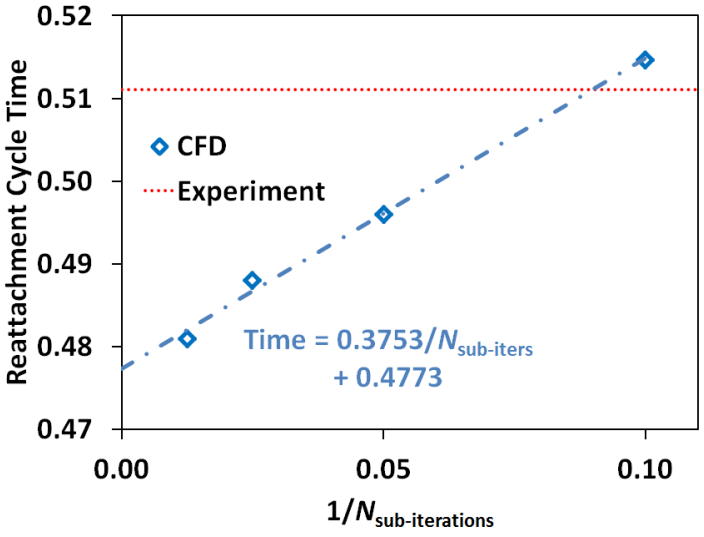

(b) Time of reattachment

Figure 35: Variation of predicted dynamic stall cycle time for stall and reattachment events for VR7 airfoil at a reduced frequency of $k = 0.10$.

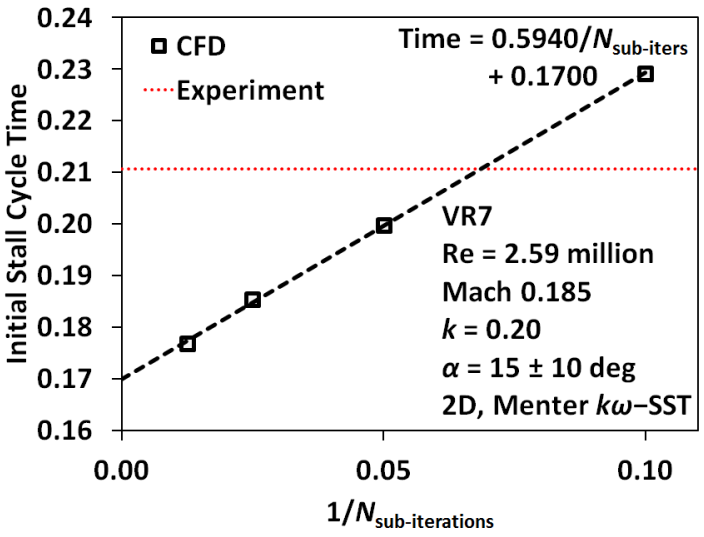

(a) Time of initial stall event

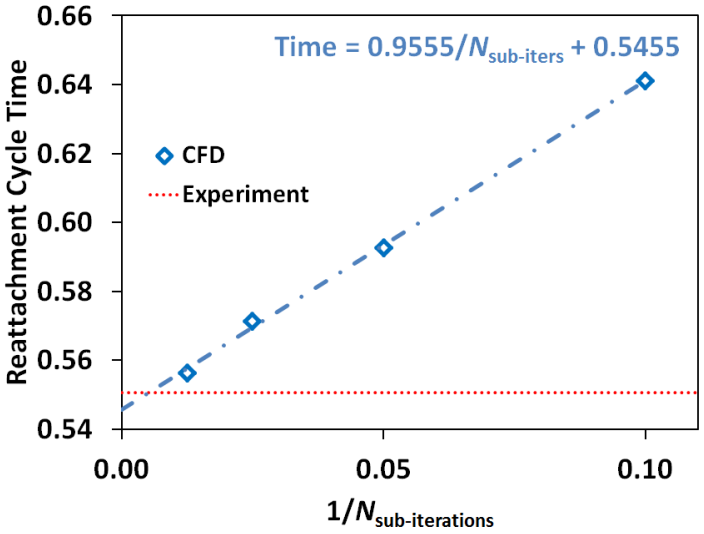

(b) Time of reattachment

Figure 36: Variation of predicted dynamic stall cycle time for stall and reattachment events for VR7 airfoil at a reduced frequency of $k = 0.20$.

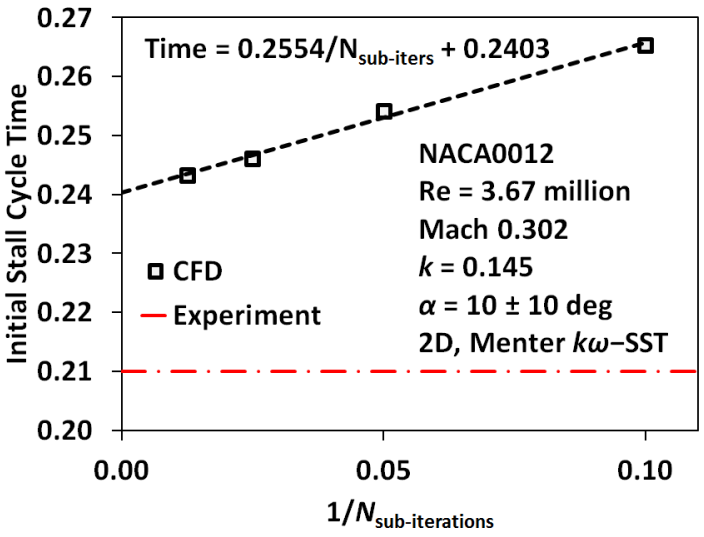

(a) Time of initial stall event

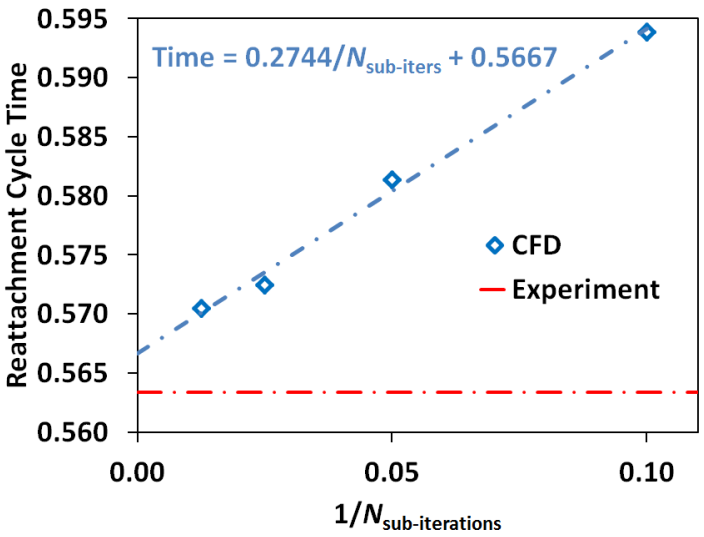

(b) Time of reattachment

Figure 37: Variation of predicted dynamic stall cycle time for stall and reattachment events for NACA0012 oscillating airfoil at a reduced frequency of $k = 0.145$.

6.6.3 Turbulence Subiteration Convergence

Given the sensitivity of the predictions to the mean flow subiterations, the effect of increasing the number of subiterations for the turbulent transport properties was investigated. Using 10 and 20 mean flow subiterations, the turbulent transport equations were further solved using 1– 8 subiterations for each mean flow subiteration. The attached, separated, and reattachment regions were each considered.

To explore the impact of the turbulent subiterations, their influence on the boundary layer behavior was analyzed. There was minor impact ($\leq$1.8% change) when the flow was attached (Figs. 38 and 39), but significant variations were noted when the flow was stalled (Figs. 40 and 41). Clearly the solution is not converged with 10 mean flow subiterations, as increasing the number of turbulence subiterations drastically influences the boundary layer behavior, as illustrated by the tangential velocity (Fig. 40(a)), turbulent kinetic energy (Fig. 40(b)) and the shear stress (Fig. 40(c)) profiles. The boundary layer convergence is clearly reflected in the integrated coefficient predictions (Fig. 42). The flow is converged with respect to number of turbulent subiterations to within 3.5% of the most accurate data on the upstroke at an angle of attack of 15 deg, but strong dependence on the number of turbulent flow subiterations is exhibited with separated flow on the downstroke. The same behavior can be observed in predictions with 20 mean flow subiterations (Figs. 41 and 43), although the variances are not as pronounced as the mean flow subiterations have advanced the overall solution closer to convergence. It is clear that the convergence of the turbulent kinetic energy and shear stress within the boundary layers should be examined when considering convergence of separated flows.

In the vicinity of reattachment, boundary layer profiles reveal little dependence on the number of turbulence subiterations for either the 10 (Fig. 44) or 20 (Fig. 45) mean flow subiteration cases. While the boundary layer was not converged with 10 mean flow subiterations, increasing the number of turbulence subiterations did not result in substantial modification of the boundary layer behavior. With 20 mean flow subiterations, the boundary layers were already converged. The integrated coefficients (Figs. 42 and 43) similarly have a stronger dependence on the number of mean flow subiterations than turbulent flow

subiterations, more than doubling in magnitude with increased mean flow subiterations for the drag and moment. These results indicate that convergence of the mean flow, rather than turbulence, is the necessary condition to accurately predict reattachment. This study quantified the observations of previous authors [56, 57], who noted a stronger sensitivity of reattachment with the number of mean flow subiterations. One characteristic of the coefficient hysteresis plots is the non-monotonic convergence with respect to the number of turbulent subiterations when the flow is massively separated. Completely monotonic convergence may not be necessarily expected in the event of a highly nonlinear flow, such the flow about an airfoil in deep stall. In addition, URANS approaches can result in overshoots in the integrated coefficients, which can magnify any non-monotonic convergence characteristics of the sensitive nonlinear flow.

As might be expected from the prior analyses, the separation point also exhibits a strong dependence on the number of turbulent and mean flow subiterations (Fig. 46). During deep stall (Fig. 46(a)) the separation point is very close to the leading edge. The influence of the additional turbulent subiterations is in direct proportion to the converged boundary layer with the mean flow subiterations. With ten mean flow subiterations, the boundary layer convergence was improved with additional turbulent subiterations, and the predicted location of stall separation moved as much as 10-15%. However with twenty mean flow iterations, the boundary layer was close to convergence, and the addition of further turbulent subiterations influenced the separation point $\leq 2\%$. The location of the separation point varies with the addition of turbulent subiterations. This variation in the location for this particular case does not permit an estimation of convergence with this parameter (number of turbulent subiterations); however, this may not be true for other airfoils and dynamic stall conditions. In the reattached flow region on the downstroke, some reversed flow is still observed on the upper surface of the airfoil. As with the separation point, the variation in the location of the flow reversal point (Fig. 46(b) was sensitive to the number of mean and turbulent flow subiterations characterizing the convergence of the boundary layer.

To assure convergence to the physical solution as the temporal integration was refined, comparisons with higher fidelity data were necessary. The predictions with 9,000

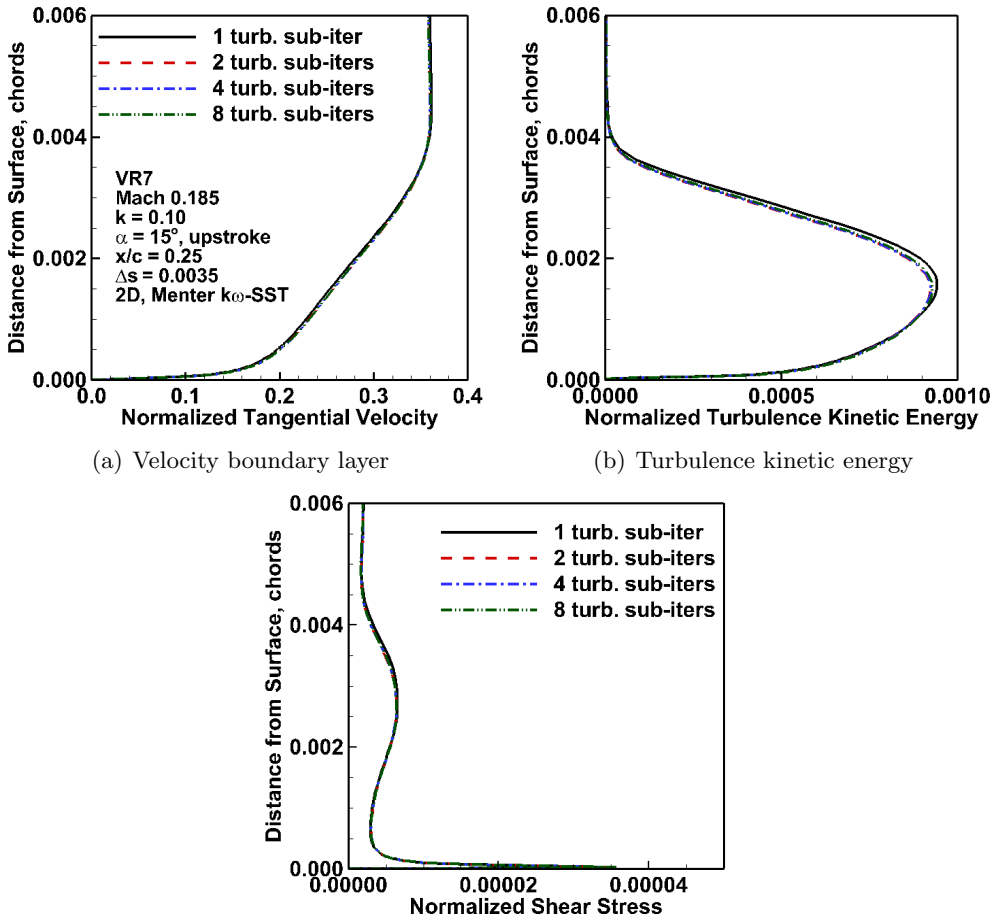

(a) Velocity boundary layer

(b) Turbulence kinetic energy

(c) Shear stress

Figure 38: Boundary layer convergence for the VR7 airfoil at $k = 0.10$ with 10 subiterations in the attached region ($\alpha = 15°$ up).

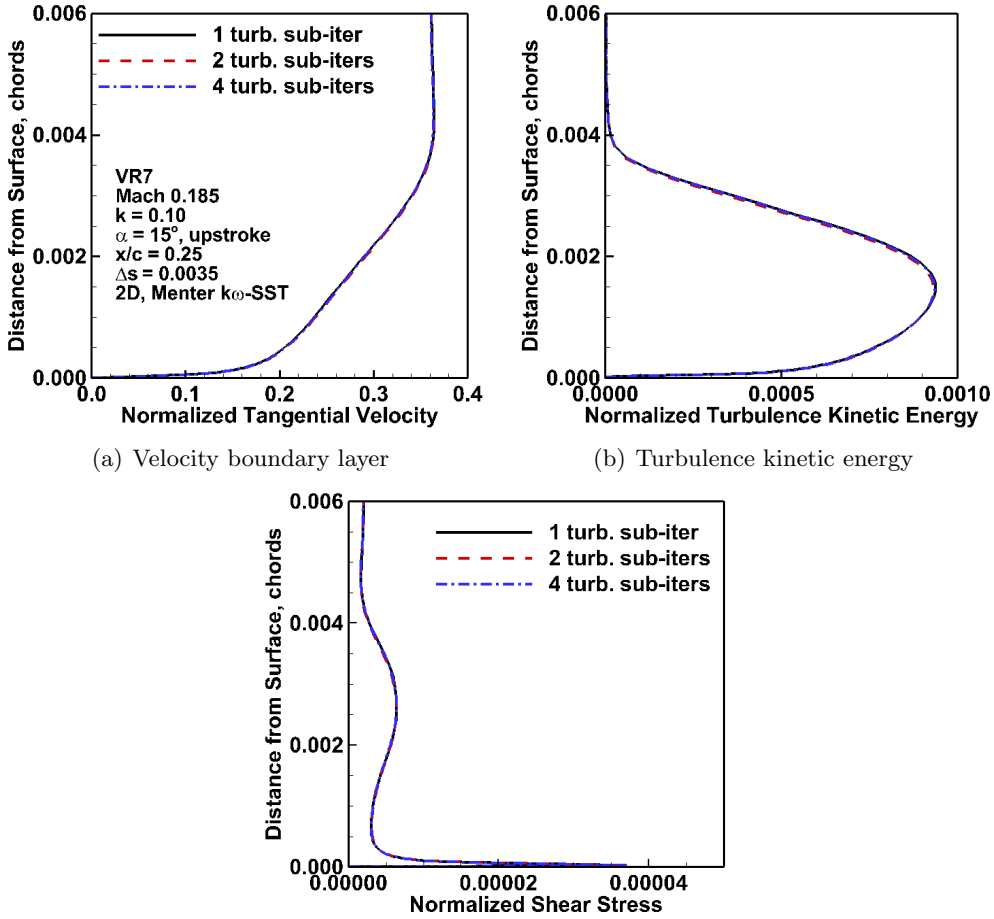

(a) Velocity boundary layer

(b) Turbulence kinetic energy

(c) Shear stress

Figure 39: Boundary layer convergence for the VR7 airfoil at $k = 0.10$ with 20 subiterations in the attached region ($\alpha = 15^\circ$ up).

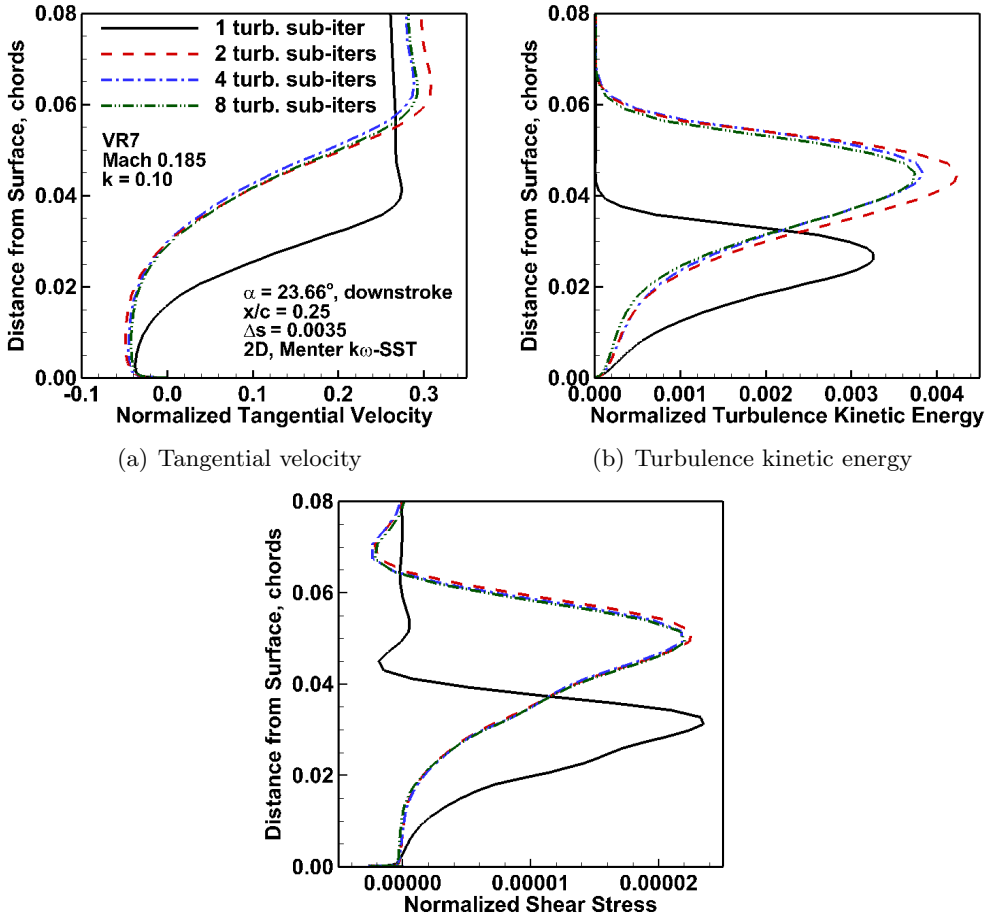

(a) Tangential velocity

(b) Turbulence kinetic energy

(c) Shear stress

Figure 40: Boundary layer convergence for the VR7 airfoil at $k = 0.10$ with 10 subiterations in the separated region ($\alpha = 23.66°$ down).

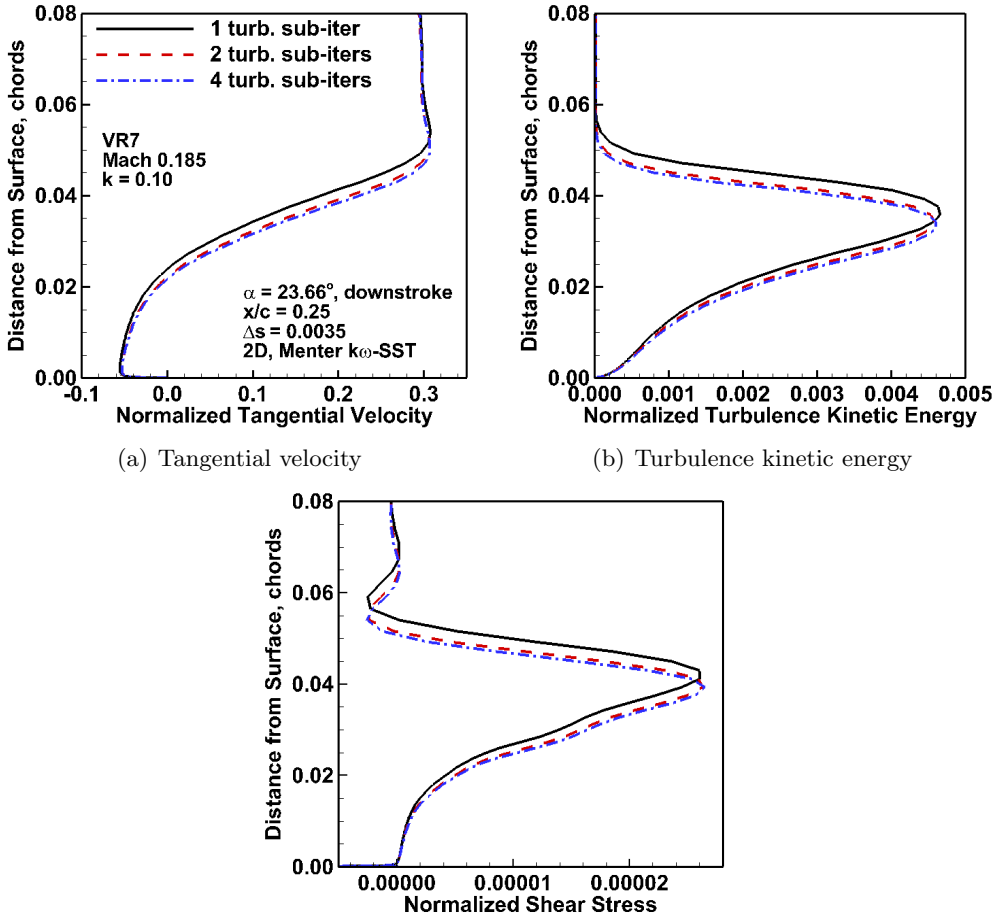

(a) Tangential velocity

(b) Turbulence kinetic energy

(c) Turbulence kinetic energy

Figure 41: Boundary layer convergence for the VR7 airfoil at $k = 0.10$ with 20 subiterations in the separated region ($\alpha = 23.66°$ down).

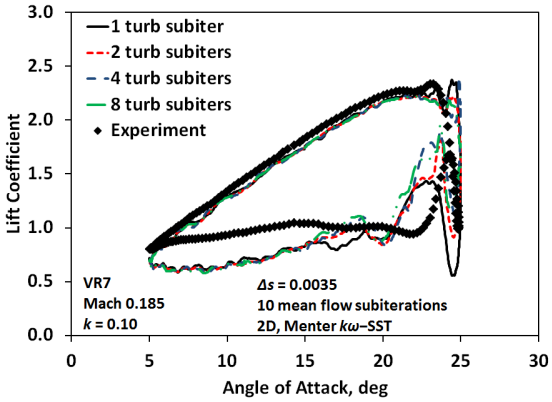

(a) Lift coefficient

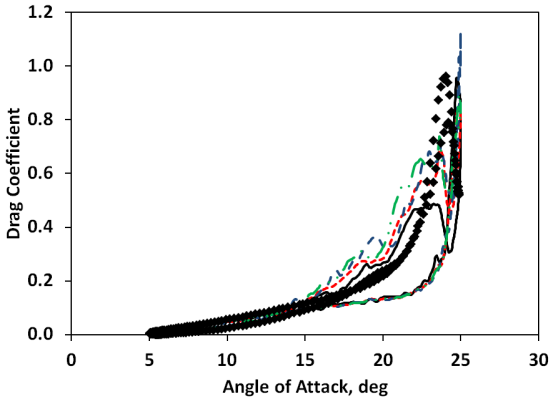

(b) Drag coefficient

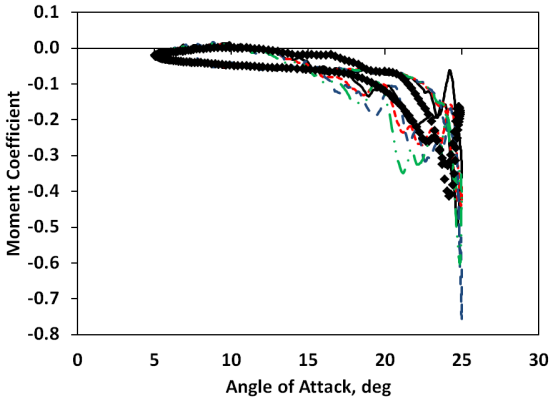

(c) Moment coefficient

Figure 42: Integrated coefficient hysteresis curve variation with turbulent flow subiterations for the VR7 airfoil at $k = 0.10$ with 10 mean flow subiterations.

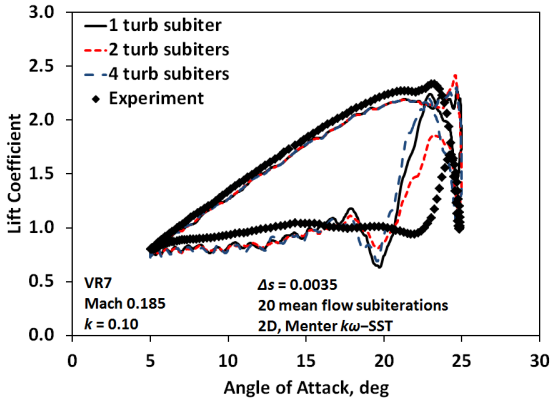

(a) Lift coefficient

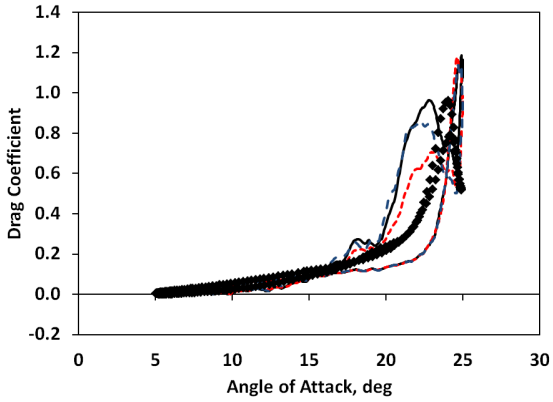

(b) Drag coefficient

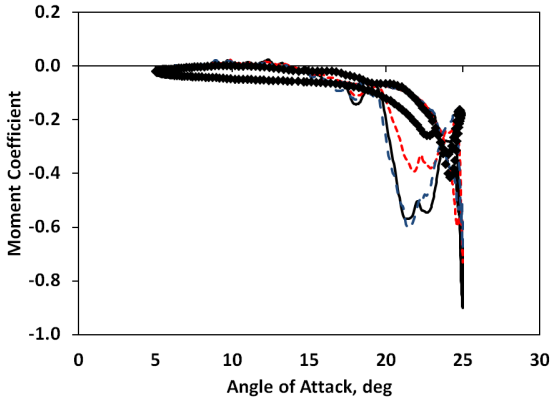

(c) Moment coefficient

Figure 43: Integrated coefficient hysteresis curve variation with turbulent flow subiterations for the VR7 airfoil at $k = 0.10$ with 20 mean flow subiterations.

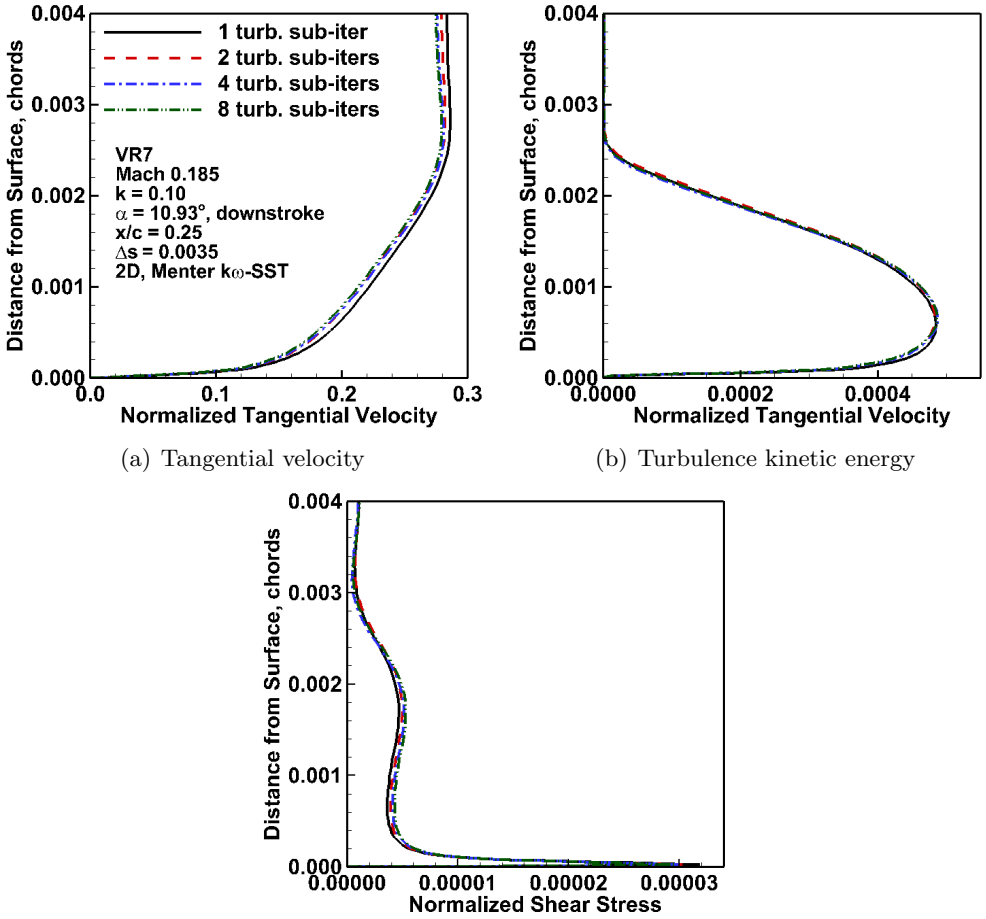

(a) Tangential velocity

(b) Turbulence kinetic energy

(c) Shear stress

Figure 44: Boundary layer convergence for the VR7 airfoil at $k = 0.10$ with 10 subiterations post-reattachment ($\alpha = 10.93°$ down).

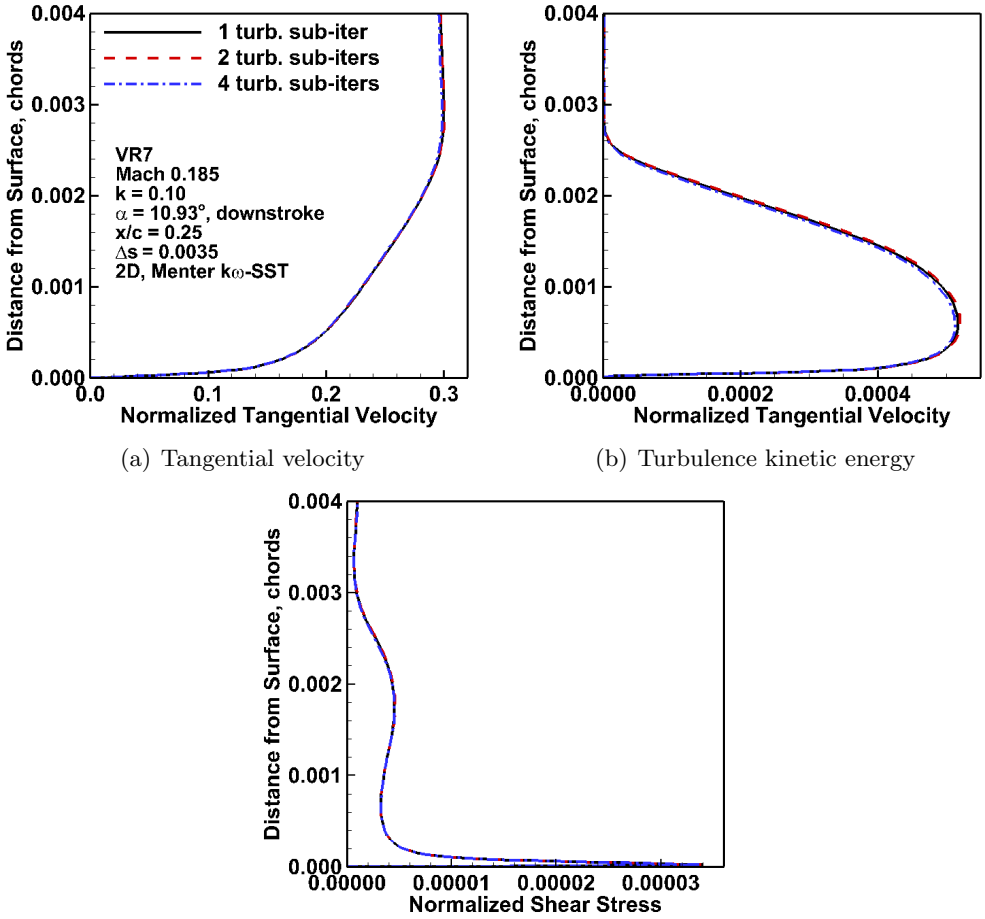

(a) Tangential velocity

(b) Turbulence kinetic energy

(c) Shear stress

Figure 45: Boundary layer convergence for the VR7 airfoil at $k = 0.10$ with 20 subiterations post-reattachment ($\alpha = 23.66°$down).

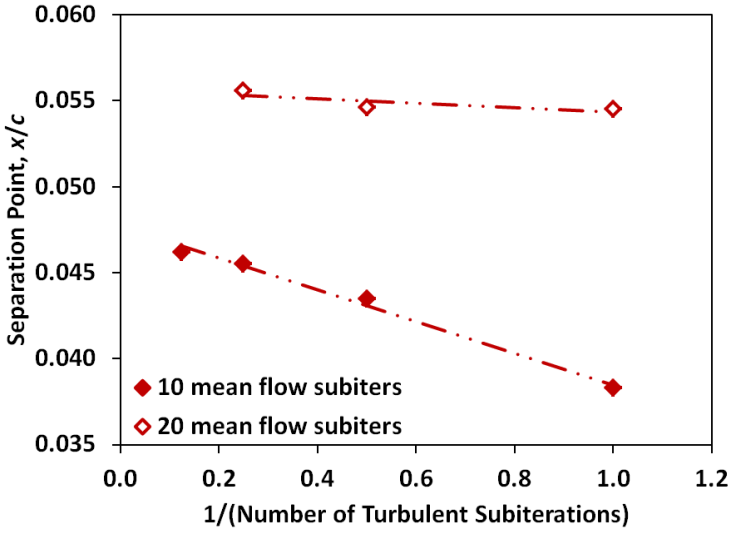

(a) Angle of attack of 23.66° on the downstroke

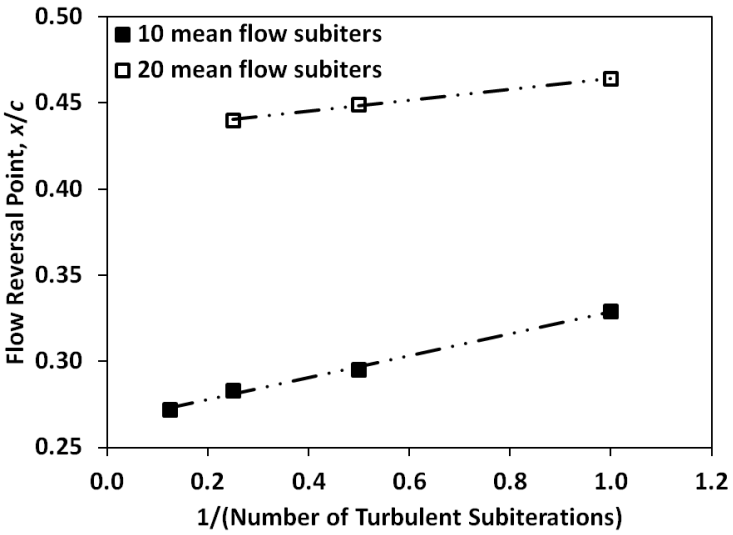

(b) Angle of attack of 10.93° on the downstroke

Figure 46: Variation of upper surface separation and flow reversal points with number of turbulent subiterations for stall and reattachment regions for the VR7 airfoil at $k = 0.10$, Mach 0.185, $\Delta s = 0.0035$, 2D Menter $k\omega$-SST turbulence model.

steps/cycle, 20 mean flow subiterations, and 4 turbulent flow subiterations were compared with predictions obtained via 36,000 steps/cycle, 10 mean flow subiterations, and 1 turbulent subiteration per mean flow subiteration. The lift, drag, and moment hysteresis curves (Fig. 47) demonstrated the attached flow on the upstroke was completely converged, while reattachment on the downstroke was approaching the experimental data. Not unexpectedly results in post-stall before reattachment were highly sensitive to the temporal integration parameters.

Comparisons between boundary layers of the 9,000 steps/cycle, 20 mean flow subiterations, 4 turbulent subiterations data and the 36,000 steps/cycle, 10 mean flow subiterations, and 1 turbulent subiteration data were also carried out for stall and reattachment. Although post-stall boundary layer behavior (Fig 48) was highly sensitive to the temporal integration parameters as observed in the coefficient hysteresis curves, convergence of the coarser time integration results to the higher fidelity boundary layer behavior was verified. Reattachment (Fig 49) boundary layer behavior was more converged in these comparisons. In both post-stall and reattachment, the data exhibited differences as increased boundary layer thickness for the higher fidelity predictions.

The cost of each additional turbulence subiteration per mean flow iteration is only 19% the cost of an additional full solver iteration, whereas the cost of an additional mean flow sub-iteration is roughly 60% the cost of an additional full solver iteration. Therefore, a cost-benefit analysis of the turbulent subiteration-mean flow subiteration-time step combination is needed to determine the most efficient cost of the simulation for a given accuracy. The computational costs associated with this approach represent a lower bound based on convergence estimations of flow separation, reattachment, and convergence of boundary layer behavior.

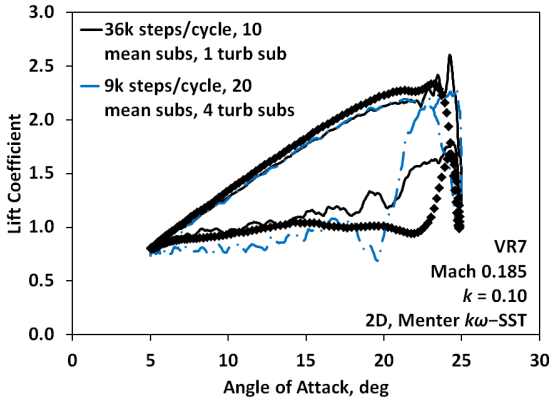

(a) Lift coefficient

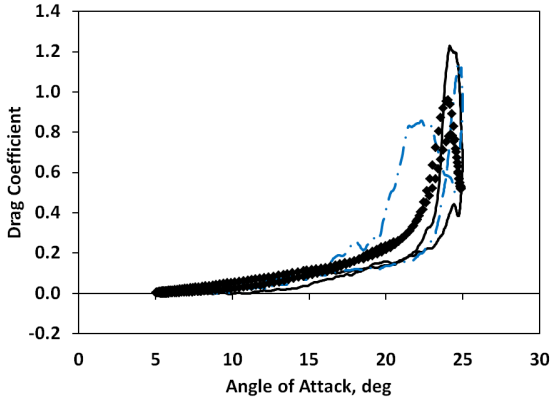

(b) Drag coefficient

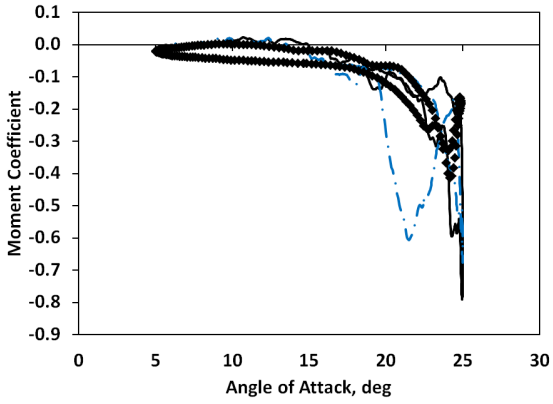

(c) Moment coefficient

Figure 47: Coefficient history for the VR7 airfoil in dynamic stall with $k = 0.10$ for varying integration parameters.

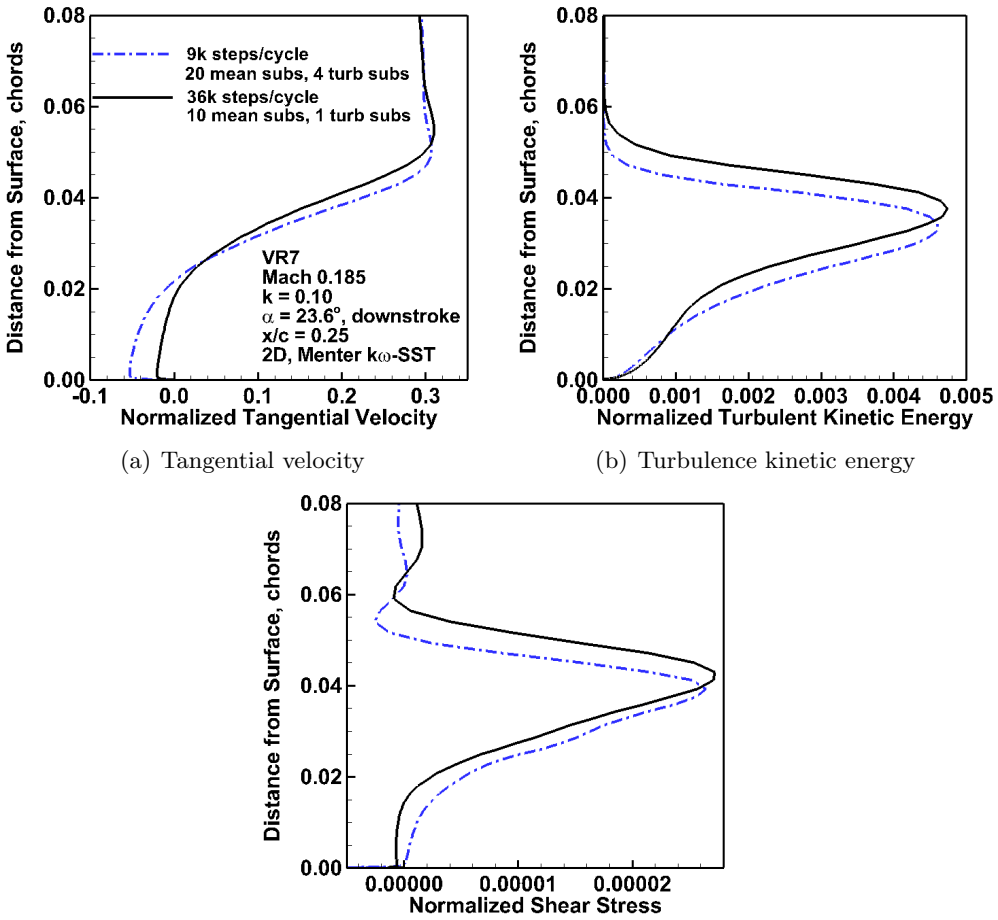

(a) Tangential velocity

(b) Turbulence kinetic energy

(c) Shear stress

Figure 48: Boundary layer convergence comparison for the VR7 airfoil in dynamic stall at $\alpha = 23.66°$ on the downstroke.

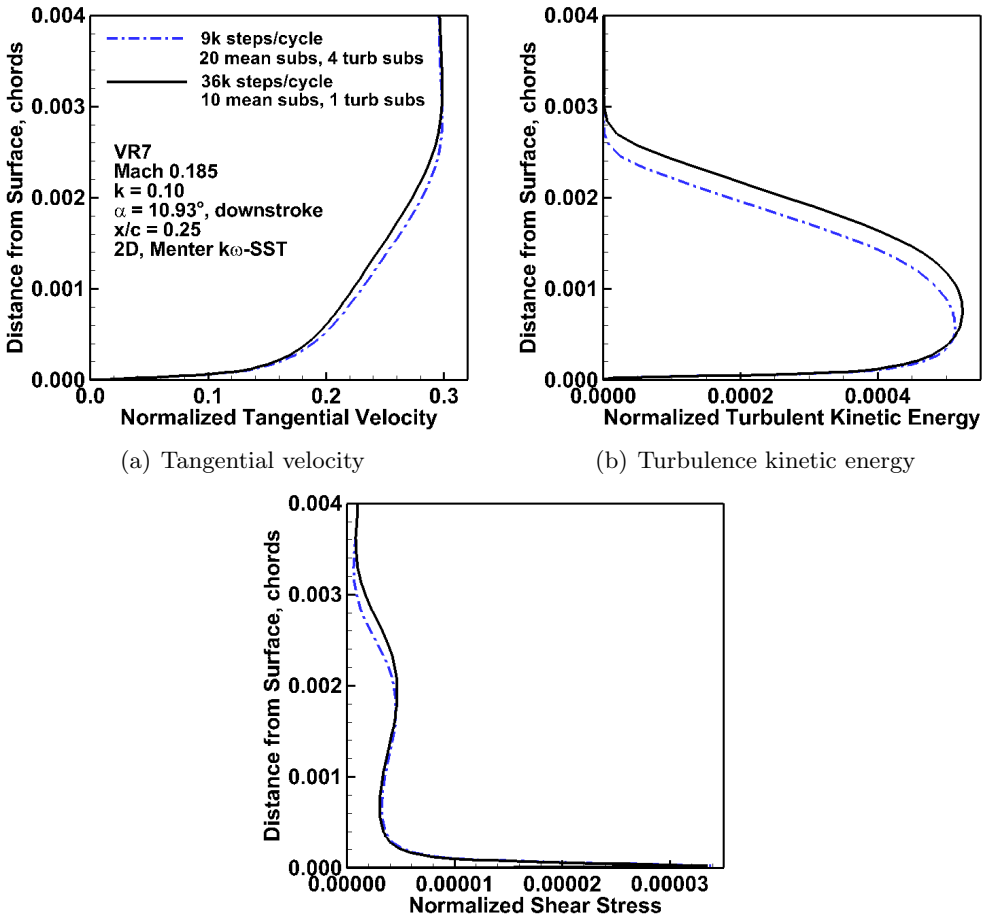

(a) Tangential velocity

(b) Turbulence kinetic energy

(c) Shear stress

Figure 49: Boundary layer convergence comparison for the VR7 airfoil in post-reattachment at $\alpha = 10.93°$ on the downstroke.

CHAPTER VII

TURBULENCE MODELING TO CAPTURE ACOUSTICS

7.1 Purpose

Validation of the computational approach and turbulence methodology may be achieved via reproduction of the physics of a cavity flow. Although geometrically simple, cavity flows exhibit complex physics including shear layer instability, flow induced resonance, and massive separation with a highly vortical flow field. Prediction of acoustic modes and the flow field within the cavity gives evidence of the ability of the computational approach to capture complex physical phenomena and turbulent flows.

7.2 Experimental Correlation

The generic cavity rig used by QinetiQ for a set of cavity experiments by Henshaw [1] was correlated to the computations in this study. The cavity was embedded in a rig mounted on a sting, and the pressures across the cavity floor were monitored at various free stream steady flows. These experiments have also formed the basis for correlation by a number of computational simulations [18, 43, 44, 86] using LES and detached eddy simulations with Spalart-Allmaras, $k-\omega$ SST, and $k-\varepsilon$ turbulence models. Each computational study has examined the mean or unsteady pressure at the cavity floor center.

The experimental study varied the depth of a rectangular cavity having a length of 0.508 m and a width of 0.1016 m. Shallow (0.0508 m) and deep (0.1016 m) cavity were examined. No cavity motion, inclination, or yaw was considered. The rig had a length of 1.8288 m with the leading edge of the cavity located at 0.7874 m, and a width of 0.4318 m with the cavity centerline offset by 0.0254 m from the rig centerline. Pressure measurements were taken using static pressure transducers along the cavity floor centerline at 10 locations and the rig centerline at 28 and 14 locations ahead and aft of the cavity, respectively.

Mach numbers of 0.6, 0.85, and 1.35 were studied with total pressures ranging from 101.65 to 102.55 kPa and total temperatures from 302.32 to 311.35 K. This study examined

the Mach 0.85 case near sea-level standard atmospheric conditions with a total pressure of 101.65 kPa and total temperature of 302.32 K as a Reynolds number of 1.38×10^7. The static temperature from isentropic relations was then 263 K, resulting in a flow speed of 276 m/s.

7.3 Computational Setup

The simulations were performed using the OVERFLOW 2.1z [67] flow solver. The spatial and numerical scheme utilized were a 4^{th}-order central-difference Euler scheme. The temporal scheme utilized was an ARC3D diagonalized Beam-Warming scalar pentadiagonal scheme with 2^{nd}-order Newton sub-iterations utilized. Additionally, artificial viscosity was added in the form of a 4^{th}-order generalized thin-layer Navier-Stokes (TLNS3D) dissipation scheme. This dissipation scheme adds smoothing to ρh_0 in the form of dissipation coefficients to the 2^{nd} and 4^{th}-order discretization of the spatial derivatives.

The fluid composition assumes air is a perfect gas having a constant ratio of specific heats of 1.4. The cavity simulations here were run with dimensional time steps ranging from 3.62×10^{-6} to 2.00×10^{-5} seconds for a total simulation time of up to 0.5 seconds, which is equivalent to a fluid element traveling 276 grid lengths or *residence periods*, the time required for a fluid particle to travel the length of the cavity at free stream velocity. A free stream turbulence intensity of 10% and normalized turbulent kinetic energy of 10^{-6} were prescribed to initialize the simulation. The temporal scheme was the ARC3D diagonalized Beam-Warming pentadiagonal scheme with two Newton sub-iterations having second-order accuracy. The spatial scheme used central difference Euler terms. The simulations were run using 4th-order spatial accuracy for a fully-viscous simulation including all cross terms. The TLNS3D dissipation scheme was used to smooth ρh_0, with second and fourth-order dissipation coefficients of 2.0 and 0.04, respectively.

The results of the simulations are compared in terms of the aeroacoustics and convergence of integrated force and moment coefficients. The aeroacoustic behavior for the cavity is determined by applying Fourier transforms to the pressure data at the cavity floor center. The peak frequencies and amplitudes for each turbulence technique are recorded from the

transformed data and compared to experimental values in terms of their relative errors. The simulation pressure data are recorded at each iteration. For the experimental data, unsteady pressure information is gathered at sensor locations using Kulite pressure transducers with the data determined [1] to an uncertainty of 12 Hz. The data are also compared to the Rossiter frequency modes [87] as

$$f_n = \frac{U_\infty}{L} \frac{n - \gamma}{M_\infty + 1/\kappa} \tag{41}$$

The reference velocity, U_∞, and reference Mach number, M_∞, are the freestream velocity and Mach number, respectively. The values here are $U_\infty = 276m/s$ and $M_\infty = 0.85$. The reference length, L, is the stream-wise cavity dimension of 0.508 m. The parameters γ and κ are usually given by experiment with κ usually having a value of 0.57 and γ having a value between 0 for a deep cavity and 0.57 for a shallow cavity. The desired mode is calculated by setting n equal to the mode number. A value of $\gamma = 0.307$ is applied in this work to permit direct comparisons with Levasseur [18].

7.4 Grids

7.4.1 Setup

Cavity simulations provide validation of turbulence and analysis methodology for the airfoil/flap gap. Figures 50(a) and 50(b) show two-dimensional slices of the three-dimensional cavity grid. This grid is called grid 2R and corresponds to the grid used by Levasseur [18] to model this cavity called mesh M3. An overset approach is used with a refined grid to model the internal cavity and one second grid to model the area external to the cavity. The cavity grid extends 0.2422 m into the flow field grid and applies an overset approach to exchange information between the grids. There are 161 grid points along the length of the cavity, 188 grid points from the cavity floor to the overset boundary, with 73 of those grid points overlapping the flow field grid, and 115 grid points across the cavity width. Stretching and spacing between the cavity and external flow grids are matched for the overlap boundary at the cavity opening. It is worth noting these grids have stretching an spacing that is appropriate for a RANS grid. The stretching is larger than would be the case for LES

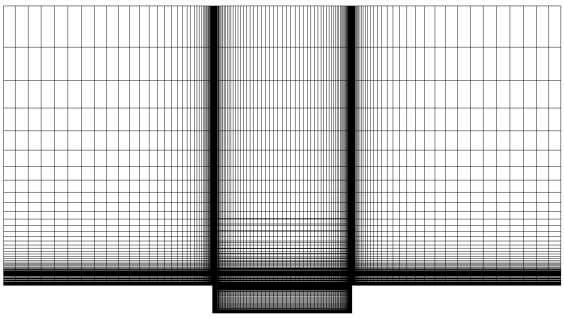

(a) Overall view of the cavity and external flow grids.

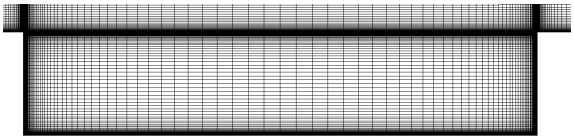

(b) Cavity grid close-up.

Figure 50: Cavity grid profile view.

simulations, as these simulations examine the ability of RANS grids to capture flow physics with a hybrid technique, rather than performing a traditional LES simulation.

The area (and grid) external to the cavity is 2.032 m (297 points) in the stream-wise direction, 0.6096 m (241 points) in the span-wise direction, and 1.016 m (95 points) in the direction normal to the external wall. The middle of the cavity opening is in the middle of the bottom external flow wall as seen in the grid orthogonal view (Fig. 51). The initial grid spacing normal to the wall for both grids is 3.0×10^{-6} meters, yielding a viscous grid spacing of $y^+ < 1.0$ at the wall. The wall and internal cavity surfaces are viscous modeled as adiabatic boundary conditions with pressure extrapolation. The inflow, outflow, and upper far field boundaries are resolved with free stream characteristic boundary conditions. The two side boundaries corresponding to the width axis of the cavity were treated as symmetry planes. The overset boundaries between the two grid used interpolation with three fringe points.

Simulations employ grid nodes clustered towards the center of the grid (Fig. 52) for the aforementioned mesh distribution dependence work. This grid has the same number of nodes and differs only in the distribution of these points.

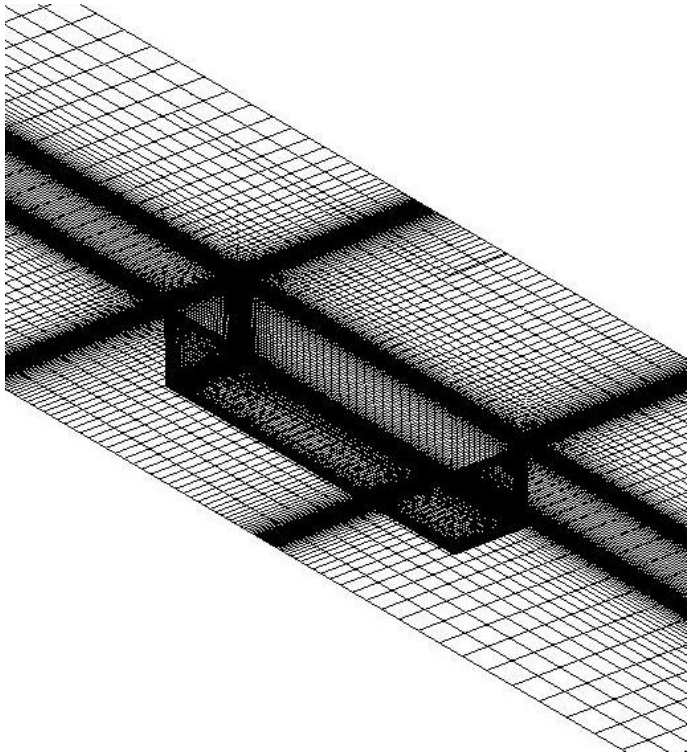

Figure 51: Cavity grid orthogonal view.

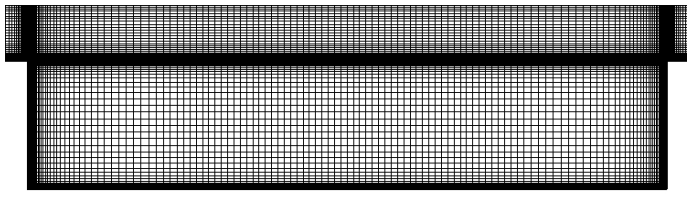

Figure 52: Cavity grid for node distribution analysis.

Table 4: Grid solution convergence with varying initial normal wall spacings.

Wall spacing m	Wall shear stress Pa	Viscous wall spacing
3.0×10^{-2}	0.8	351.7
3.0×10^{-3}	5.9	96.3
3.0×10^{-4}	44.0	26.3
3.0×10^{-5}	69.0	10.3
3.0×10^{-6}	86.7	0.92
3.0×10^{-7}	87.3	0.11

7.4.2 Grid Spacing Study

The influence of grid spacing on the simulations was examined via initial normal wall spacings with a rate of expansion of less than 15% to identify the normal and length spacing (the spacing in the direction of the width was constant). The largest aspect ratio at the wall varied from 0.128 for the coarsest normal spacing up to 12,800 for the finest normal spacing. The wall spacing was varied from 3.0×10^{-2} to 3.0×10^{-7} m, resulting in refined grid. For each case, the wall stress was calculated from the gradient of the flow at the wall. Convergence of the shear stress was used as a criterion for the minimum necessary initial normal wall spacing in Table 4. With a shear stress change of 0.7% between the two finest spacings, an initial normal spacing of 3.0×10^{-6} is considered converged.

The grid setup used here is compared with other works such as a study by Allen [43] which has $y^+ < 300$, and simulations by Syed [44] which have $y^+ < 2$. It is clear that a large viscous spacing near 300 at the surface will not properly capture the surface physics; however, the viscous spacing near 2 may properly reproduce the near-wall flow. The average grid spacing of the different setups is similar where Allen, Syed, and this study have mesh spacings of 1.89×10^{-2}, 1.56×10^{-2}, 1.64×10^{-2} m, respectively, within the cavity.

7.4.3 Influence of the External Grid Domain

Experimental investigations of cavities, such as Ref. [88] have noted the interaction of the cavity with the downstream external flow. In subsonic free stream configurations, this interaction may influence the cavity behavior, and the numerical control volume should be large enough to include these potential interactions. To examine the influence of the

Table 5: Grid comparisons for small and large grid domains.

Grid	Stream-wise m, nodes	Span-wise m, nodes	Height m, nodes
1R, External Flow	1.3208, 297	0.4064, 241	1.016, 95
2R, External Flow	2.0320, 297	0.6096, 241	1.016, 95
1R and 2R, Cavity	0.508, 161	0.1016, 115	0.1016, 115 +0.1406 overset, +73

external grid domain on the analysis, two meshes with different far field boundary locations were compared, similar to the analysis by Levasseur [18]. Results from the grid discussed previously were compared to results from a grid with 1.016 m height, 1.3208 m in the stream-wise direction and 0.4064 m in the span-wise direction. The cavity dimensions were not modified. The grid extents for both grids are listed in Table 5. The computational and physical extents of both the external flow grids and the cavity grid are listed. The computational mesh sizes of the grids are not altered between grid 1R and grid 2R. The simulations performed by Levasseur [18] are different from this study as Levasseur uses unstructured grids, whereas grids 1R and 2R are structured grids. The unstructured meshes in the study by Levasseur have 3×10^6 elements for the coarse M1 mesh and 9×10^6 elements for the fine M3 mesh. The physical dimensions of Levasseur's meshes M1 and M3 are the same as grids 1R and 2R, respectively, from Table 5. In the LES study by Levasseur [18], M1, the smaller domain grid, does not obtain as high a quality solution as the larger domain grid, and the similar conclusions may be drawn here using the hybrid RANS/LES method. The pressure histories for the two simulations are shown in Fig. 53. The 1R pressure predictions do not contain the larger and longer period oscillations found in the 2R pressure history. The shorter period oscillations are apparent, but these oscillations are not as large in magnitude as the simulations which use the 2R grid.

The influence of the extent of the external domain can observed via the location of the harmonics of the pressure at the midpoint of the cavity floor, tabulated in Table 6. The peak frequencies are compared to experimental values which have an error of 12 Hz. This error corresponds to 3.4% of the total for the low frequency peak 2 and 1.4% of the total for the high frequency peak 4. While the current simulation using the smaller extent grid has

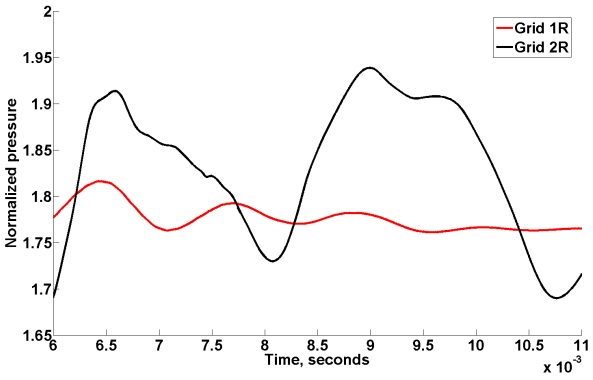

Figure 53: Pressure history at the cavity floor center for the smaller flow field cavity setup.

about 1/3 the LES error for peak 2, the size of the errors at higher harmonics is 3–5 times larger than the error of the LES simulation. The smaller domain simulations using both LES and hybrid RANS/LES methods result in errors up to 25–30% of the experimental values, which is not acceptable for engineering accuracy. The results applying the larger domain mesh, M3, are also listed in Table 6. The errors for the current simulations with the M3 mesh are of the same order as the LES simulations. While the LES predictions indicated the largest improvement with the M3 mesh for the lowest frequency peak, the current methodology predictions had the most improvement at the highest frequency peak with the different meshes.

Data are not available for peak 1, as the low frequency requires much longer simulation to accurately capture, and for many applications the higher harmonics are of more interest. The increase in grid fidelity from the coarse to the fine meshes can result in a drop in error in the prediction of the frequency peaks of an order of magnitude, validating the use of a larger and more costly grid domain. Considering the 12 Hz error in the experiment and uncertainty in the frequency transform, the predictions using the 1R grid do not fall within the prediction error bounds, however, the predictions using the 2R grid fall within the prediction error bounds.

7.5 Spectral Estimation

The desire to properly capture acoustics within the flow necessitates an analysis of the approaches employed to determine the frequency spectrum. Up to this point in the study,

Table 6: Mesh 1 peak frequencies at the cavity floor center.

Data source	Mesh	Peak 2 Hz	Error %	Peak 3 Hz	Error %	Peak 4 Hz	Error %
Experiment [1]	-	353±12	-	594±12	-	838±12	-
LES [18]	M1	462	30.9	625	5.2	873	7.1
KES	1R	337	-4.5	675	13.6	1012	24.5
LES [18]	M3	362	2.5	594	0.0	813	3.1
KES	2R	377	6.8	628	5.7	844	3.8
HRLES-sgs	2R	379	7.4	611	2.9	846	4.0

traditional FFT has been applied; however other methods should be consideration. The Burg method of spectral estimation [89, 90] is designed to improve the power spectrum prediction of a temporal series. Studies of vortex frequencies within shear flows [91] and acoustics of cavity flows [18, 92] have utilized the Burg method and proven its applicability in fluid dynamics. There are several benefits these studies have demonstrated with using this approach, which include a smoother spectral estimation depending on the order of the analysis, reducing unwanted noise, and reduced requirements on the amount of data necessary to obtain a spectrum. Caution must be exercised with respect to this approach, as spectral peaks may be split giving spurious modes. This is a concern when a higher order analysis is used, and care must be taken in choosing the length of the filter. A review of the Burg spectral estimation approach follows.

The pressures constitute a series, where p_n is the n^{th} value and the sampling period is Δt. The autocorrelation of these pressure is

$$\phi(\tau) = \lim_{T\to\infty} \frac{1}{2T+1} \sum_{n=-T}^{T} p_n p_{n+\tau} \tag{42}$$

The power spectrum of this pressure series is defined as

$$P(f) = \frac{1}{W} \sum_{\tau=-\infty}^{\infty} \phi(\tau)\, cos\,(2\pi f \tau \Delta t) \tag{43}$$

Here, $W = \frac{1}{2\Delta t}$, and f is defined on the interval $(0, W)$. The entropy of this power spectrum is related to

$$\int_0^W log\,[P(f)]\, df \tag{44}$$

The goal of this method is to determine the power spectrum that has the maximum entropy, but is constrained so that the spectrum agrees with the autocorrelation values. This

constraint can be written mathematically as

$$\int_0^W P(f)\, cos(2\pi f \tau \Delta t)\, df = \phi(\tau) \tag{45}$$

This maximum entropy spectrum is

$$P(f) = \frac{\frac{P_{N+1}}{W}}{\left|1 + \sum_{n=1}^{N} \Gamma_{n+1} e^{-i2\pi f n \Delta t}\right|^2} \tag{46}$$

The unknown Γ_{n+1} and P_{n+1} parameters are obtained from the matrix of autocorrelation values satisfying the relationship

$$\begin{bmatrix} \phi(0) & \phi(1) & \cdots & \cdots & \phi(N) \\ \phi(1) & \phi(0) & & & \vdots \\ \vdots & & \ddots & & \vdots \\ \vdots & & & \phi(0) & \phi(1) \\ \phi(N) & \cdots & \cdots & \phi(1) & \phi(0) \end{bmatrix} \begin{bmatrix} 1 \\ \Gamma_2 \\ \vdots \\ \Gamma_N \\ \Gamma_N + 1 \end{bmatrix} = \begin{bmatrix} P_{N+1} \\ 0 \\ \vdots \\ 0 \\ 0 \end{bmatrix} \tag{47}$$

The key component of spectral estimation is the evaluation of the autocorrelation values. Autocorrelation of this series may be estimated by Eq. 42. The problem with this estimation lies in the implicit assumption that the data before and after the limits of the series are either zero or repeat periodically. Burg avoids this edge distortion by directly relating the autocorrelation coefficients to the power. These filter parameters values are then determined in a recursive manner beginning with a two-point autocorrelation prediction error. The filter of the pressure defined by $p_{i+1} + \Gamma_1 p_i$ has a total forward and backward squared error of

$$P_2 = \frac{1}{2(N-1)} \left[\sum_{i=1}^{N-1} (p_{i+1} + \Gamma_1 p_i)^2 + \sum_{i=1}^{N-1} (p_i + \Gamma_1 p_{i+1})^2 \right] \tag{48}$$

The minimum error is achieved when the filter parameter is

$$\Gamma_1 = -\frac{2\sum_{i=1}^{N-1} p_i p_{i+1}}{p_1^2 + 2\sum_{i=2}^{N-1} p_i^2 + p_N^2} \tag{49}$$

The next level of recursion begins with the error of a three-point filter

$$P_3 = \frac{1}{2(N-2)} \left[\sum_{i=1}^{N-2} (x_{i+2} + \Gamma_2 x_{i+1} + \Gamma_3 x_i)^2 + \sum_{i=1}^{N-1} (x_i + \Gamma_2 x_{i+1} + \Gamma_3 x_{i+2})^2 \right] \tag{50}$$

A value of $\Gamma_2 = \Gamma_1(1 + \Gamma_3)$ is substituted to guarantee the estimate of the one-point autocorrelation agree between the two and three-point predictions. The minimization of

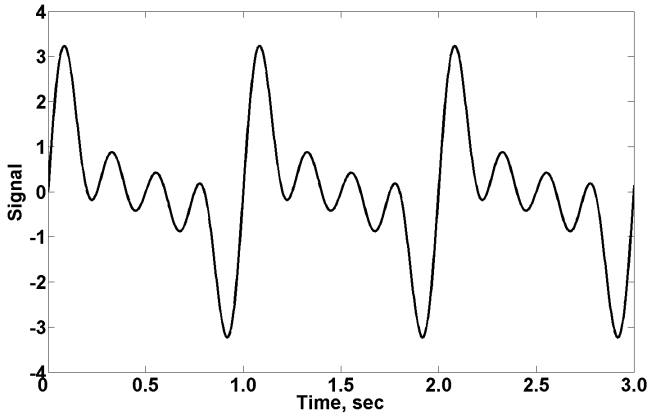

Figure 54: Known signal for Burg analysis.

P_3 gives the prediction parameter Γ_3. Along with the previously calculated Γ_1, Γ_2 can be calculated completing knowledge of the three-point parameters.

In a similarly recursive manner the parameters of the filter up to the desired order of prediction are determined. This procedure is continued until the desired number of filter points (the order) of the system is reached. These parameters are substituted into Eq. 46 to obtain the estimation of the power spectrum. To assess the predictive capability of Burg's method, a pressure signal is constructed from four modes using the equation

$$p(t) = \sin(2\pi \cdot 1 \cdot t) + \sin(2\pi \cdot 2 \cdot t) + \sin(2\pi \cdot 3 \cdot t) + \sin(2\pi \cdot 4 \cdot t) \tag{51}$$

The first three major cycles of this signal (Fig. 54) have visual evidence of each of the four modes used in its construction. The Fourier transform of Burg spectral estimation of this signal should provide four peaks in frequency space of equal amplitude situated at 1, 2, 3, and 4 Hz. A sample of this signal is taken with 400 collections per longest mode, and thus 100 samples per shortest mode. A total of 20 cycles of the longest mode are taken. This combination of sampling frequency and length should provide data to accurately reconstruct the signal in the frequency space.

By creating a known pressure history with exact modes and no noise, the effect of estimating the unknown portion of the signal at the edges can be assessed. For a two point prediction, this estimation is

$$p_i = p_{i-2} + \Gamma p_{i-1} + \epsilon_i \tag{52}$$

The coefficient Γ is found by the least squares method fitting across the entire *known* pressure, which does not include the unknown edge data. The error ϵ_i present in the estimation is the difference between the predicted and known signal, and is assumed to be of Gaussian distribution. As the order this method is increased, additional data are included from various modes of the signal.

The frequency spectrum of the constructed pressure history is determined using traditional Fourier transform and Burg's method with varying orders (Fig. 7.5). The Fourier transform correctly predicts the location of the modes within the uncertainty of the analysis, but the second and fourth modes are predicted with 27% less amplitude than the first and third modes. The predictive capability of Burg's method is highly dependent on the choice of order, but all spectral estimations have relatively smaller high frequency peaks. As the order increases from 75 to 100, the predictions improve. An order of 100 corresponds to including 1 cycle of the highest frequency mode in the prediction filter. As the order is further increased, attenuation of the higher frequency modes is apparent due to increased dependence of the prediction parameter on the longer period oscillations. The attenuation of higher harmonics across all estimations may be attributed to the large order needed to create a complex frequency reconstruction, which averages out the variations in the shorter modes. The sensitive dependence of Burg's method on order does not guarantee more accurate results than traditional Fourier analysis, but a comparison using the pressure history of the cavity is desired.

A comparison of the results of the cavity simulation using the LES type grid analyzed using Burg's methods with varying orders (Fig. 56) demonstrates sensitivity of the method to the chosen order. At the lowest order of 500, the spectrum has a high degree of smoothing with variation in the data reduced, whereas at the highest order of 2000 the data show spurious peaks and even a triple peak at the 594 Hz peak. An order of 1000 provides a balance between reproducing variability in the data without additional peak splitting. If no experimental data are available for order considerations, expected data may be appropriate depending on the application, such as the Rossiter modes in the case of cavity flow.

The results of Burg's spectral estimation using an order of 1000 as compared with

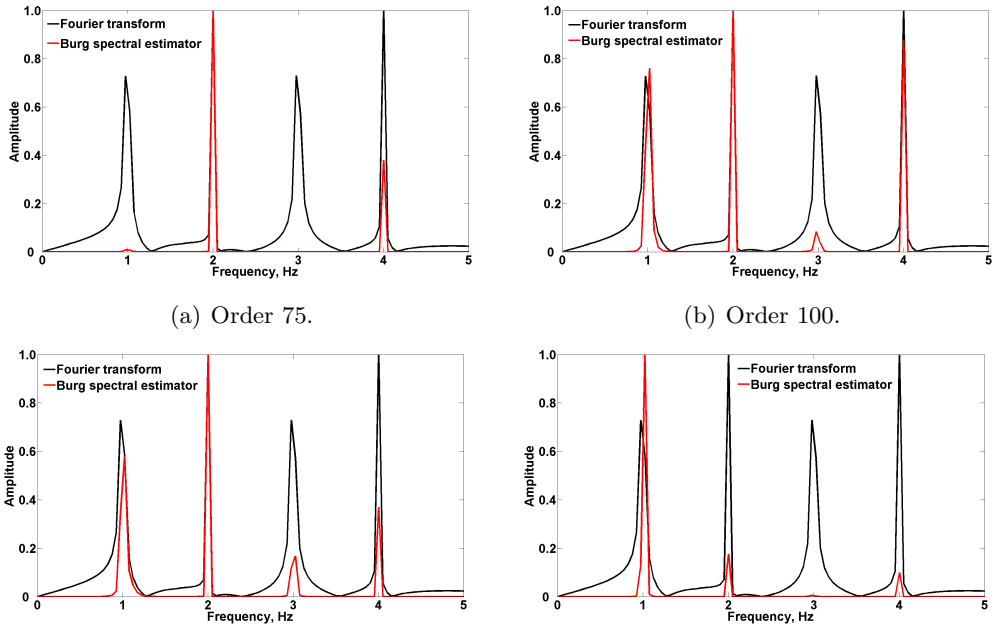

(a) Order 75.

(b) Order 100.

(c) Order 125.

(d) Order 150.

Figure 55: Differing node distributions for grid dependency analysis.

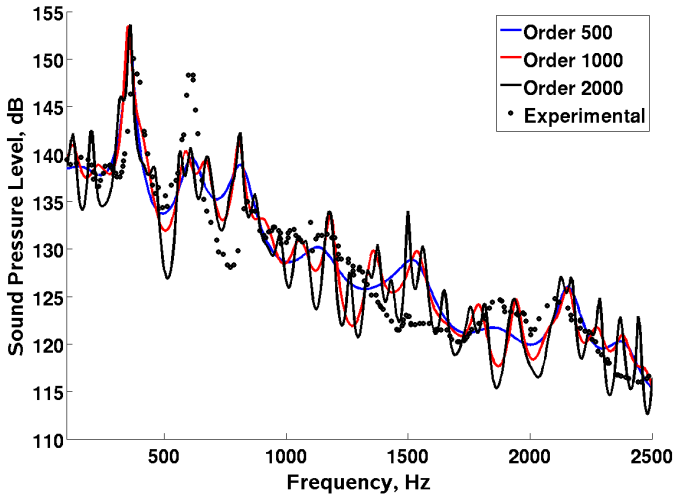

Figure 56: Sound pressure levels at the cavity floor center using Burg's method with varying orders.

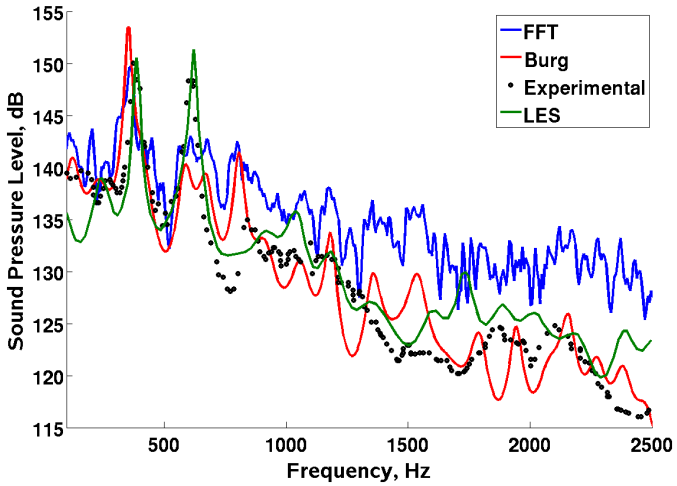

Figure 57: Sound pressure levels at the cavity floor center using Burg's method and FFT.

Table 7: Peak mode frequency error for differing spectral methods.

Mode	FFT Error %	Burg Error %
2	-3.9	-4.6
3	-0.4	-3.2
4	-4.6	-4.0

traditional FFT (Fig. 57) have much smoother sound pressure levels and attenuation at the higher frequencies. The predicted mode frequencies (Table 7) fall within the error bounds of the experiment and analysis. The similar predictions for the acoustics in terms of the mode frequencies and amplitudes (Tables 7 and 8) might lead to the conclusion that Burg's method is desirable, due to its smoother frequency spectrum, however, the sensitivity to the order creates a source of uncertainty in the approach. Therefore, the traditional FFT analysis is applied for the remainder of the analysis within this paper.

Table 8: Peak mode amplitude error for differing spectral methods.

Mode	FFT Error %	Burg Error %
2	-0.4	2.2
3	-3.7	-5.4
4	5.4	4.6

7.6 Flow Field Evaluation

In prior computational analyses, it was noted [93] that the RANS-based methods were able to capture the large flow field features but dissipated the vorticity over time. This behavior is examined here by comparing the flow fields from each of the different turbulence simulations at two different simulation times. In Fig. 7.6, the flow field vorticity at 8 ms is seen on the left, while the flow field 2 ms later is shown on the right. All methods capture the separation after the upstream corner of the cavity, leading to a recirculation region immediately behind the backward facing step and vortex shedding which reaches the downstream corner. Vorticity at the downstream corner travels either over the corner or towards the bottom of the cavity via the rear wall. The feedback loop of vorticity is reproduced in each set of data, however significant differences in the overall character of the flow fields for each simulation.

The traditional RANS flow field defines several vortical structures in the shear layer that have developed from the forward edge of the cavity. As time progresses, the vortices, as noted by vortex A, move downstream and impinge on the aft cavity wall. Vortices resulting from this wall impingement travel forward toward the front of the cavity, as illustrated by vortex B. One issue in this flow field is the high degree of dissipation. Although the flow separates at the upstream corner, separation is not apparent at the downstream corner and vorticity within the cavity is relatively weak. This field differs significantly from the DES-SST simulation, which captures a large amount of vorticity. This fact is attributed to the subgrid-scale modeling allowing resolution of eddies that are modeled in traditional RANS. In the DES-SST vorticity flow field in Fig. 58(b), vortex A travels downstream impinging on the corner, while vortices B and C are traveling upstream across the cavity floor. Although much more vorticity is captured by the DES-SST method, the GT-HRLES approach predicts stronger vortex cores. Moreover, the effect of the cavity extends further into the far field than the DES-SST results with more shed vorticity. Separation on the downstream corner is stronger for the GT-HRLES technique than DES-SST work. The KES simulation does not capture as complex of a flow field when compared with the hybrid RANS-LES data, but it captures more of the vortical structures than traditional RANS. The

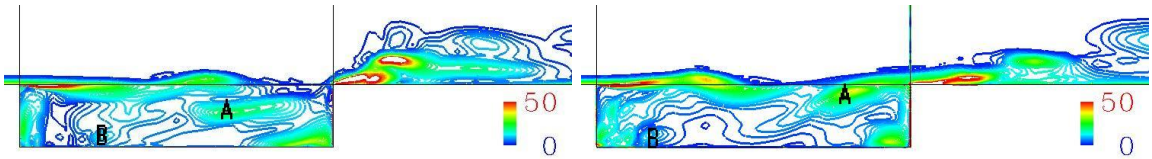

(a) Menter $k-\omega$ SST simulation.

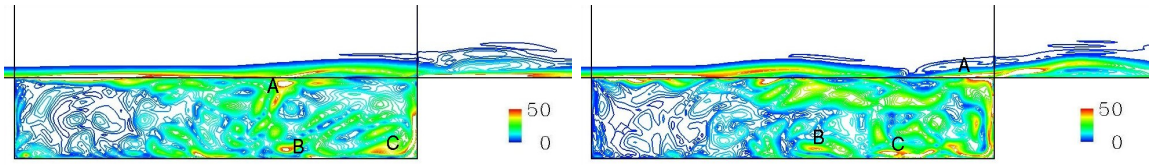

(b) DES-SST simulation.

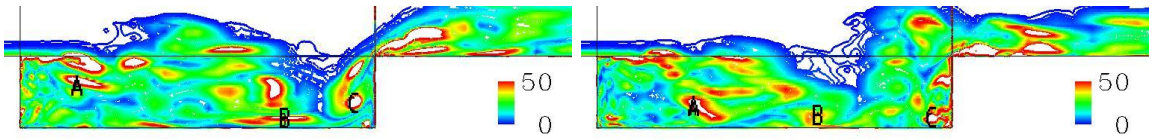

(c) GT-HRLES simulation.

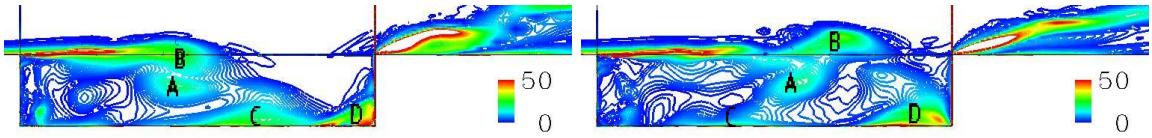

(d) KES simulation.

Figure 58: Predicted vorticity within the cavity of the Henshaw experiments[1] for different turbulence methods. The flow field at 8 ms is on the left and at 10 ms on the right.

vortex cores are weaker for the KES data than in the GT-HRLES case, but stronger than those acquired via the traditional RANS and DES-SST models. The shear layer downstream and cavity flow upstream vortex motion are clearly seen in vortices labeled A, B and C, D, respectively. The vorticity captured by the DES-SST and GT-HRLES simulations missing in the KES data may be attributed to the direct transport of turbulent dissipation in conjunction with subgrid-scale modeling in contrast to the KES method which scales the $(kl)^{sgs}$ term. Dissipation throughout the flow field is better preserved using the DES-SST and GT-HRLES methods, resulting in the flow field having many distinct vortices.

7.7 Flow Development

Initial investigation of subsidence of the initial flow transients of the integrated load coefficients for the simulations is presented for grid 2R. The cavity floor pressure was integrated

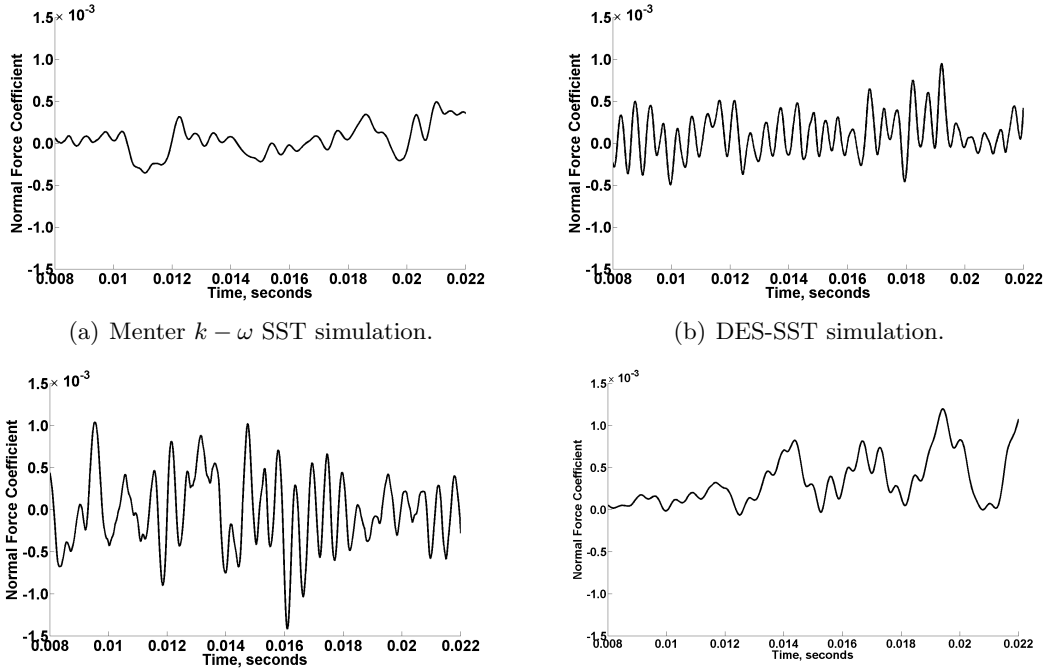

(a) Menter $k-\omega$ SST simulation.

(b) DES-SST simulation.

(c) GT-HRLES simulation.

(d) KES simulation.

Figure 59: Periodic development of normal force on the cavity floor.

over the cavity floor and normalized to coefficient form.

$$C_N = F_N / \left(\frac{1}{2} \rho_\infty U_\infty^2 S_{ref} \right) \tag{53}$$

As the pressure changes across the floor, the integrated normal force will provide a measure of the time at which the initial transients in the flow have died down. The coefficient of normal force is illustrated for each of the turbulence approaches (Fig. 7.7). In each case the coefficient of normal force shows some degree of oscillation resulting from the unsteady vortex structure within the cavity. The $k-\omega$ SST results have the weakest oscillations, as expected from the highly dissipative model. Variations for the DES-SST data are greater than for traditional RANS, but the GT-HRLES data demonstrate the largest multi-scale oscillations. The LES-VLES approach captures stronger oscillations than traditional RANS, but differs from DES-SST and GT-HRLES as it has differing transported properties.

The pressure histories at the cavity floor midpoint (Fig. 7.7) indicate a strong simple harmonic content over much of the time period, indicative of the influence of the vortical feedback loop, although the magnitude and phase of the pressure varies for each of the

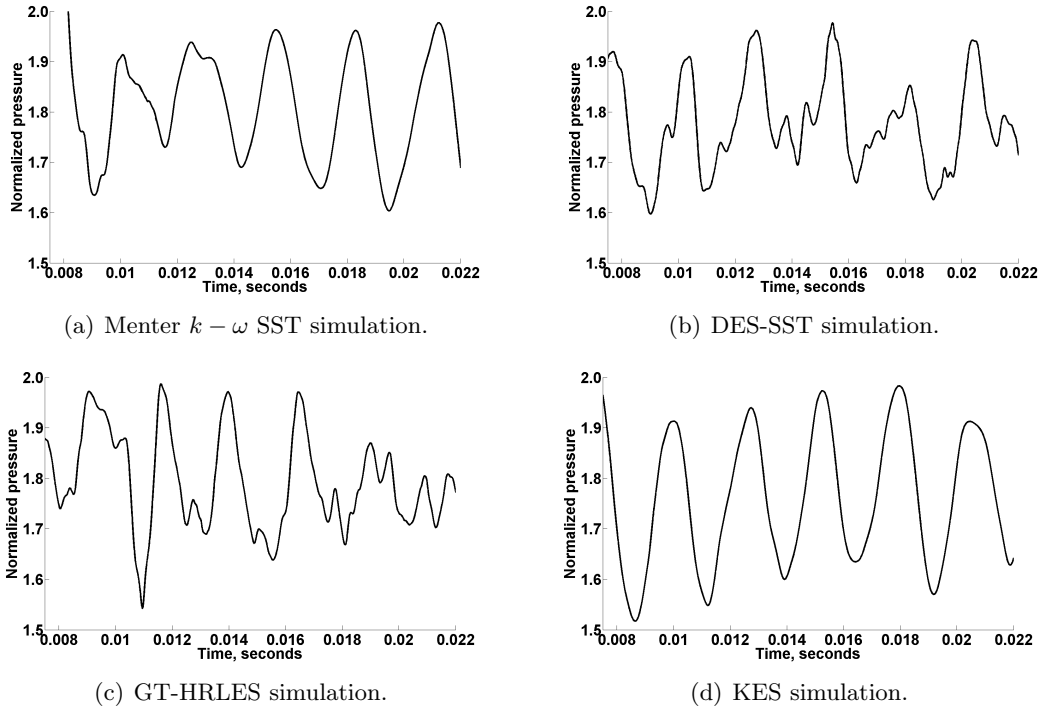

(a) Menter $k-\omega$ SST simulation.

(b) DES-SST simulation.

(c) GT-HRLES simulation.

(d) KES simulation.

Figure 60: Pressure history on the cavity floor.

three turbulence approaches. The DES-SST and GT-HRLES pressures also contain higher harmonics not present in the other two methods resulting from the higher vortical activity observed (Fig. 7.6).

The pressure histories were then analyzed by taking the frequency transform to obtain acoustic and frequency characteristics. Data analysis begins after the starting transients have exited the computational domain and periodicity in the solution is observed. Three different analysis intervals of 5.81, 11.70, and 17.36 residence periods that use subsequently more data from the pressure history trace were examined to ascertain the time required for the initial flow transients to subside. These intervals correspond to an integer-based number of pressure cycles from the pressure data in order to avoid biasing of the data.

The mean pressure on cavity floor (Table 9) provides a starting point in determining if the initial transients have died out, which is defined as when the mean pressure changes were less than 1.5% between analysis intervals. The mean pressure for the $k-\omega$ SST simulation final averaged value obtained is 2.9% higher than the mean pressure from the GT-HRLES simulation and 3.8% higher than the KES simulation predictions. The DES-SST results

Table 9: Mean pressures at the cavity floor center for OVERFLOW simulations.

Case	Pressure, 5.81 res kPa	Pressure, 11.70 res kPa	Pressure, 17.36 res kPa
$k-\omega$ SST	163.0	160.6	159.4
DES-SST	160.3	156.8	156.9
GT-HRLES	158.9	156.9	154.9
KES	151.8	152.8	153.5

fall between traditional RANS and the higher fidelity methods. This discrepancy between the RANS and hybrid results is explained by the dissipative nature of the RANS approach. The $k-\omega$ SST, DES-SST, and KES simulations have pressure changing less than 1.5% by the end of the analysis interval. For the GT-HRLES case, the simulation time was extended for an addition 8 residence periods to ensure the flow was fully developed. A change of less than 0.1% was computed when compared to the 17.36 residence period case confirming the fully developed cavity flow.

In addition to static pressure analysis, dependency of the solution on the interval of data analysis is necessary through the acoustic response of the flow. This analysis provides evidence that adequate data is contained to obtain a refined frequency spectrum. The frequency analysis of the pressure history data (Fig. 7.7) presents frequency characteristics in the form of the sound pressure levels. As expected, the results from the shortest (5) residence period analysis do not correlate well with the experimental data, as enough time is not included to resolve the harmonics. The traditional RANS data containing the longest time interval capture the frequencies of modes 2, 3, and 4, but do not accurately predict their amplitudes. The hybrid simulations indicate lower amplitude at very low frequencies, which are not observed in the RANS case, where the amplitude continues to increase as the frequency drops. For the KES simulation, the first two modes merge into one single mode for the shortest analysis interval, but become distinct as the analysis interval is increased. As the amount of pressure data increases with longer analysis intervals the harmonic content becomes more pronounced. Tables 10 and 11 for the frequency locations and amplitudes, respectively, indicate convergence to values that agree the with experimental results to within the error bounds. Experimental data, analytical predictions from Rossiter, and LES

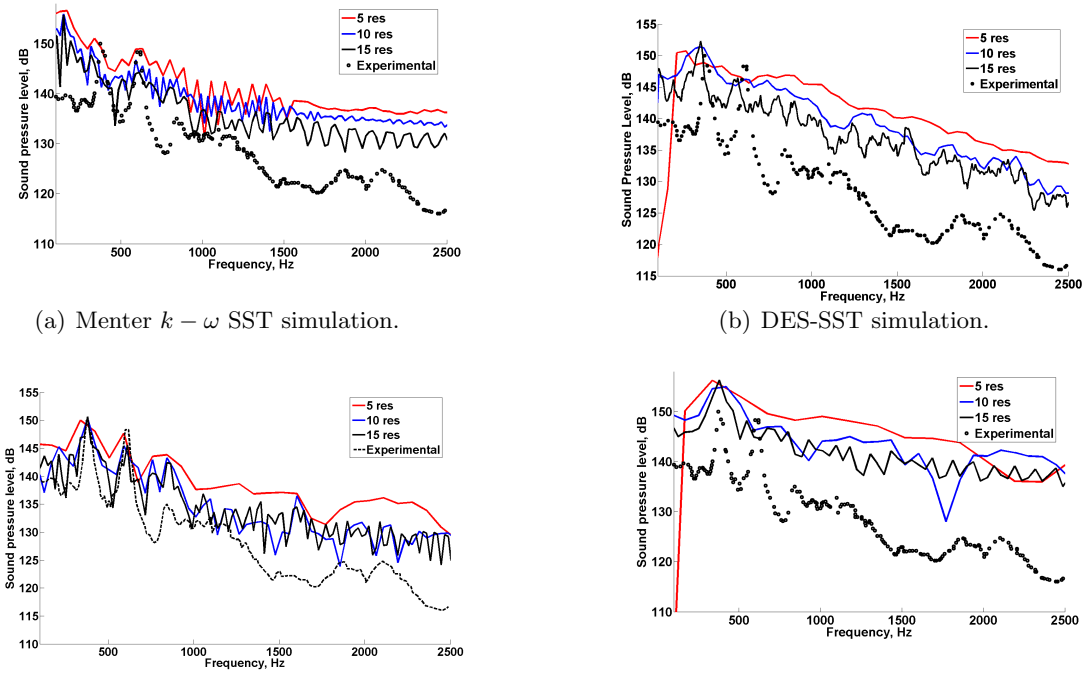

(a) Menter $k-\omega$ SST simulation.

(b) DES-SST simulation.

(c) GT-HRLES simulation.

(d) KES simulation.

Figure 61: Sound pressure levels for cavity pressure data.

results are also shown for comparison. The longest analysis time period yields errors of less than about 10% of the mean (within the 12% error bound) for the harmonic frequencies and amplitudes. The RANS method performs as well as the hybrid methods in determining the frequencies and amplitudes of the harmonics though the high mean pressures and sound levels at low frequencies provide evidence of its predictive limitations. The DES-SST and GT-HRLES methods predict harmonic modes are more distinct than those predicted by the KES approach, as one would expect from the differences in the vorticity observed (Fig. 7.6), but the DES-SST predictions have larger relative errors in the peak location and amplitudes than the GT-HRLES predictions. The LES simulations [1, 18] outperform all other methods in overall terms of relative error, as expected.

7.8 Node Distribution

If hybrid turbulence methodology is applied utilizing a RANS-like approach with the goal of improving flow reproduction, solution dependency on grid node distribution should be addressed. The previous results obtained using the RANS-like grid with larger spacing

Table 10: Predicted cavity modal frequencies for different turbulence methods and analysis intervals.

Method	Interval res	Mode 2 Hz	Error %	Mode 3 Hz	Error %	Mode 4 Hz	Error %
$k-\omega$ SST	5.81	338	-4.4	632	6.4	800	-1.6
	11.70	317	-10.3	591	-0.6	800	-1.6
	17.36	317	-10.3	614	3.2	800	-1.6
DES-SST	5.81	250	-29.3	-	-	715	-12.1
	11.70	325	-7.8	615	3.6	818	0.6
	17.36	332	-5.9	552	-7.1	778	-4.3
GT-HRLES	5.81	337	-4.5	590	-0.7	843	3.7
	11.70	379	7.4	590	-0.7	843	3.7
	17.36	379	7.4	611	2.9	843	3.7
KES	5.81	506	39.6	-	-	1012	20.7
	11.70	422	16.5	759	19.7	1181	40.9
	17.36	338	-7.8	549	-5.4	929	10.8
Rossiter [87]	-	357	1.3	566	4.7	775	4.7
LES Simulations [18] (Mesh 3)	-	362	2.5	594	0.0	838	3.1
Experiment [1]	-	353±12	-	594±12	-	813±12	-

Table 11: Predicted cavity modal amplitudes for different turbulence methods and analysis intervals.

Method	Interval res	Mode 2 dB	Error %	Mode 3 dB	Error %	Mode 4 dB	Error %
$k-\omega$ SST	5.81	151	0.6	149	0.7	147	8.6
	11.70	149	-0.5	147	-0.9	143	5.8
	17.36	148	-1.7	144	-2.6	141	4.6
DES-SST	5.81	150	0.5	-	-	147	8.8
	11.70	151	0.9	146	-1.4	145	7.3
	17.36	152	1.4	146	-1.5	143	6.1
GT-HRLES	5.81	150	0.0	148	-0.3	144	6.5
	11.70	150	0.1	145	-1.9	143	6.0
	17.36	151	0.3	145	-1.7	142	5.4
KES	5.81	153	2.1	-	-	149	10.4
	11.70	155	3.3	147	-0.7	145	7.4
	17.36	153	2.1	147	-0.7	144	7.0
Experiment [1]	-	150	-	148	-	135	-

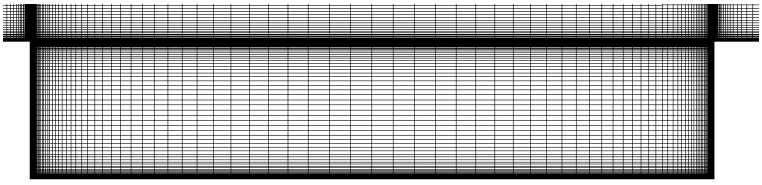

(a) RANS-like grid node distribution.

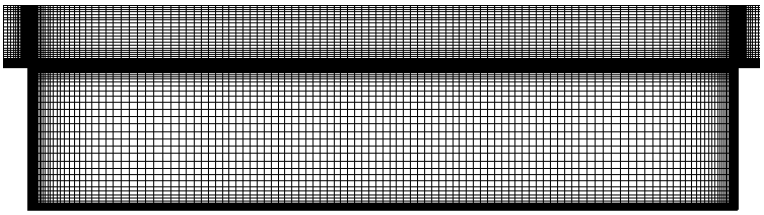

(b) LES-like grid node distribution.

Figure 62: Differing node distributions for grid dependency analysis.

Table 12: Peak mode frequency error for differing node distributions.

Mode	RANS-like Error %	LES-like Error %
2	2.6	-3.9
3	0.2	-0.4
4	1.8	-4.6

across the center of the cavity are compared to results using a grid with more node clustering in the center of the cavity that could be employed with an LES code (Fig. 7.8). The only difference between the two simulations shall be the grid node distribution. With both grids the GT-HRLES approach is used with the same discretization and integration parameters. Pressure is taken again at the same cavity floor location and estimation of the frequency spectrum is carried out with FFT. The results of the spectral analysis (Fig. 63) give minimal qualitative difference between the differing node distributions. Quantitatively, a comparison of the mode predictions (Tables 12 and 13) provides evidence that the frequencies predicted by each method fall within the analysis error of each other, providing evidence of the validity of the RANS-like grid approach. All mode frequency predictions fall within the error bounds of the experiment with the exception of mode 4 for the LES-like grid results.

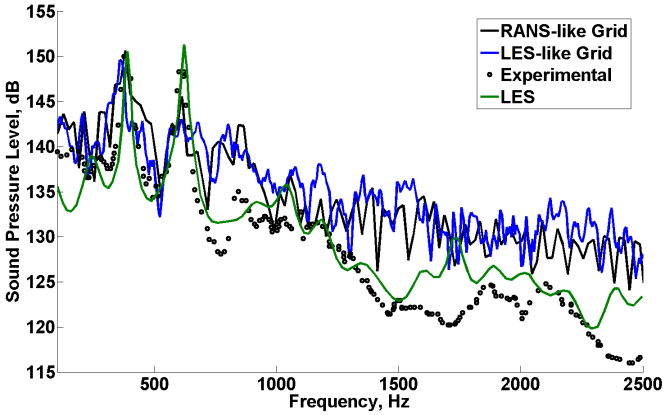

Figure 63: Sound pressure levels at the cavity floor center using differing node distributions.

Table 13: Peak mode amplitude error for differing node distributions.

Mode	RANS-like Error %	LES-like Error %
2	0.4	-0.4
3	-1.9	-3.7
4	5.4	5.4

7.9 Method Comparison

As a final evaluation, the 0.5 s period DES-SST and GT-HRLES results are compared to the results obtained by LES [18] and experiments by Henshaw [1]. The sound pressure levels for these simulations (Fig. 64) are presented up to frequencies of 2500 Hz (Fig. 65). The DES-SST method predicts additional modes between 100–400 Hz, which are not present in experiment. The GT-HRLES turbulence method simulation captures overall more accurate SPL characteristics below 700 Hz than the DES-SST approach and is comparable to the LES predictions. The major characteristics of the mode at 350 Hz are captured by the LES and GT-HRLES simulations. The DES-SST approach captures this peak, but the frequency is shifted. The third mode is best captured by the LES method, with the GT-HRLES method providing the next best predictions. The DES-SST result for the third mode is the most inaccurate correlation. As discussed previously, the grids for the DES-SST GT-HRLES simulations were not optimized for higher frequency content and contained some aspect ratios that may result in poorer resolution of the acoustics above 700 Hz.

Table 14: Grid comparisons for small and large grid domains.

Grid	Stream-wise	Span-wise	Height	Computational Size cells
Current Study	20D	6D	10D	8.9×10^6
LES [18]	20D	6D	10D	9×10^6

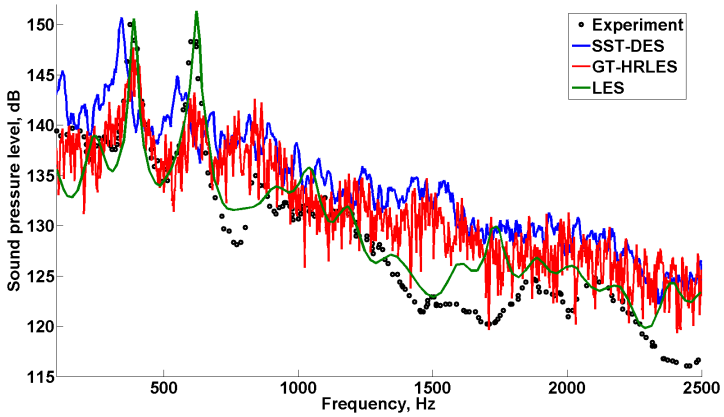

Figure 64: Sound pressure levels at the cavity floor center for different turbulence methods.

With respect to the captured modal frequencies (Table 15), GT-HRLES computation at the longer simulation time/larger time step combination predicts the frequencies with accuracy comparable to the LES simulation for the second and third modes, and is comparable to the other hybrid methods for mode four. For the modal peak sound pressure levels (Table 16), the GT-HRLES and DES-SST predictions for modes two and three are comparable to LES, but mode four DES-SST and GT-HRLES levels are not as accurate as the LES results. Limited computer resources prevented examination of a longer time interval to determine if this could have lowered the higher mode amplitudes. As expected, the LES method has the best performance overall. The GT-HRLES approach is the next most accurate after LES.

Table 15: Comparison of cavity modal frequencies.

Method	Mode 2 Hz	Error %	Mode 3 Hz	Error %	Mode 4 Hz	Error %
DES-SST	323	-8.4	538	-9.4	790	-2.9
GT-HRLES	354	0.3	596	0.3	837	3.0
LES [18], Mesh 3	362	2.5	594	0.0	813	0.0
Experiment [1]	353±12	-	594±12	-	813±12	-

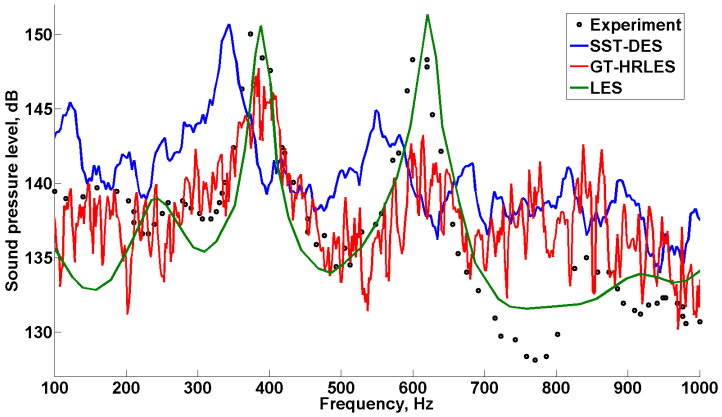

Figure 65: Sound pressure levels at the cavity floor center for different turbulence methods.

Table 16: Comparison of cavity modal peak sound pressure levels.

Method	Mode 2 dB	Error %	Mode 3 dB	Error %	Mode 4 dB	Error %
DES-SST	151	0.4	144	-2.4	141	4.5
GT-HRLES	149	-0.6	145	- 2.1	144	6.7
LES[a] [18] (Mesh 3)	150	0.3	151	2.2	134	-1.0
Experiment [1]	150	-	148	-	135	-

[a] These data were not explicitly given by Levasseur [18]. These quantities have been determined by digitization of the SPL data presented in Fig. 64.

7.10 Cost

Some final consideration of cost is appropriate. The hybrid turbulence techniques employed in this study aim to improve predictions of cavity flows without drastically increasing the cost of the simulations. The DES-SST, GT-HRLES, and KES techniques result in an increase in cost relative to the traditional RANS approach of 2.1%, 16%, and 0.9%, respectively. No timing information was available for the comparable LES study, so quantitative comparisons are not possible, but qualitative assessments may be made. If timing data from recent LES simulations by Tucker [45] employing structured grids in an LES framework are considered, full LES simulation with appropriate temporal parameters would increase the cost by two orders of magnitude. The advanced turbulence methods outlined in this study provide a much higher turnover rate for modestly decreased accuracy.

CHAPTER VIII

FLAPPED OSCILLATING AIRFOILS

8.1 Purpose

The understanding of static stall is of paramount importance as it is a phenomenon that may lead to drop in lift, high drag, and large moments, creating useless or even detrimental flow conditions. Dynamic stall adds yet another layer of complexity on the physics of the flow, with leading edge vortex shedding dominating the flow at higher angles of attack. The response of the flow will change in a nonlinear manner as the angle of attack or reduced frequency of oscillation is altered. Static and dynamic stall are both characterized by strong vortex shedding that may greatly increase noise levels. The addition of airfoil flaps, which may be necessary to reduce stall speed and counter dynamic stall affects, creates a cavity-like flow between the airfoil and flap. Vorticity and acoustics resulting from the complex flowfield are an additional concern due to vibration and fatigue. Analysis of each of these aspects of the physics will help alleviate the effects of dynamic stall.

8.2 Experimental Correlation

Krzysiak et al. [31] investigated an oscillating NACA 0012 airfoil with an oscillating trailing edge flap. The resulting data were used as an assessment of the ability of the approach in this study to predict the aerodynamic response of a multi-element dynamic system. The airfoil had a total chord including the airfoil and flap of 0.18 m and a span of 0.6 m. It was mounted in a wind tunnel with a cross-sectional test section of 0.6 m by 0.6 m and a length of 1.58 m. The length of the airfoil flap was 0.04069 m, and it had a leading edge radius of 0.00469 m. The minimum distance or gap between the flap and the airfoil was 0.0005 m. The axes of rotation of the airfoil and flap were at 35% and 80% of the total airfoil plus flap (0.18 m) chord, respectively.

The flap was set at a deflection angle of 0° for the static analysis. Computations were performed at a Reynolds number of 1.99 million and Mach number of 0.5. Computational

results were compared with experimental data at Reynolds numbers of 1.99 million from the Institute of Aviation (IoA) [94], 1.93 million from the Aeronautical Research and Tests Institutes (VZLU) [95], and 17.6 million from the National Aeronautical Establishment (NAE) [96].

The Mach number for the dynamic tests was 0.4 with a Reynolds number of 1.63 million. The dynamic stall data were obtained with the primary airfoil oscillating sinusoidally at 5 Hz and the flap at 10 Hz. Two oscillating cases were evaluated and are described in Table 17. For both cases, oscillation amplitudes for the airfoil and flap were 6° and 5.4°, respectively. The main airfoil oscillated at 5 Hz, while the flap oscillated at 10 Hz. Due to some differences in the actual experiment to the nominal motion, the airfoil pitch and flap deflection motions from Krzysiak et al. [31] were digitized and interpolated to provide the forcing functions in the computational analysis.

8.3 Computational Setup

8.3.1 NACA 0012 Airfoil

The computational analyses were performed using the NASA-developed Overflow 2.1z code [67]. Time-accurate simulations using a hybrid unsteady Reynolds-averaged Navier-Stokes/large eddy simulation (HRLES) [29] model were performed. A time step of 1.32×10^{-6} seconds with an ARC3D diagonalized Beam-Warming scalar pentadiagonal scheme and 2^{nd}-order accurate Newton subiterations provided the temporal integration. A 4^{th}-order spatial discretization formulation was employed with central difference Euler terms. Numerical stability was ensured via the 2^{nd} and 4^{th}-order ρh_0 discretization terms in the form of dissipation coefficients. The coefficients are 2.0 and 0.04 for these discretization terms, respectively.

For the overset approach, 3 fringing points were utilized for interpolation between grids to conform to the higher spatial accuracy. X-rays cut the grids at a distance of 0.002 airfoil chords from the airfoil surface and 0.002 flap chords from the flap surface. The dynamic stall simulations parallel the static stall simulation methodology. The only difference was in the rotation of the airfoil and flap about their respective axes of rotation with each time

Table 17: Dynamic flapped airfoil setup.

Parameter	Case 1	Case 2
Mean Angle of Attack, °	4	10
Initial Flap Deflection, °	4.769	-0.286
Flap Oscillation Lag, °	298	177

step. Therefore, the X-rays cut holes in the grids at every iteration, rather than only once at the beginning of the simulation.

8.3.2 VR7 Airfoil

Overflow 2.1z [67], an overset structured solver, was employed to assess the flow about the airfoil-flap configuration. The predictions were run using 2^{nd}-order temporal accuracy and 4^{th}-order spatial accuracy. Temporal integration was achieved via an ARC3D diagonalized Beam-Warming scalar pentadiagonal scheme, while spatial discretization was achieved via a central difference Euler scheme with numerical dissipation added to the 2^{nd} and 4^{th}-order ρh_0 discretization terms. The dissipation coefficients for these terms were 2.0 and 0.04, respectively.

The HRLES [29] turbulence technique was used with a solution time step of 1.32×10^{-6} seconds. Solution convergence was confirmed in accordance with methodologies developed in the previous convergence chapter. The overset approach required X-rays to cut portions of the various grids that overlapped the geometry. The overlapping nodes were cut 0.002 airfoil chords away from the airfoil surface and 0.002 flap chords away from the flap surface, respectively. Higher order spatial accuracy necessitated interpolation of conserved variables between neighboring grids with three fringe points.

In this study, a variety of flap oscillation frequencies, angles of attack, free stream speeds, and gap sizes were parametrically varied (Table 18) to determine their effects on the behavior of the wing section. The parameters were chosen to reproduce conditions similar to a one-sixth CH-47 rotor blade. This scale is similar to the scale of comparable investigations of flapped airfoils and rotors [31, 35, 97]. The flap chord is 25% of the total chord, which matches the effective flap chord of the Boeing SMART active rotor [35]. The nominal flap gap is 0.7% of the chord, which also matches the Boeing SMART rotor. For each test case,

Table 18: Cases for flapped VR7 airfoil analysis.

Case Number	Reynolds Number per chord	Mach Number	Angle of Attack (deg)	Flap Reduced Frequency	Gap Size (mm)
1	1.51×10^6	0.475	10.5	0.118	0.035
2	1.51×10^6	0.475	10.5	0.237	0.035
3	1.51×10^6	0.475	10.5	0.355	0.035
4	1.51×10^6	0.475	18.5	0.118	0.035
5	1.02×10^6	0.320	10.5	0.237	0.035
6	1.51×10^6	0.475	10.5	0.118	0.070
7	1.51×10^6	0.475	10.5	0.118	0.105
8	1.51×10^6	0.475	18.5	0.118	0.070
9	1.51×10^6	0.475	18.5	0.118	0.105

the flap was oscillated sinusoidally between $\pm3.88^\circ$ to provide an assessment of the unsteady behavior. This deflection is also in the mid-range of similar investigations [31, 35, 97]. First, the influence of the flap reduced frequency of oscillation was established (cases 1–3). These reduced frequencies correspond to possible 2, 4, and 6 per rev flap oscillation frequencies for the existing rotor blade experiment. Variable free stream speeds (cases 2 and 5) were also evaluated. Gap size sensitivity for attached flows (cases 1, 6, and 7) and separated flows (cases 4, 8, and 9)) were investigated where the gap size was varied as integer multiples (1X, 2X, 3X) of the baseline gap size of 0.035 mm.

8.4 Grids

The best practices obtained from the efforts of earlier chapters along with other studies [30] were applied here to ensure sufficient grid fidelity for the simulations.

8.4.1 NACA 0012 Airfoil

The flapped NACA 0012 airfoil is 180.00 mm long with a 40.69 mm flap (Fig .66). The size of the gap at the minimum is 0.5 mm, and the radius of the flap leading edge is 4.69 mm. The overset grid system consisted of four grids to model the moving components and the wind tunnel test section (Fig. 67). The wind tunnel grid has 173 grid points in the vertical direction and 286 grid points in the stream-wise direction. Grid points were clustered in the region of the tunnel surrounding the airfoil. The flapped airfoil (Fig. 68) is split into

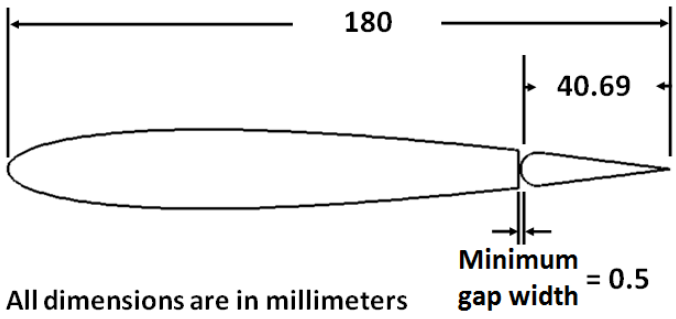

Figure 66: Dimensions of the flapped NACA 0012 airfoil.

three separate grids: an airfoil O-grid (Fig. 69) for the portion from the leading edge up to the flap gap, a C-grid for the flap (Fig. 70), and a patch grid to allow interpolation across the C-grid boundary. The airfoil O-grid had 200 grid points in the normal direction and 374 grid points around the circumference. The C-grid included 200 grid points in the normal direction and 400 points in the C-direction with 250 grid points along the flap and the remaining 150 grid points in the wake. The C-grid was smoothed to reduce the tight viscous spacing in the region downstream within the wake. The patch grid fitted 11 grid points in the vertical direction across the gap and 75 grid points in the stream-wise direction. The viscous grid spacing at the airfoil and flap surfaces was $y^+ < 1.0$ for the Reynolds number range here with at least $30 - 50$ points in the boundary layer, as identified by previous studies [30, 53]. The airfoil and flap surfaces are treated as fully viscous with the pressure extrapolated to the surfaces. The wind tunnel walls are treated as inviscid walls with the inlet and outlet treated with subsonic characteristic boundary conditions.

The HRLES cases required three-dimensional grids of a semi-infinite wing to accurately capture the turbulent behavior. The resolution and length of the mesh along the span was based on previous high stall and reverse flow predictions [30]. The three-dimensional separated flow features were modeled with a span of two chords and a spanwise mesh resolution of 30 nodes per chord. Interrogation of the flow and data from the mid-line of the solutions provided results that are free of boundary condition contamination.

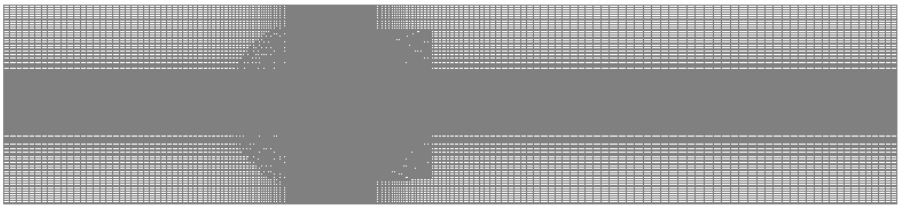

Figure 67: Overall view of the NACA 0012 flapped airfoil grid including wind tunnel walls.

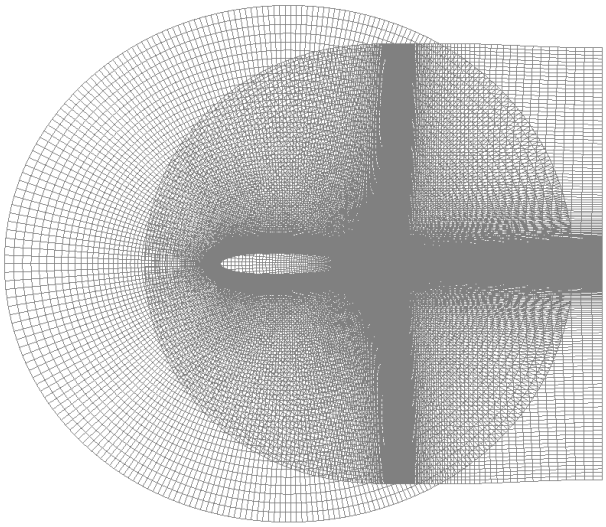

Figure 68: NACA 0012 airfoil and flap grid with patch grid across wake.

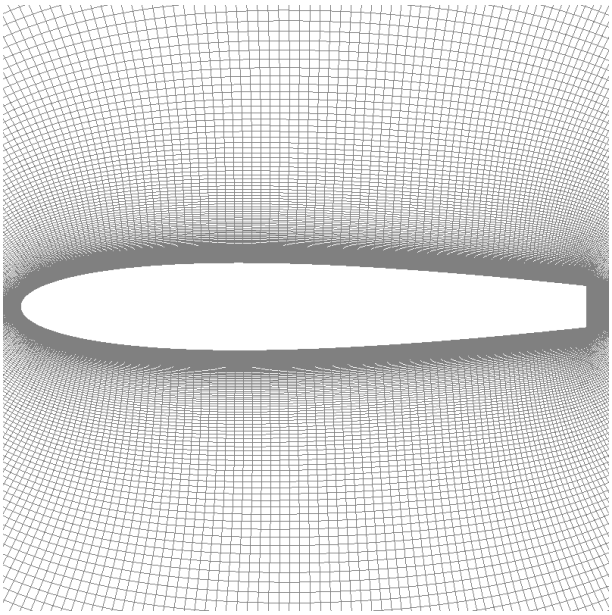

Figure 69: NACA 0012 airfoil O-grid.

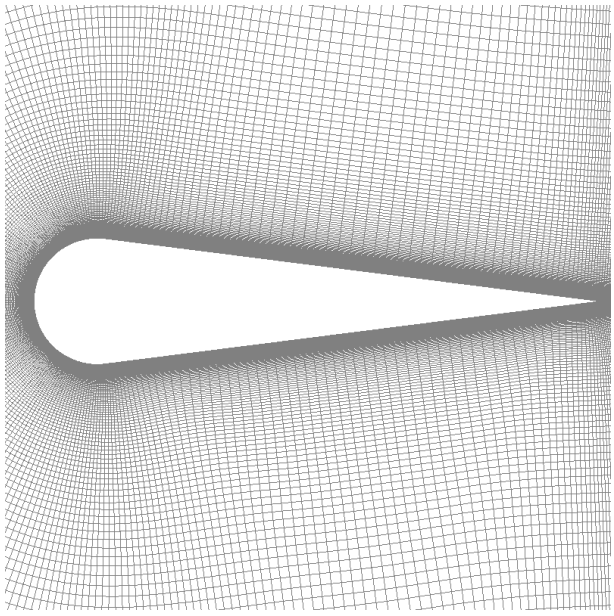

Figure 70: NACA 0012 flap C-grid.

8.4.2 Flapped VR7 Airfoil

The flapped VR7 airfoil has a total chord of 5.388 inches (Fig. 71). The final 1.345 in. is the flap chord, and the minimum gap between the airfoil and flap is 0.035 inches. The predictions were carried out using a three-dimensional grid that consisted of an O-grid topology for the main airfoil body, C-grid for the flap, and patch grid for passing boundary information across the C-grid seam (Fig. 72). The O-grid had 476 nodes around the circumference of the airfoil and 180 nodes in the normal direction extending 10 chords away from the surface of the airfoil. The C-grid had 518 nodes in the stream-wise direction (354 nodes cover the viscous surface of the flap; 82 nodes extend into the downstream flow for the wake), and 100 nodes in the normal direction. The patch grid started at the trailing edge of the flap and extended 82 nodes into the downstream flow and matched the node distribution of the flap grid. The patch grid had 11 nodes in the vertical direction. The radial direction is a semi-infinite wing of dimension 2 chords (11.776 inches) with 61 nodes (30 nodes/chord) distributed equally across the width. This resolution was shown to accurately capture the turbulent features for high stall and reverse flow predictions [30].

The semi-infinite airfoil and flap surfaces were treated as fully viscous with the pressure

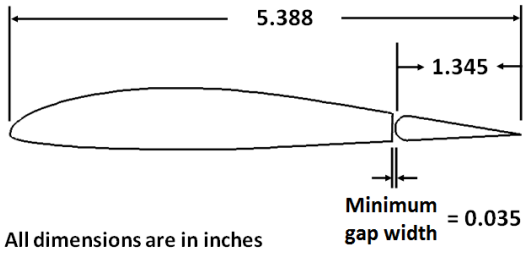

Figure 71: Dimensions for the flapped VR7 airfoil section.

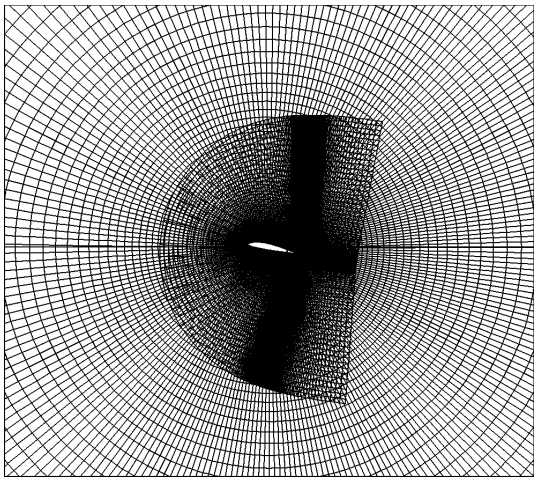

Figure 72: Three-dimensional grid system for the flapped VR7 airfoil study.

extrapolated to the surface. The viscous grid spacing at the airfoil and flap surfaces had a $y^+ < 1.0$ for the Reynolds number range applied here with at least 30 – 50 points in the boundary layer, which is necessary for proper resolution as identified by previous studies [30, 53]. The farfield was treated with Riemann invariant boundary conditions, and the initial conditions for the solution were uniform flow. Interrogation of the flow and data at the mid-span location of the wing provide sectional data that includes the three-dimensionality of the turbulent flow. Once the initial transients in the flow subsided, multiple cycles of the data were averaged to provide the mean behavior of the airfoil at each location during the oscillation.

8.5 Results for NACA 0012 Airfoil

These NACA 0012 airfoil results may also be found in a publication by Liggett and Smith [98].

8.5.1 Static Response

Variation of the static integrated coefficients with angle of attack are compared with experimental observations (Fig. 73). Static stall location and magnitude are within the limits of experimental error bounds. The effect of including the wind tunnel walls is an increase in magnitude in the lift, drag, and moment coefficients from their respective free air values. The effect is present for predictions both with and without the flap, and is stronger at higher angles of attack. These increases are caused by blockage of the wind tunnel area by the airfoil body. To maintain mass flow rate, the fluid accelerates through the reduced wind tunnel cross-sectional area. This acceleration leads to lower pressures on the upper surface, a higher suction peak than would be experienced in free air, and increases in the magnitudes of the wind tunnel coefficients. This blockage effect is one of the reasons why wind tunnel corrections are necessary.

The addition of the flap has little effect at angles of attack below stall. The flow is attached; therefore, any fluid traveling through the gap is entrained into the boundary layer, minimizing its influence in the linear regime. Once the flow separates, the impact of the gap becomes significant as indicated by increases in the lift and drag. The gap is more directly exposed to the flow at higher angles of attack, and a strong pressure difference exists across the upper and lower surfaces through the gap. This pressure difference leads to suction that enhances both lift and drag.

8.5.2 Dynamic Stall (mean $\alpha = 4°$)

Dynamic stall of the NACA 0012 airfoil-flap configuration was subsequently analyzed. The integrated lift and moment coefficients are compared with experimental data (Fig. 74); however no experimental drag data were available. The combined motion of the airfoil and flap exactly matched the experiment (Fig. 74(d)). The lift coefficients differ between experiment and the predictions by at most $\Delta C_L = 0.05(7\%)$, while the moment coefficients differ by at most $\Delta C_M = 0.015(13\%)$ over the dynamic angle of attack range. For this case, no stall occurs.

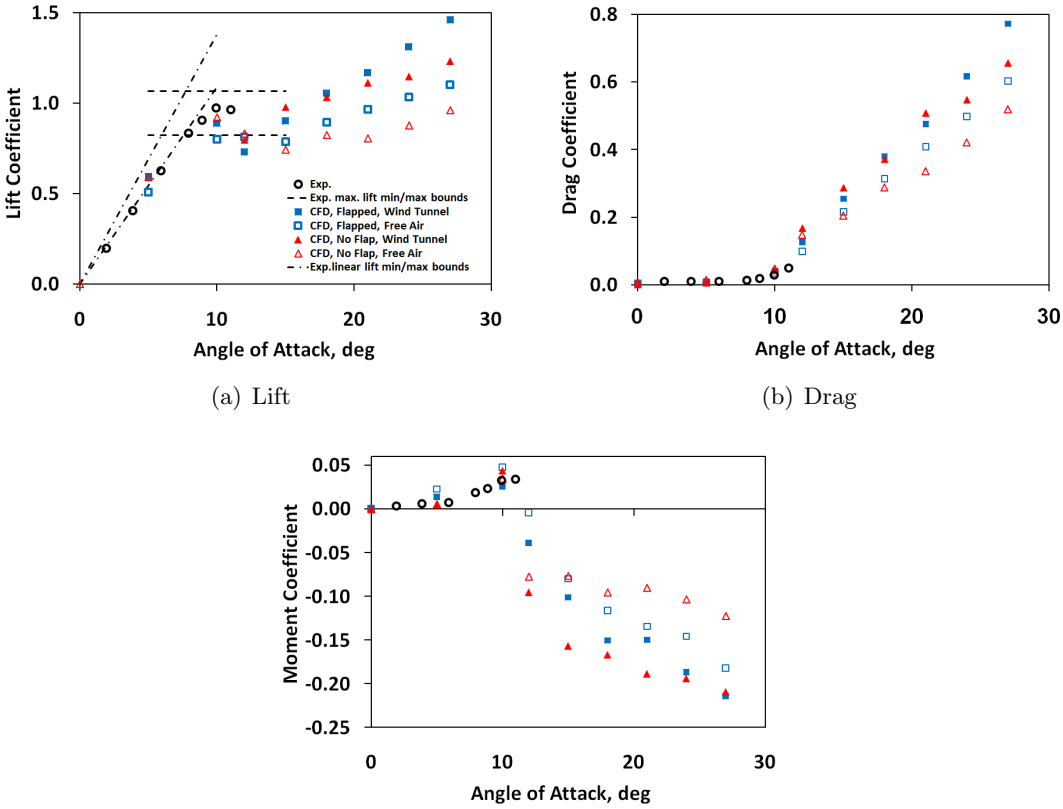

(a) Lift

(b) Drag

(c) Moment

Figure 73: NACA 0012 airfoil integrated coefficient variation with angle of attack, $M_\infty = 0.5$, $Re_\infty = 1.99$ million.

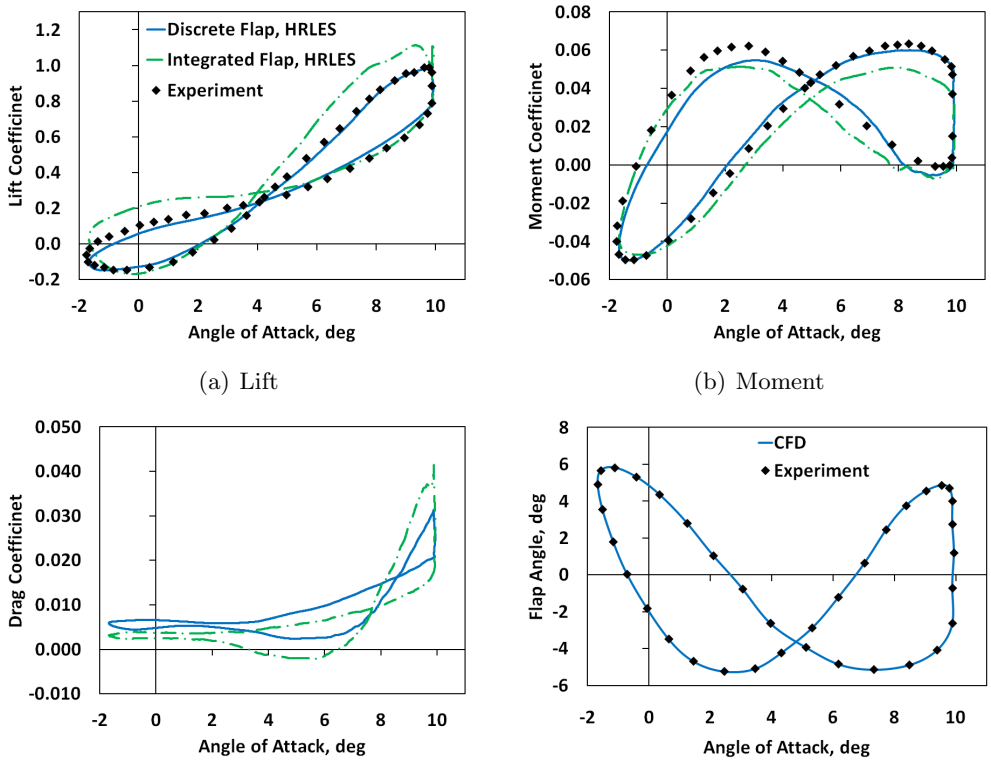

(a) Lift

(b) Moment

(c) Drag

(d) Motion

Figure 74: NACA 0012 airfoil integrated coefficient response and input motion with $\alpha_{mean} = 4°$ and $\phi = 148°$, $M_\infty = 0.4$, $Re_\infty = 1.63$ million, $k_{airfoil} = 0.021$, $k_{flap} = 0.042$.

8.5.2.1 Flow Field

At the beginning of the cycle at 3.96° during the upstroke, the flow is fully attached to the airfoil (Fig. 77(a)). Vorticity in the upper half of the gap (Fig. 75(a)) and a detached shear layer in the lower half of the gap (Fig. 76(a)) are associated with flow downward through the gap. The roll-up and shear layer instability observed in prior studies [17, 19, 20] is not present here. This may be due to the shorter distance the detached shear layer travels before impinging on the leading edge of the flap. In prior results, the shear layer begins to roll-up after a distance of 10 mm, while in this configuration there exists a maximum of a 5-7 mm gap, which may be an insufficient distance for a shear layer instability to develop. There may also be some secondary Reynolds number effects associated with the growth of the shear layer instability as the Reynolds number in Krzysiak's tests is 4.4 times smaller than the prior efforts.

At low angles of attack, upward deflection of the flap trailing edge relative to the airfoil results in flow downward through the gap. The negative deflection of the flap and downward flow through gap are associated with decreased lift efficiency as observed in the integrated coefficients (Fig. 74(a)). The flap deflection appears to exert a stronger influence than the airfoil motion, which may be due to the low reduced frequency ($k = 0.021$). During the upstroke, the flow begins to reverse direction through the gap as the flap deflection crosses chord axis of the airfoil (i.e., as the flap cross zero deflection relative to the airfoil). This occurs during the downstroke as well. Despite the fact that the airfoil maintains the direction of the pitching rate, the reversal of the flap direction also reverses the flow through the gap. For this case, there are four times per cycle the flap crosses the zero deflection axis, and each time is accompanied by initiation of the reversal of the flow direction through the gap. This behavior is not observed at the higher angles of attack for the deep stall case for $\alpha > 10$, which is evaluated in the next section.

As the angle of attack increases to $\alpha = 6.62°$, the flap has increased negative deflection relative to the airfoil. Stronger suction across the gap occurs (Fig. 78(b)) and downward flow through the gap is enhanced. This is evident through strong rotation of flow into the gap (75(b)) and increased vorticity in the lower half of the gap (Fig. 76(b)). The flow

remains attached to the airfoil and flap throughout this angle of attack range (Fig. 77(a)).

Near the peak angle of attack during the upstroke, the flow downward into the gap weakens (Fig. 75(c)). The strength of the vorticity in the upper half of the gap has considerably weakened (Fig. 75(c)). The detached shear layer in the lower half of the gap begins to move upward into the gap (Fig. 76(c)). The flap is still at a negative deflection relative to the airfoil, but it is very near zero and will begin positive deflection momentarily. The lift efficiency is also beginning to increase at the maximum angle of attack (Fig. 74(a)).

Near the maximum angle of attack on the downstroke, the flap is deflected downward (i.e., positive deflection) relative to the airfoil. The high angle of attack combined with the positive flap deflection results in a strong pressure gradient across the gap that pulls flow upward through the gap (78(d)). The lift coefficient rises at this point (74(a)) as the efficiency increases. The flow near the trailing edge is much slower (77(d)), but full boundary layer reversal on the flap never occurs.

The relationship of the flap deflection, flow through the gap, and lift efficiency repeats for the remainder of the oscillation cycle. The direction of flow through the gap at these low angle of attack is governed by the deflection of the flap relative to the airfoil: negative flap deflection relative to the airfoil is associated with flow downward through the gap, while positive flap deflection relative to the airfoil is associated with flow upward through the gap. Flow downward through the gap/negative flap deflection is associated with lower lift efficiency, while flow upward through the gap/positive flap deflection is associated with higher lift efficiency. Gap flow reversal is correlated with several points on the integrated coefficient curves: crossover near the mean angle of attack, reversal in efficiency at the maximum angle of attack, and reversal in efficiency at the minimum angle of attack.

Separation and flow reversal as a function of the angle of attack, flap deflection angle, and total inclination angle (Fig. 79) were extracted from skin friction data. The total inclination angle is the sum of the flap deflection angle and the angle of attack. No separation or flow reversal was exhibited on the surface of the airfoil, whereas up to 70% the upper surface of the flap experienced flow reversal. As a function of angle of attack (Fig. 79(a)) the separation point moves upstream on the flap from the trailing edge to a value of $x/c = 0.84$

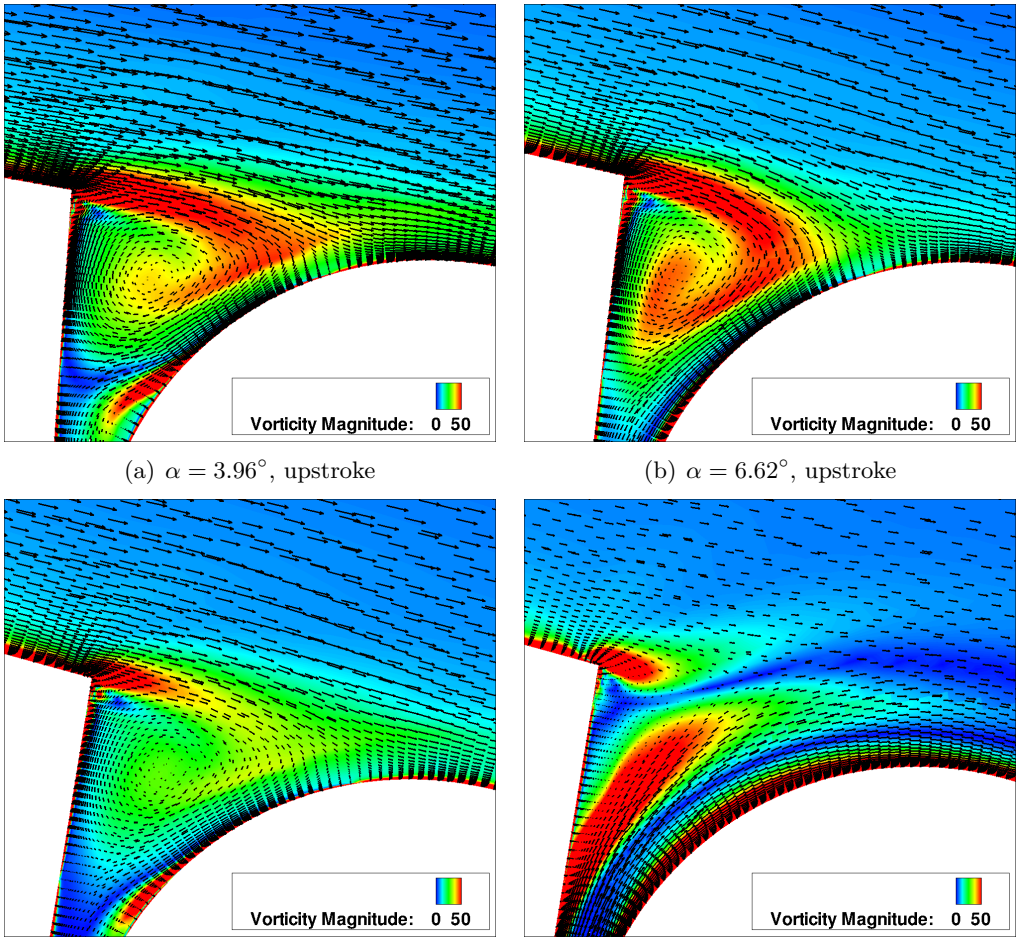

(a) $\alpha = 3.96^\circ$, upstroke

(b) $\alpha = 6.62^\circ$, upstroke

(c) $\alpha = 9.23^\circ$, upstroke

(d) $\alpha = 9.26^\circ$, downstroke

Figure 75: Physics of the upper portion of the NACA 0012 airfoil-flap gap for dynamic oscillations of $\alpha_{mean} = 4^\circ$ and $\phi = 148^\circ$ during the main airfoil upstroke, $M_\infty = 0.4$, $Re_\infty = 1.63$ million, $k_{airfoil} = 0.021$, $k_{flap} = 0.042$ applying constant contour levels at all locations.

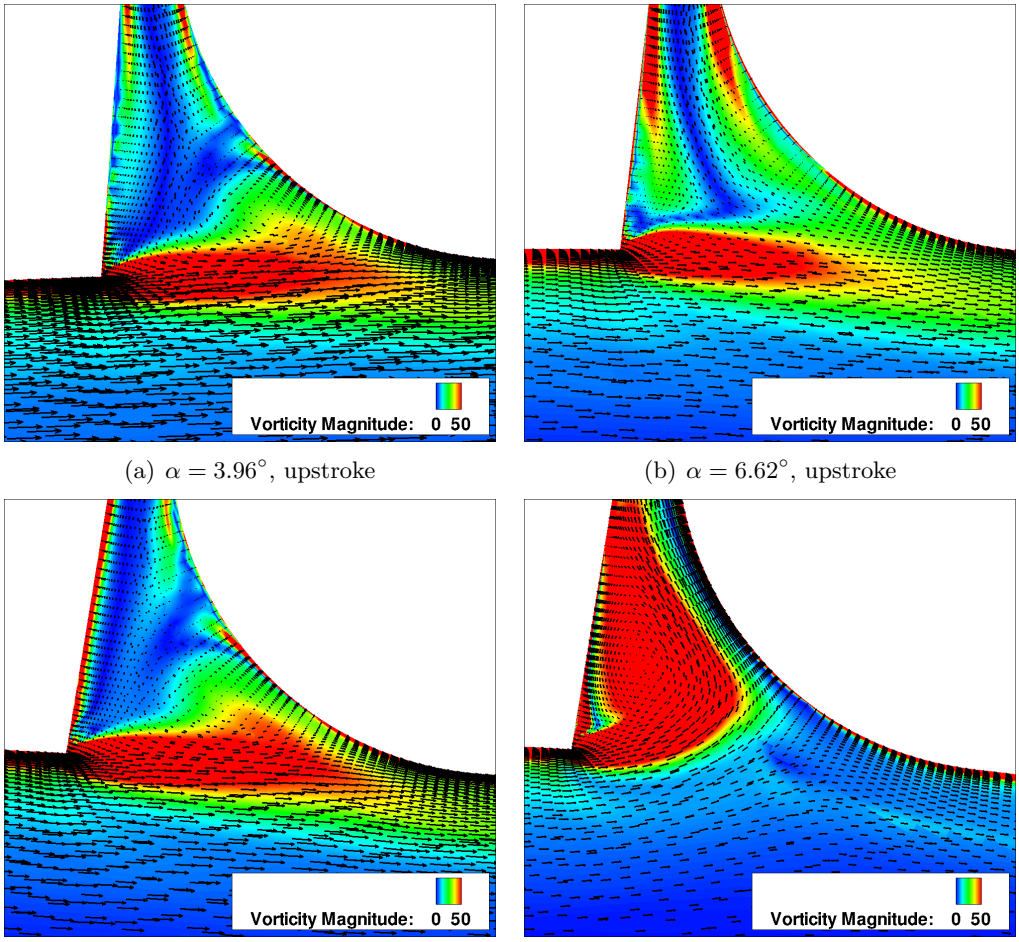

(a) $\alpha = 3.96^{\circ}$, upstroke

(b) $\alpha = 6.62^{\circ}$, upstroke

(c) $\alpha = 9.23^{\circ}$, upstroke

(d) $\alpha = 9.26^{\circ}$, downstroke

Figure 76: Physics of the lower portion of the NACA 0012 airfoil-flap gap for dynamic oscillations of $\alpha_{mean} = 4^{\circ}$ and $\phi = 148^{\circ}$ during the main airfoil upstroke, $M_{\infty} = 0.4$, $Re_{\infty} = 1.63$ million, $k_{airfoil} = 0.021$, $k_{flap} = 0.042$ applying constant contour levels at all locations.

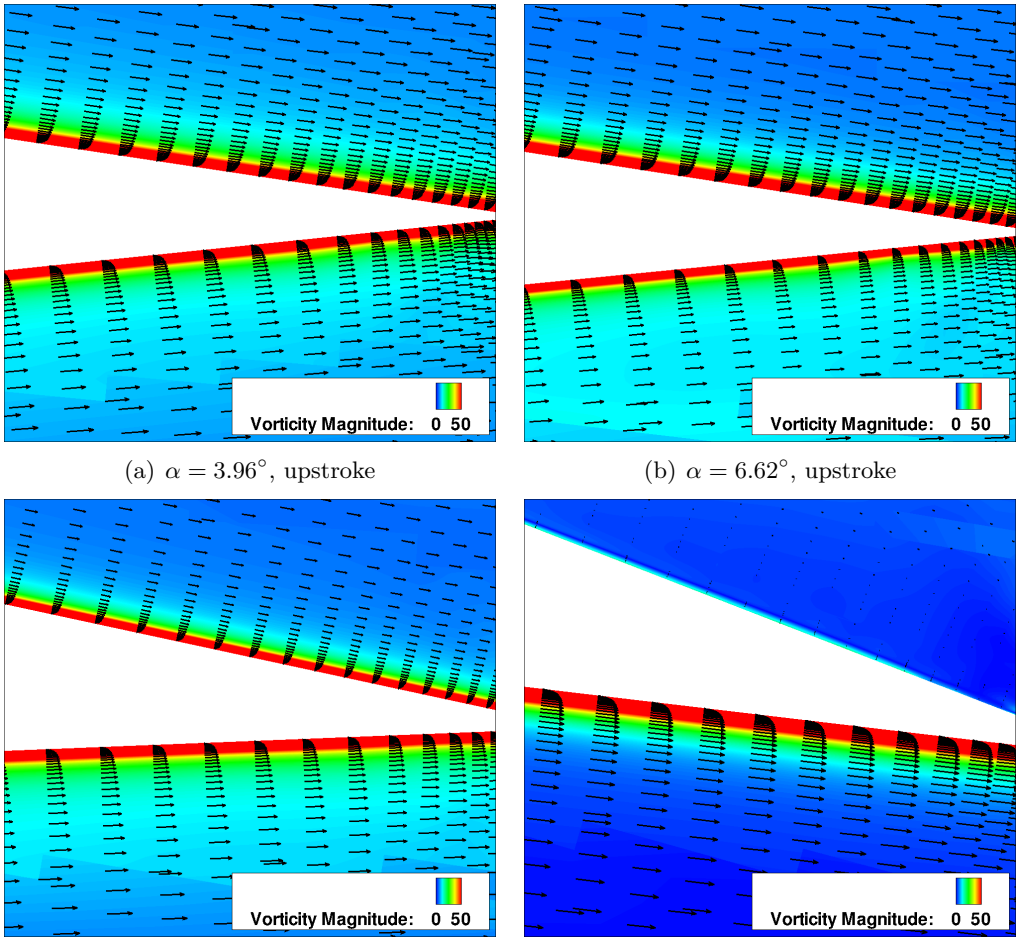

(a) $\alpha = 3.96^\circ$, upstroke

(b) $\alpha = 6.62^\circ$, upstroke

(c) $\alpha = 9.23^\circ$, upstroke

(d) $\alpha = 9.26^\circ$, downstroke

Figure 77: Physics of the trailing edge of the NACA 0012 airfoil-flap gap for dynamic oscillations of $\alpha_{mean} = 4^\circ$ and $\phi = 148^\circ$ during the main airfoil upstroke, $M_\infty = 0.4$, $Re_\infty = 1.63$ million, $k_{airfoil} = 0.021$, $k_{flap} = 0.042$ applying constant contour levels at all locations.

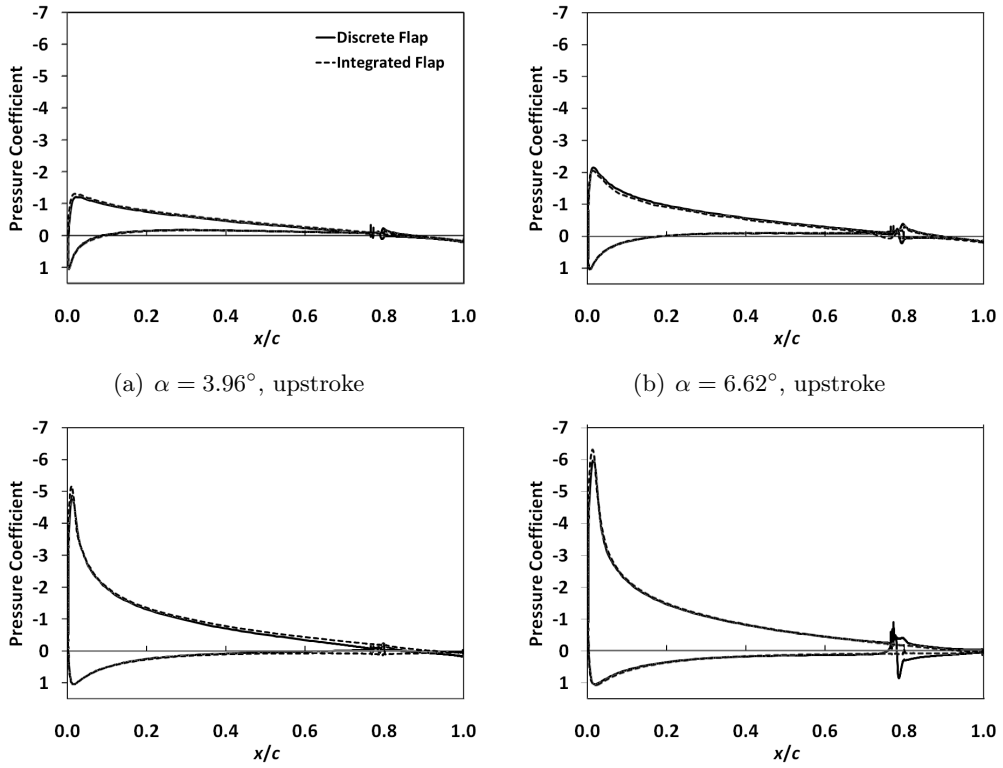

(a) $\alpha = 3.96°$, upstroke

(b) $\alpha = 6.62°$, upstroke

(c) $\alpha = 9.23°$, upstroke

(d) $\alpha = 9.26°$, downstroke

Figure 78: Pressure coefficient distribution of the NACA 0012 airfoil with discrete or integrated flap (discrete flap has gap) for dynamic oscillations of $\alpha_{mean} = 4°$ and $\phi = 148°$ during the main airfoil upstroke, $M_\infty = 0.4$, $Re_\infty = 1.63$ million, $k_{airfoil} = 0.021$, $k_{flap} = 0.042$ applying constant contour levels at all locations.

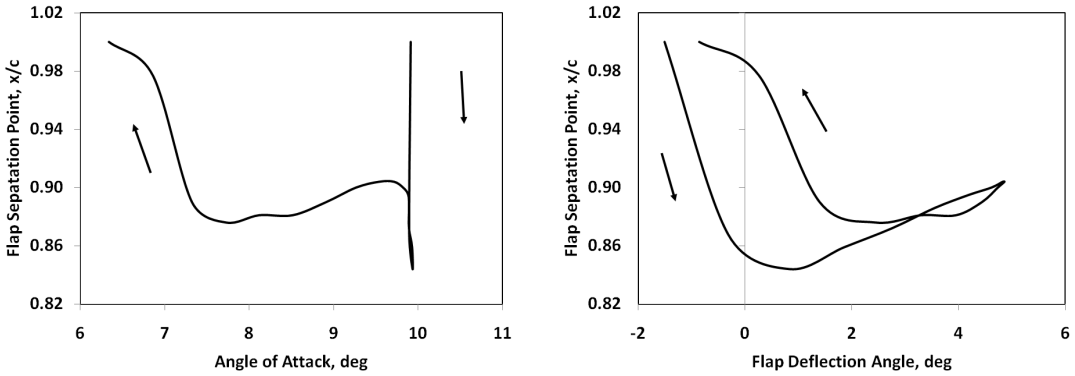

(a) Variation with angle of attack

(b) Variation with flap deflection angle

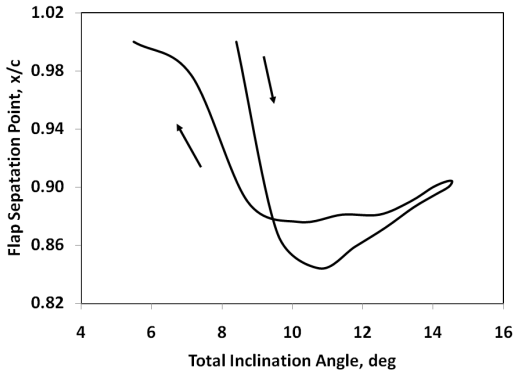

(c) Variation with total flap inclination angle

Figure 79: NACA 0012 flap separation point variation for $\alpha_{mean} = 4°$ and $\phi = 148°$, $M_\infty = 0.4$, $Re_\infty = 1.63$ million, $k_{airfoil} = 0.021$, $k_{flap} = 0.042$.

and settles at a value of $x/c = 0.88$, despite the constant angle of attack.

Examining the flap deflection angle (Fig. 79(b)) reveals that although the angle of attack is constant, the flap deflection angle is increasing. This gives rise to the increasing separation. As the angle of attack begins to decrease, the flap deflection angle is still increasing, which results in a nearly constant separation location. Once the angle of attack reaches $\alpha = 7.4°$ the flap deflection angle begins to decrease resulting in a separation point that moves quickly to the trailing edge and fully attached flow at $\alpha = 6.4°$.

The total inclination angle (Fig. 79(c)) reveals the upstroke acts to suppress separation up to about 9.5°. At higher angles of attack, the upstroke aggravates reversal.

8.5.2.2 Comparison with Integrated Flap

Additional predictions using an identical computational setup were made for an airfoil with an integrated flap. This geometry is identical to the previous discrete flap case, except the airfoil-flap gap is sealed to create a single continuous surface. The resulting lift, drag, and moment hystereis curves for the integrated flap are compared with the discrete flap case with a gap (Fig. 74). The results indicate that the gap is detrimental to the performance of the airfoil. A 33% drop in average lift, 9% increase in average drag, 46% increase in pitching moment occur when discrete flaps are employed, rather than integrated flaps. Although differences in lift are primarily observed on the upper portion of the lift hysteresis, the drag and moment curves differ consistently throughout the predictions; however, the qualitative behavior of the curves is similar. These results are consistent with those of previous authors who observed performance losses in rotorcraft with discrete flaps when compared to those with integral flaps [35].

Flow field vorticity results for both the discrete and integrated flap airfoils were smooth and fully attached. This is not unexpected, as the integrated coefficients of both predictions follow similar smooth trends. No significant difference in vorticity was discernible in the flow surrounding the discrete flap (away from the gap) and the integrated flap airfoils at any angle of attack (Fig. 80). Previous authors observed unsteadiness emanating from the gap [17, 19, 20], but roll-up of vorticity and growth of instabilities is prevented by the relatively small gap size as previously discussed.

When the flap is deflected upward during the upstroke, the pressure coefficient distributions are nearly identical (Figs. 78(a) and 78(b)), resulting in approximately the same value of lift (Fig 74(a)). As the airfoil begins the downstroke, higher lift is observed for the integrated flap airfoil, partially the result of higher suction peaks (Figs. 78(c) and 78(d)). Without flow leakage through the gap, the pressure is reduced on the upper surface of the integrated flap airfoil where the gap would be located. This leads to higher suction and increased lift for the integrated flap airfoil. The higher drag for the discrete flap (Fig. 74(c)) is the result of flow stagnation against the flap leading edge, a phenomenon which physically cannot occur on the integrated flap. The higher moment for the discrete flap airfoil is due

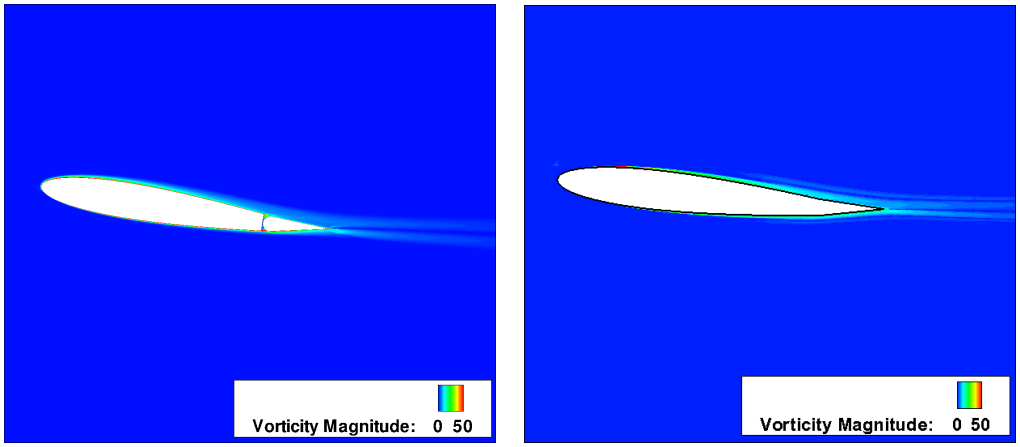

(a) Discrete flap (b) Integrated flap

Figure 80: NACA 0012 airfoil flow field vorticity for dynamic oscillations of $\alpha_{mean} = 4°$ and $\phi = 148°$, $M_\infty = 0.4$, $Re_\infty = 1.63$ million, $k_{airfoil} = 0.021$, $k_{flap} = 0.042$ applying constant contour levels at all locations.

to energized flow from the gap traveling across the flap moving lift production from the airfoil to the flap. This effect is most pronounced with downward flap deflection during the beginning of the downtroke (Fig. 78) due to the positive angle of attack of the airfoil.

8.5.3 Dynamic Stall (mean $\alpha = 11°$)

The data for the more deeply stalled flapped NACA 0012 airfoil at a higher mean angle of attack of 11° and phase shift of $\phi = 177°$ in the form of the integrated coefficients exhibits dynamic stall behavior (Fig. 81). As with the lower angle of attack scheduling, the digitized experimental motions (Fig. 81(d)) are utilized to overcome limitations of the reported equations to capture the true motion. As the angle of attack exceeds 14°, the airfoil undergoes dynamic stall. The GT-HRLES model is able to predict the onset of dynamic stall, although it over predicts the moment excursion.

8.5.3.1 Flow Field

At the beginning of the cycle, $\alpha = 10.6°$, the flow over the airfoil (Fig. 82(a)) is smooth and attached except in the vicinity of the gap. The vorticity pattern in the gap is associated with stagnation of the flow on the lower surface of the flap and mass flow upward through the gap (Figs. 83(a) and 84(a)). The mass flow rate is not enough to detach the flow and the fluid travels along the upper surface of the flap to the trailing edge. The flap stagnation

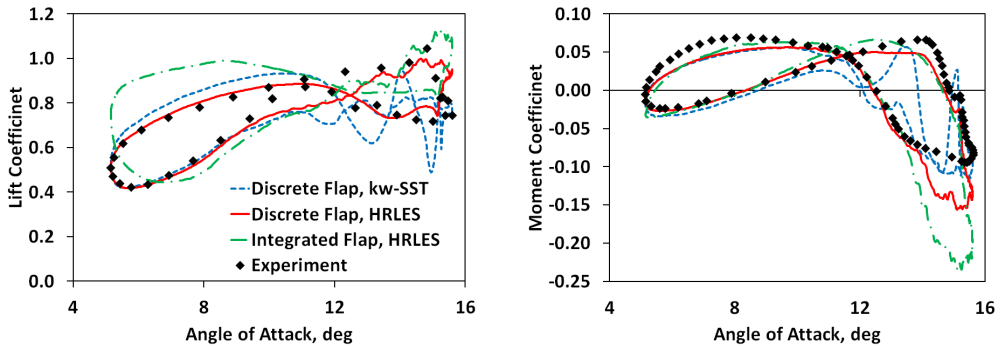

(a) Lift

(b) Moment

(c) Drag

(d) Motion

Figure 81: NACA 0012 airfoil integrated coefficient response and input motion with $\alpha_{mean} = 11^{\circ}$ and $\phi = 177^{\circ}$, $M_{\infty} = 0.4$, $Re_{\infty} = 1.63$ million, $k_{airfoil} = 0.021$, $k_{flap} = 0.042$.

point and suction peak appear in the pressure distribution (Fig. 85(a)).

As the angle of attack increases to $\alpha = 13.3°$, the pressure difference across the gap increases and a weak jet begins to emanate from the gap. Evidence of the jet is observed in both the velocity contours (84(b)) and two lines of vorticity in the upper half of the gap (83(b)). As before, the flow stagnates on the lower surface of the flap leading edge; however, the suction peak on the flap is stronger as the flow accelerates through the gap (Fig. 85(b)). The gap jet helps to start a clockwise vortex on the upper surface of the flap, and a counter-clockwise vortex upstream of the gap. At this point in the cycle the lift is still maintained and moment excursion has not yet occurred.

During the moment excursion but before the drop in lift ($\alpha = 14.98°$ during the upstroke), the gap jet supports a four core vortex pattern above the airfoil (Fig. 82(c)). The jet has aided in the creation of two counter-rotating vortices on the upper surface at the mouth of the gap. The suction peak has begun to drop due to separation on the upper surface (Fig. 85(c)); however, lift production has increased on a region of the airfoil starting approximately 0.6 chords upstream from the gap (the location of the jet-aided vortex). It is this flow region that initiates the moment excursion, while maintaining lift. This local in lift is maintained as the cycle progresses, despite a drop in the suction peak, amplifying the moment excursion.

In addition to the counter-rotating vortices near the flap gap jet, there is a clockwise vortex forming near the mid-chord and vortex rolling up the trailing edge. This four vortex pattern is maintained throughout the massively separated region of the cycle. Alternating vortices are shed into the flow via the upper surface and the trailing edge.

The airfoil maintains the pitch angle briefly at the maximum angle of attack before beginning the downstroke while the flap rotates downward. The vortical flow field does not significantly change (Fig 82(d)), but the suction peak continues to drop. This correlates with the decreased lift production and increased moment magnitude characteristic of dynamic stall (Fig. 74). The significance of the gap presence continues to be the vortex pattern in the flow field maintained by the jet.

The downstroke of the airfoil is characterized by gradual recovery and reattachment of

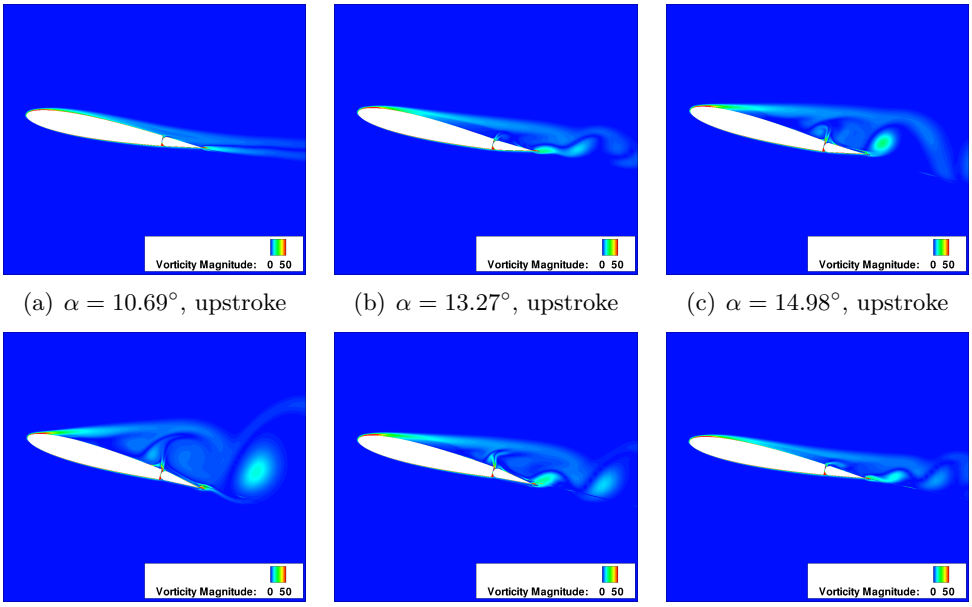

(a) $\alpha = 10.69°$, upstroke (b) $\alpha = 13.27°$, upstroke (c) $\alpha = 14.98°$, upstroke

(d) $\alpha = 15.48°$, downstroke (e) $\alpha = 13.52°$, downstroke (f) $\alpha = 11.79°$, downstroke

Figure 82: NACA 0012 airfoil-flap gap flow field vorticity airfoil-flap gap for dynamic oscillations of $\alpha_{mean} = 11°$ and $\phi = 177°$, $M_\infty = 0.4$, $Re_\infty = 1.63$ million, $k_{airfoil} = 0.021$, $k_{flap} = 0.042$ applying constant contour levels at all locations.

the flow (Fig. 82(e)). At the beginning of the downstroke, the lift does not recover, but the suction peak begins to increase (Fig: 85(e)). The vortices on the upper surface weaken, which moves lift production towards the leading edge and reduces the moment excursion. A gap jet is still present (Figs. 83(e) and 84(e)), but the degree of separation of the upper is reduced due to the decreased angle of attack.

Flow reattachment on the airfoil leads to recovery of lift and reduced moment excursion at lower angles of attack (Fig. 82(f)). The flow at the flap leading edge mimics reattachment of the airfoil leading edge flow. Decreased curvature and pressure gradient along with freestream stream-wise momentum result in the conventional boundary layer flow once the angle of attack drops. At this point in the cycle the flow characteristics are qualitatively similar to the NACA 0012 airfoil $\alpha_{mean} = 4°$, $\phi = 148°$ case for the portion of the cycle with recirculating flow in the lower portion of the gap.

The separation point variation with angle of attack, flap deflection angle, and total flap inclination angle indicate flow reversal on both the airfoil and flap upper surfaces (Fig. 86). The flow reversal point begins at the trailing edge and traverses the upper surface to the

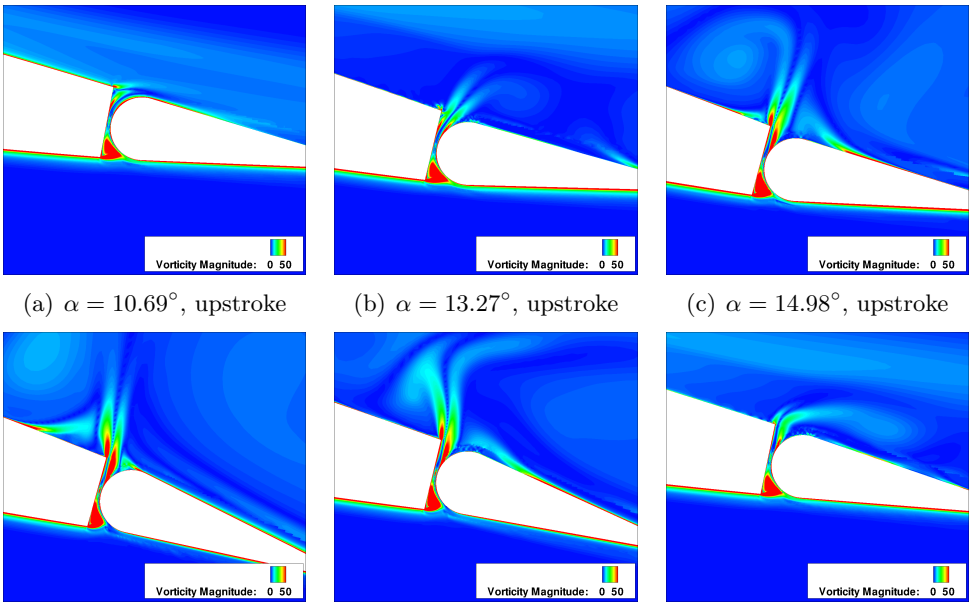

(a) $\alpha = 10.69°$, upstroke (b) $\alpha = 13.27°$, upstroke (c) $\alpha = 14.98°$, upstroke

(d) $\alpha = 15.48°$, downstroke (e) $\alpha = 13.52°$, downstroke (f) $\alpha = 11.79°$, downstroke

Figure 83: Vorticity within the NACA 0012 airfoil-flap gap for dynamic oscillations of $\alpha_{mean} = 11°$ and $\phi = 177°$, $M_\infty = 0.4$, $Re_\infty = 1.63$ million, $k_{airfoil} = 0.021$, $k_{flap} = 0.042$ applying constant contour levels at all locations.

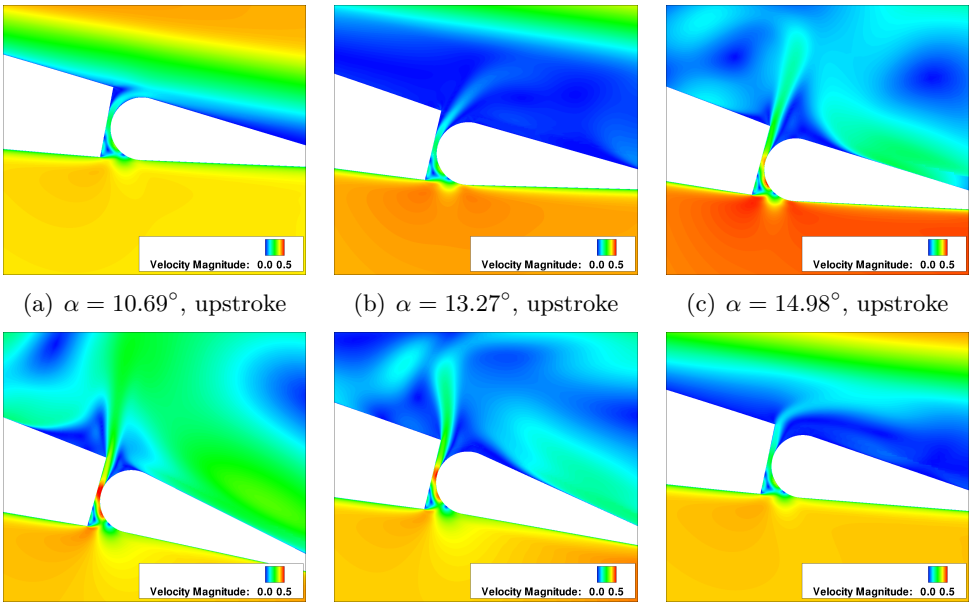

(a) $\alpha = 10.69°$, upstroke (b) $\alpha = 13.27°$, upstroke (c) $\alpha = 14.98°$, upstroke

(d) $\alpha = 15.48°$, downstroke (e) $\alpha = 13.52°$, downstroke (f) $\alpha = 11.79°$, downstroke

Figure 84: Velocity magnitude within the NACA 0012 airfoil-flap gap for dynamic oscillations of $\alpha_{mean} = 11°$ and $\phi = 177°$, $M_\infty = 0.4$, $Re_\infty = 1.63$ million, $k_{airfoil} = 0.021$, $k_{flap} = 0.042$ applying constant contour levels at all locations.

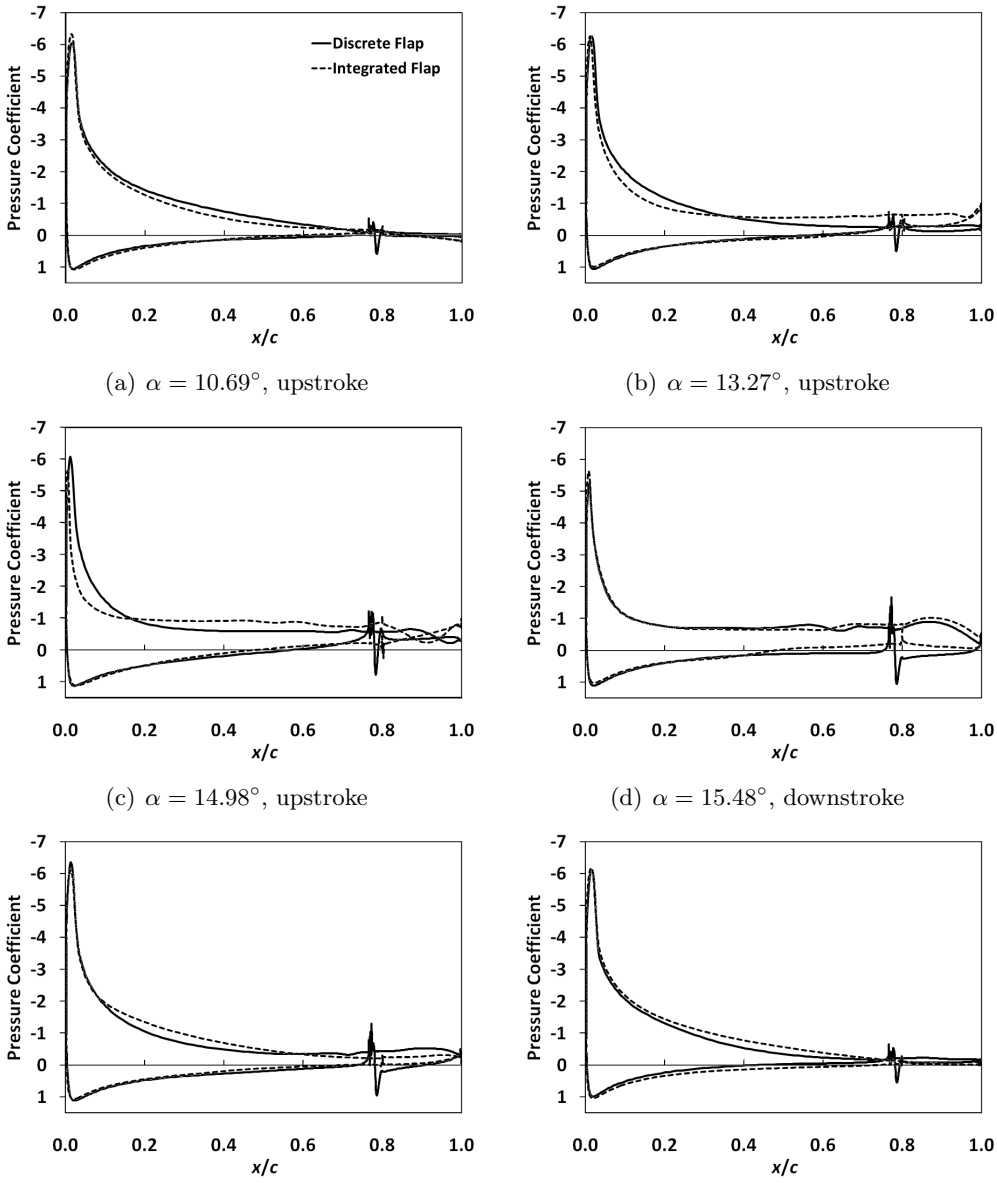

(a) $\alpha = 10.69°$, upstroke

(b) $\alpha = 13.27°$, upstroke

(c) $\alpha = 14.98°$, upstroke

(d) $\alpha = 15.48°$, downstroke

(e) $\alpha = 13.52°$, downstroke

(f) $\alpha = 11.79°$, downstroke

Figure 85: Pressure coefficient distribution of the NACA 0012 airfoil with discrete or integrated flap (discrete flap has gap) for dynamic oscillations of $\alpha_{mean} = 11°$ and $\phi = 177°$, $M_\infty = 0.4$, $Re_\infty = 1.63$ million, $k_{airfoil} = 0.021$, $k_{flap} = 0.042$ applying constant contour levels at all locations.

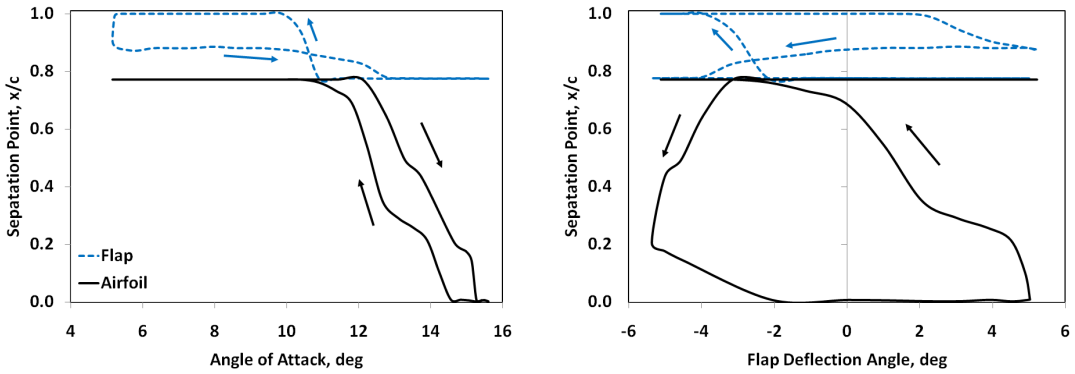

(a) Variation with angle of attack

(b) Variation with flap deflection angle

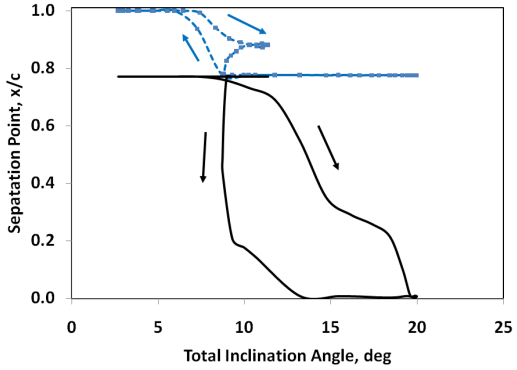

(c) Variation with total flap inclination angle

Figure 86: NACA 0012 flap separation point variation for $\alpha_{mean} = 11°$ and $\phi = 177°$, $M_\infty = 0.4$, $Re_\infty = 1.63$ million, $k_{airfoil} = 0.021$, $k_{flap} = 0.042$; constant plot ranges across all time samples.

leading edge.

As the angle of attack increases, separation is observed on the airfoil at $\alpha = 12.5°$, and the flap is fully stalled at $\alpha = 13.2°$. Both components are fully stalled near the maximum angle of attack, followed by initial downstream movement of the separation point at $\alpha = 14.6°$.

Sound pressure levels for the flapped NACA 0012 airfoil (Fig. 87) are calculated as outlined in the development of the acoustic analysis in the reproduction of cavity flow. Peaks exist for both the 4° and 11° flapped NACA 0012 airfoil configurations at 5 and 10 Hz (Fig. 87(a)), which correspond to the oscillation cycles of the airfoil and flap, respectively. The spectrum of the mean angle of attack of 4° case, which was attached throughout the predictions, has no other dominant modes. The spectrum of the mean angle of attack of

11° case exhibits additional broadband noise from 100 to 700 Hz. This frequency range corresponds to a Strouhal number range of 0.14 to 0.94, and is associated with massive vortex shedding on the upper surface of the airfoil and unsteadiness of the gap jet.

8.5.3.2 Comparison with Integrated Flap

As with the previous case, an integrated flap was considered for the flapped NACA 0012 airfoil with an identical computational setup. Again, the average lift was higher for the integrated flap compared with the discrete flap with a gap, while the drag was lower for angles of attack below 13°. At higher, stalled angles of attack the moment and drag were roughly equal on the upstroke for both the integrated and discrete flap cases, while on the downstroke the integrated flap generally had lower lift and higher pitching moment.

Examination of the flow field vorticity of the discrete (82) and integrated (88) flap cases provides some insight. During flow separation on the upstroke, there is increased vorticity aft of the quarter-chord for the integrated flap case (Figs. 88(b) and 88(c)). During the downstroke, the flow is reattaches more quickly without the presence of the gap jet (Figs. 88(e) and 88(f)). The effect of the gap is to delay stall with higher energy flow from the lower surface. Before stall, flow travels through the gap and stays attached to the surface (Fig 83(a)). This high energy flow delays stall such that the flow during the upstroke is significantly more attached for the discrete flap case (Fig. 82(c)) compared with integrated flap case (Fig. 88(c)). The integrated airfoil is more deeply stalled at a higher angle of attack, resulting in the larger excursions on the moment and drag coefficient plots (Figs. 81(b) and 81(c)). Conversely, the flow remains stalled longer on the downstroke for the discrete flap case (Fig. 82(d)) than the integrated flap case (Fig. 88(d)) due to the gap jet that aids separation (Fig. 83(d)).

Delayed stall is also observed in the pressure coefficient distributions (Fig. 85). At $\alpha = 10.69°$ during the upstroke (Fig. 85(a)) the lift and moment coefficient are nearly equal (Figs. 81(a) and 81(b)). As the angle of attack increases, the integrated flap airfoil stalls before the discrete flap airfoil. As this occurs, lift production moves aft of the quarter-chord

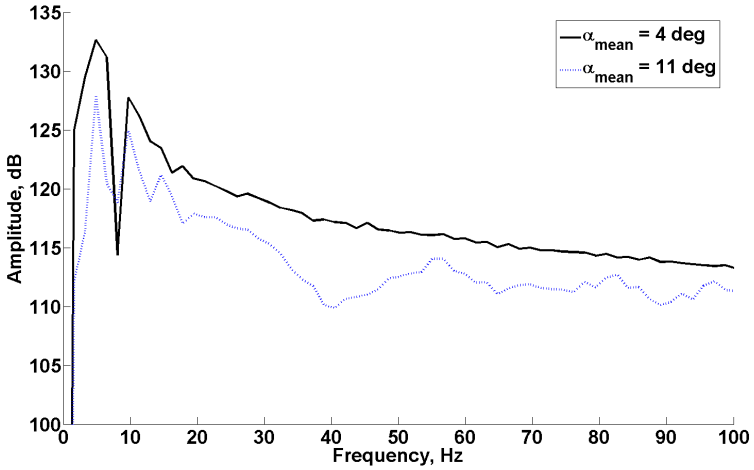

(a) Higher frequency peaks

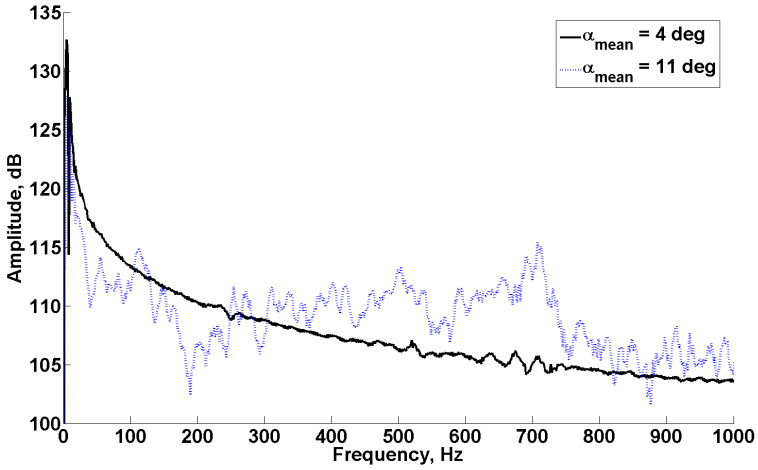

(b) Lower frequency peaks

Figure 87: NACA 0012 airfoil sound pressure levels, $M_\infty = 0.4$, $Re_\infty = 1.63$ million, $k_{airfoil} = 0.021$, $k_{flap} = 0.042$.

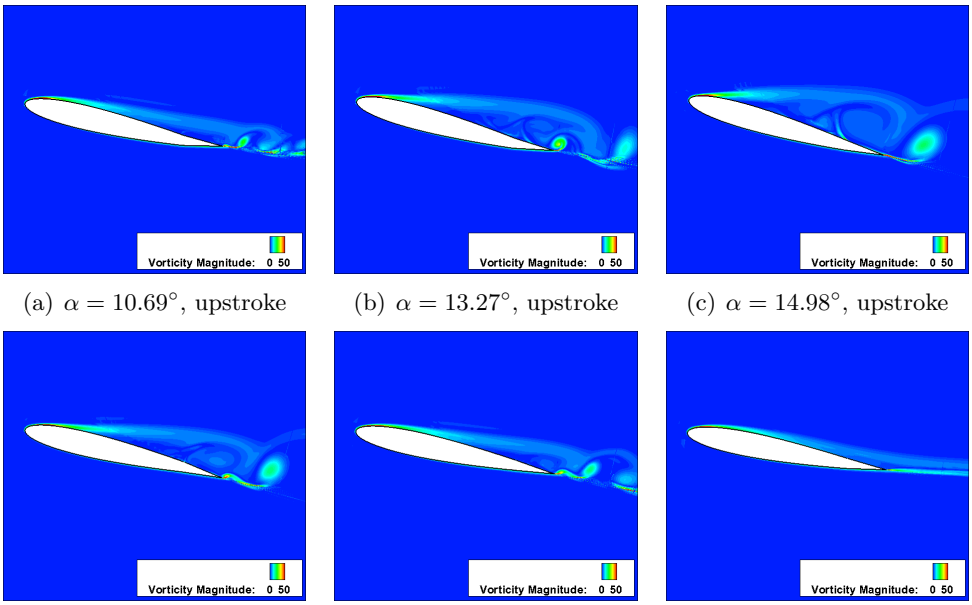

(a) $\alpha = 10.69°$, upstroke (b) $\alpha = 13.27°$, upstroke (c) $\alpha = 14.98°$, upstroke

(d) $\alpha = 15.48°$, downstroke (e) $\alpha = 13.52°$, downstroke (f) $\alpha = 11.79°$, downstroke

Figure 88: NACA 0012 integrated flap airfoil flow field vorticity for dynamic oscillations of $\alpha_{mean} = 11°$ and $\phi = 177°$, $M_\infty = 0.4$, $Re_\infty = 1.63$ million, $k_{airfoil} = 0.021$, $k_{flap} = 0.042$ applying constant contour levels at all locations.

for the integrated flap case (Figs. 85(b) and 85(c)), increasing the moment excursion considerably, while the lift remains higher than the discrete flap airfoil. The moment excursion due to stall continues through the beginning of the downstroke (Fig. 85(d)). Delayed stall recovery is evident for the discrete flap case during the downstroke due to the effect of the gap jet (Fig. 85(e)). Once the flow reattaches, the moment coefficients again become nearly identical between the two airfoil cases, while the integrated flap maintains a higher lift coefficient (Fig. 85(f)).

8.6 Results for Flapped VR7 Airfoil

The results are analyzed according to each study parameter: reduced frequency of flap oscillation, angle of attack, free stream speed, and size of the airfoil-flap gap for low and high angles of attack. These VR7 airfoil results may also be found in a publication by Liggett and Smith [99].

8.6.1 Reduced Frequency Dependence

The lift, moment, and drag hysteresis data were recorded as a function of flap deflection angle for each reduced frequency case (Fig. 89) at $\alpha = 10.5°$. Due to the low angle of attack, lift, drag, and moment generally remain within the linear regime with respect to the flap deflection angle, but stall is observed only at the lowest reduced frequency of $k = 0.118$ above flap deflection angles of 1°. This stall is suppressed as the reduced frequency is increased from $k = 0.118$ to $k = 0.237$. Suppression of stall leads to non-monotonic changes in the lift, drag, and moment averaged values and sensitivities. As the flap reduced frequency is increased ($k = 0.118$, 0.237, and 0.355), the average lift initially decreases by 2% and subsequently increases by 8%. The average drag has the opposite behavior, first increasing by 2% and then decreasing by 11%. This non-monotonic behavior is the direct result of the stall that is suppressed by the increased flap reduced frequency and the influence of the flap deflection angle. The drag and moment coefficients decrease by 23% and 25%, respectively, as the reduced frequency increases from $k = 0.118$ to $k = 0.237$. A further increase in the reduced frequency of the flap decreases the lift by 32% due to the reduced time the flow has to respond, but does not affect the drag and moment sensitivities. A phase lag between the flap deflection input and the airfoil aerodynamic response is also observed that grows with increasing flap reduced frequency.

The sound pressure level distributions exhibit peak modes (Fig. 90) that track the frequencies of the flap oscillations (Table 19). The uncertainty in the frequency transform is $\Delta f = 1/\left(N_{samples}\Delta t\right)$. Here, the number of samples used for frequency analysis is $N_{samples}$, while the time step between samples is Δt. The total frequency uncertainty based on this analysis is ±3 Hz; the peak modes observed match the flap oscillation frequencies to within this ±3 Hz uncertainty (Table 19). Smaller peaks are also observed at integer multiples of the corresponding oscillation frequency. Peaks at only the component oscillation frequencies are expected, as analysis of the $\alpha = 10.5°$ data revealed very little separation or flow reversal on the airfoil or flap surfaces outside the gap. Very low sound pressure levels observed at higher frequencies are consistent with a smoothly varying flow field that does not exhibit separation or unsteadiness.

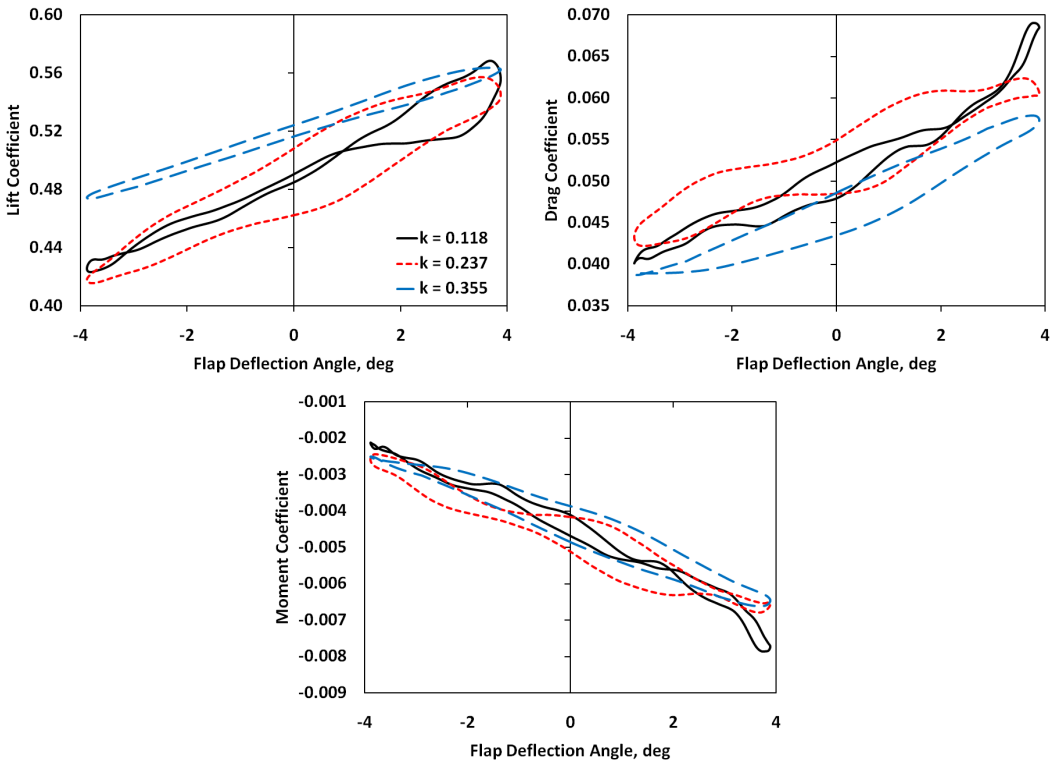

Figure 89: Flapped VR7 airfoil integrated coefficients as a function of flap deflection angle δ with $M_\infty = 0.475$, $Re_\infty = 1.51$ million, and $\alpha = 10.5°$ for varying reduced frequencies.

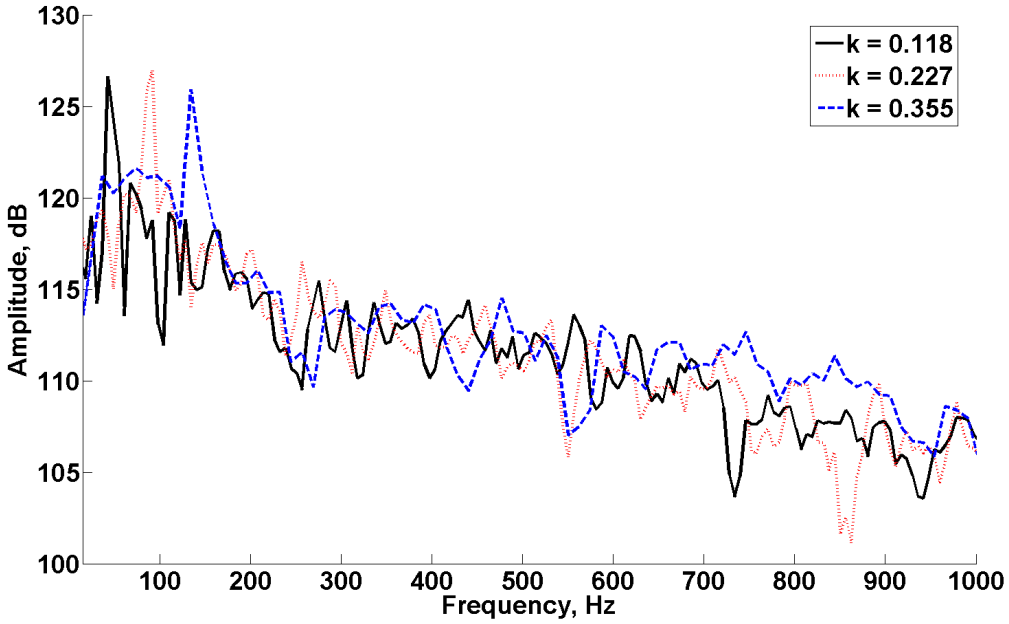

Figure 90: Flapped VR7 sound pressure levels with varying flap oscillation frequencies with $M_\infty = 0.475$, $Re_\infty = 1.51$ million, and $\alpha = 10.5°$.

Table 19: Peak frequencies for flapped VR7 airfoil with varying flap oscillation frequencies.

Flap Reduced Frequency	Flap Dimensional Frequency Hz	SPL Peak Hz	Error %
0.118	44.5	43.9	1.3
0.237	89.1	91.5	2.7
0.355	133.6	134.6	0.7

Table 20: Peak frequencies for flapped VR7 airfoil with varying angles of attack.

Angle of Attack deg	Flap Dimensional Frequency Hz	SPL Peak Hz	Error %
10.5	44.5	42.1	5.4
18.5	44.5	42.9	3.7
18.5	44.5	650–900	-

8.6.2 Angle of Attack Dependence

Variations in the lift, drag, and moment with flap deflection are investigated for $\alpha = 10.5°$ and $18.5°$ at a reduced flap oscillation frequency of $k = 0.118$ (Fig. 91). These two conditions feature attached and separated flows, respectively. Stalling of the flow alters the average lift by less than 1% between $\alpha = 10.5°$ and $\alpha = 18.5°$, but the moment and drag increase by 100% and 220%, respectively. These large increases in moment and drag are consistent with previous observations of stalled airfoils [81].

Sensitivity of the performance coefficients to flap deflection angle varies significantly between attached and stalled flows. As the airfoil stalls, the lift and moment decrease by 54% and 36%, respectively, while the drag sensitivity is nearly constant. Decreased lift and moment coefficients are also observed as the flap exhibits decreased authority in a separated flow.

Peaks at 44 Hz in the frequency spectra of both angles of attack (Fig. 92) again match the flap oscillation frequencies within the error bounds of the analysis (Table 20). The stalled angle of attack case has a smaller peak at 44 Hz and more energy at the higher frequencies between 650 Hz and 900 Hz. This frequency range corresponds to a Strouhal number range of 0.14 to 0.19 when the flap chord is used as the reference length. This Strouhal number range is associated with vortex shedding for separated flows [100], indicating the discrete flap drives production of unsteadiness in the separated region.

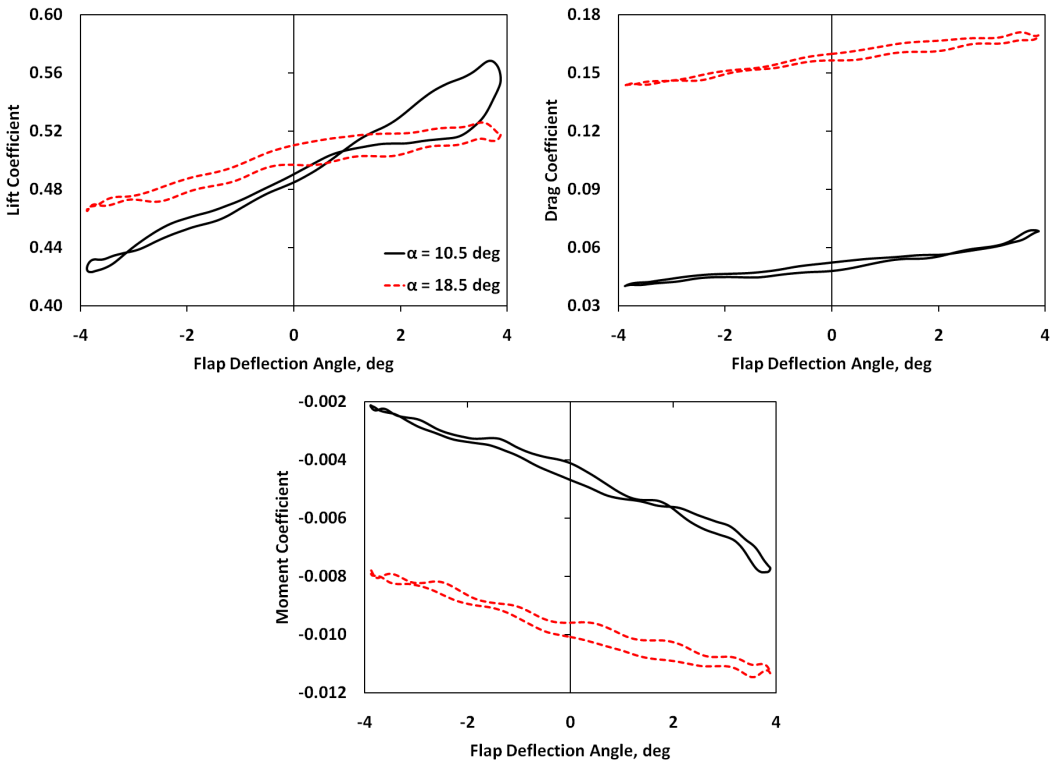

Figure 91: Flapped VR7 airfoil integrated coefficients as a function of flap deflection angle δ with $M_\infty = 0.475$, $Re_\infty = 1.51$ million, and $k = 0.118$ for varying angles of attack.

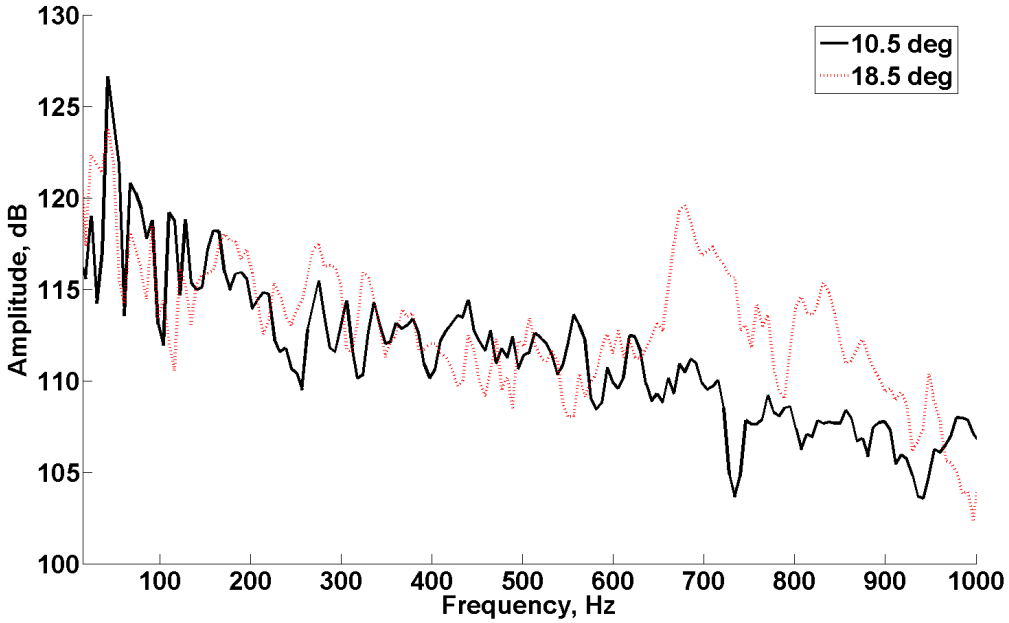

Figure 92: Flapped VR7 airfoil sound pressure levels with $M_\infty = 0.475$, $Re_\infty = 1.51$ million, and $k = 0.118$ varying angles of attack.

Table 21: Peak frequencies for flapped VR7 airfoil with varying speeds.

Reynolds Number RPM	Flap Dimensional Frequency Hz	SPL Peak Hz	Error %
1.51×10^6	89.1	91.0	2.2
1.02×10^6	60.0	60.8	1.3

8.6.3 Free Stream Speed Dependence

The free stream speed was varied, resulting in Reynolds numbers corresponding to 1.02 and 1.51 million per total chord. The reduced frequency of oscillation of the flap was constant at $k = 0.237$ at a fixed angle of attack of $\alpha = 10.5°$. Variation of the free stream speed alters the Mach number and dimensional frequency of flap oscillation (cases 2 and 5 from Table 18). The average drag coefficient drops by 20% with decreased free stream velocity, while the lift coefficient increases by 11% (Fig. 93). The averaged moment coefficient remains relatively unchanged. Differences in sensitivity to the flap deflection angle (reductions of 36%, 44%, and 30% for the lift, drag, and moment, respectively, with decreasing free stream speed) observed are a direct result of reductions in the free stream speed.

Lower free stream speed, which corresponds to lower dimensional flap oscillation frequency, was also associated with a $2° - 3°$ smaller lag between the flap deflection input and the aerodynamic response; the moment was the most significantly affected. The lower frequency of oscillation of the flap allows more time for the airfoil to respond aerodynamically.

As before, the peak frequencies of the sound pressure levels correlate with the flap oscillation frequencies (Fig. 94). The large 6.2 dB drop in the peak mode for the low speed case can be attributed to the fact that the low speed flow has less than half the energy of the high speed flow. Variation of the angle of attack resulted in altered peak modes, but the overall spectra are similar in amplitude (Fig. 92). This is not true for variation of the speed, which results in a shift downward of the entire spectrum with decreased speed. Higher frequency peaks are not observed with these attached flows.

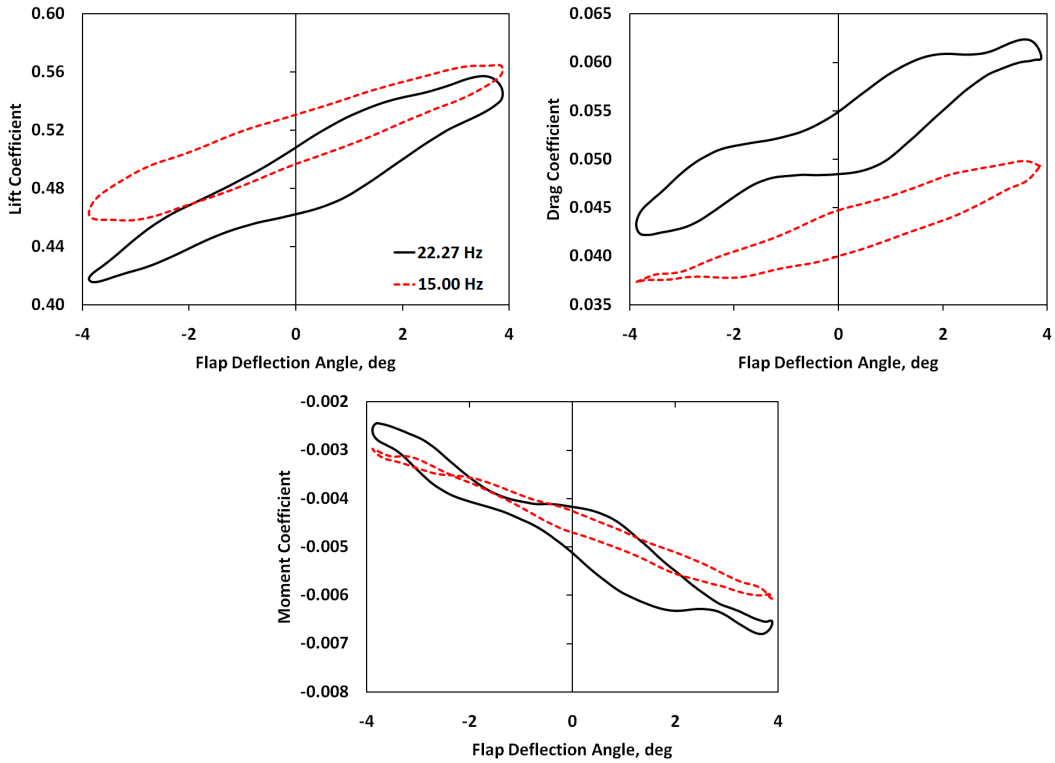

Figure 93: Flapped VR7 airfoil integrated coefficients as a function of flap deflection angle δ with $k = 0.237$ and $\alpha = 10.5^\circ$ for varying speeds: case 1 (flap oscillating at 22.27 Hz, Re = 1.51×10^6, and M = 0.475); case 2 (flap oscillating at 15.00 Hz, Re = 1.02×10^6, and M = 0.320).

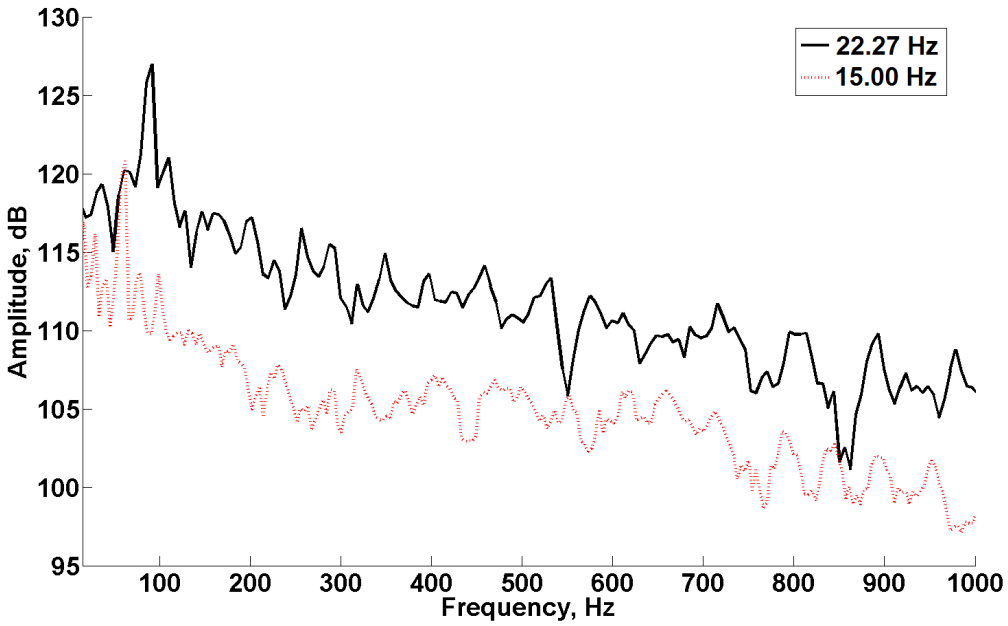

Figure 94: Flapped VR7 airfoil sound pressure levels with varying speeds: case 1 (1336 RPM, flap oscillating at 22.27 Hz, Re = 1.51×10^6, and M = 0.475); case 2 (900 RPM, flap oscillating at 15.00 Hz, Re = 1.02×10^6, and M = 0.320).

8.6.4 Gap Size Dependence

The dependence of the integrated coefficients on the size of the gap was assessed for an attached angle of attack of $\alpha = 10.5°$ (Fig. 95) and a separated angle of attack of $\alpha = 18.5°$ (Fig. 96). Gap sizes of nominal (0.035 in. or 1X), two times nominal (0.070 in. or 2X), and three times nominal (0.105 in. or 3X) were considered. As previously observed, there is a linear dependence of the integrated coefficients on the flap deflection angle.

The lift, moment, and drag vary in a non-monotonic manner with respect to gap size for both low and high angles of attack. For example, at $\alpha = 18.5°$ the average lift decreases by 0.2% as the gap size is doubled, and then increases by 3% as the gap size is tripled. The drag first increases by 2% and subsequently decreases by 5%. The slope of the coefficients with respect to flap deflection is also nonlinear. The lift sensitivity is 0.011 per degree with the smallest gap, decreases by 32% as the gap size increases, and then increases by 36% as the gap size further increases. The lag between the aerodynamic response and the input flap deflection generally increased with increased gap size. To a first order, this relationship

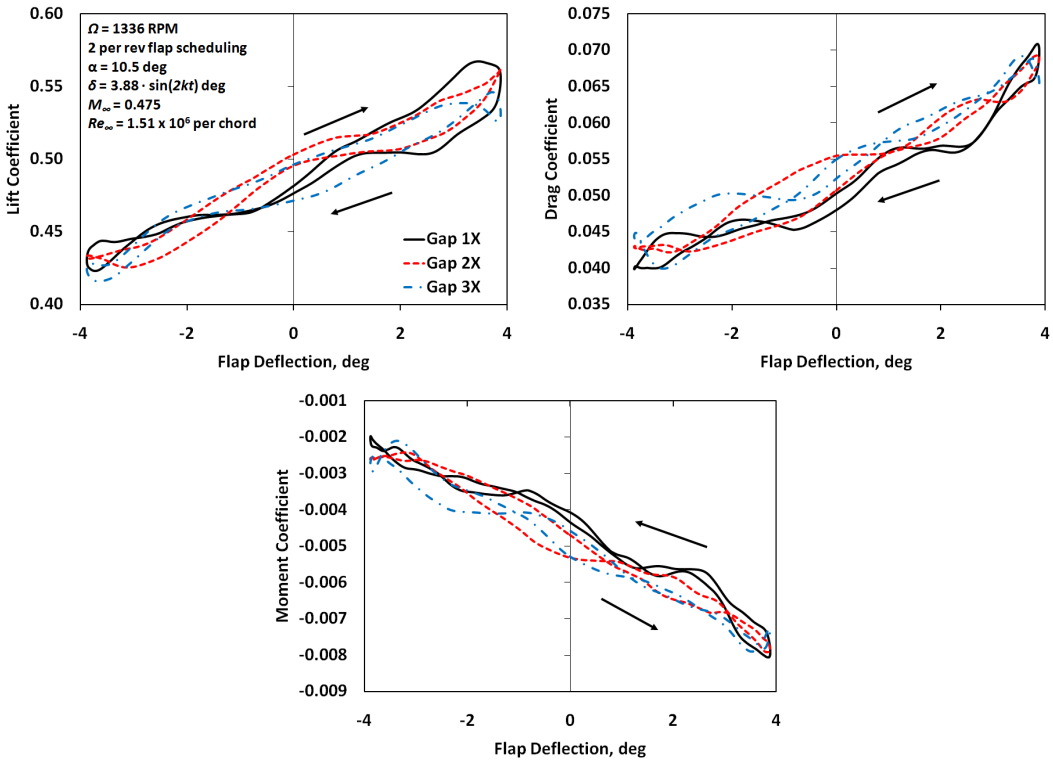

Figure 95: Flapped VR7 airfoil integrated coefficients as a function of flap deflection angle δ with $k = 0.118$, and $\alpha = 10.5°$ for varying gap sizes.

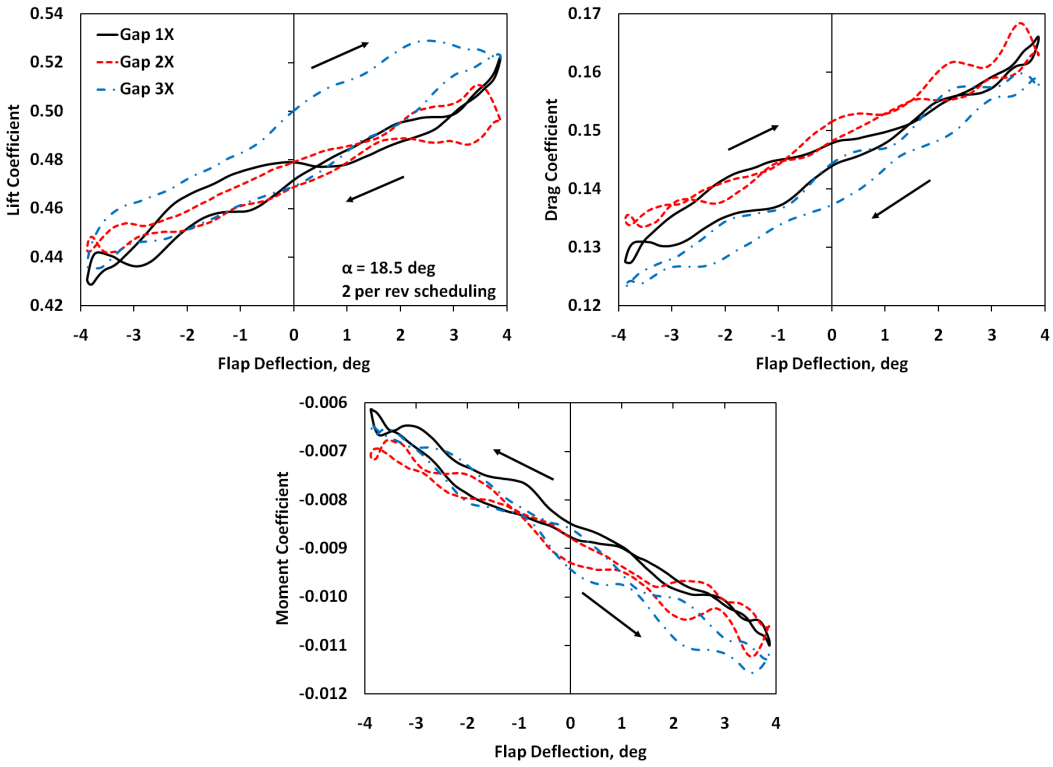

Figure 96: Flapped VR7 airfoil integrated coefficients as a function of flap deflection angle δ with $M_\infty = 0.475$, $Re_\infty = 1.51$ million, $k = 0.118$, and $\alpha = 18.5°$ for varying gap sizes.

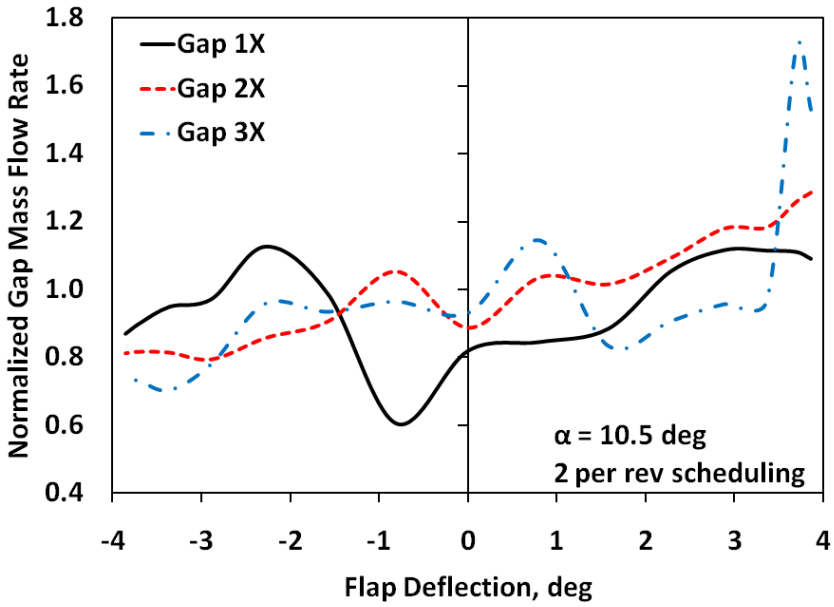

Figure 97: Flapped VR7 airfoil gap mass flow rate as a function of flap deflection angle δ with $M_\infty = 0.475$, $Re_\infty = 1.51$ million, $k = 0.118$, and $\alpha = 10.5°$ for varying gap sizes.

is linear. The volume of fluid between the airfoil and flap also increases linearly with gap size. As such, the lag increase may be attributed to the additional fluid volume within the gap.

The nonlinear variation of the airfoil performance quantities prompted investigation of the mass flow rate through the gap for the low and high angle of attack data (Figs. 97 and 98, respectively). The mass flow rates are normalized by the average mass flow rate for the respective 1X gap. As the flap deflection angle increased, the flow through the gap generally increased. This was due to the increased pressure difference across the gap associated with a downward deflected flap. The mass flow rate characteristics correlate with features observed in the integrated coefficient hysteresis data. If crossover is observed across all coefficients, then a sudden change in the mass flow rate is also present.

At low angles of attack, the average mass flow rate through the gap *increased* by 4% when the gap size was doubled. A further increase in gap size *decreased* the mass flow rate by 1%. The effects of gap size were significantly larger at higher angles of attack where the average mass flow rate *increased* by 35% as the gap width was doubled. A further increase in gap size at the high angle of attack *decreased* the mass flow rate by 40%. The larger

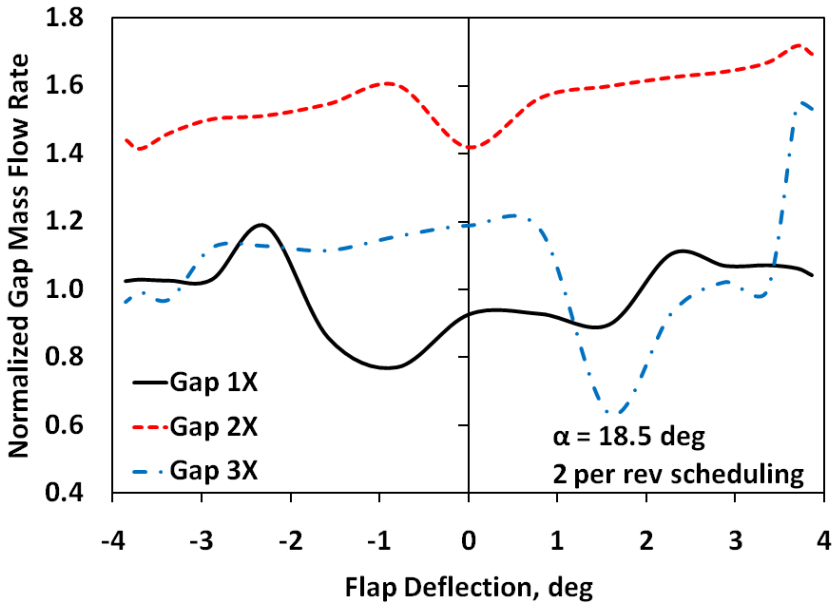

Figure 98: Flapped VR7 airfoil gap mass flow rate as a function of flap deflection angle δ with $M_\infty = 0.475$, $Re_\infty = 1.51$ million, $k = 0.118$, and $\alpha = 18.5°$ for varying gap sizes.

mass flow rate changes at higher angles of attack can be attributed to the larger pressure difference across the gap. The non-monotonic dependence can be understood by examining the vorticity within the gap (Fig. 99). The smallest gap is associated with interference of the jet with the airfoil. As the gap size is doubled, development of the jet is no longer confined by the airfoil and the mass flow rate increases. Further increases in the gap size result in a recirculation region just behind the blunt edge of the airfoil. This recirculation actually decreases the flow rate, explaining the non-monotonic dependence of mass flow rate on gap size. This could also lead to the observed non-monotonic dependence of the integrated coefficients.

8.6.5 Transition

Transition modeling provided the transition locations for each of the nine cases considered in this parametric study (Table 18). For all cases, transition at the leading edge of the airfoil was unaffected by the flap oscillation. None of the parameters (static angle of attack, flap oscillation frequency, freestream speed, and gap size) led to unsteadiness of the transition location. With the airfoil at a 10.50° angle of attack (cases 1, 2, 3, 5, 6, and 7), transition

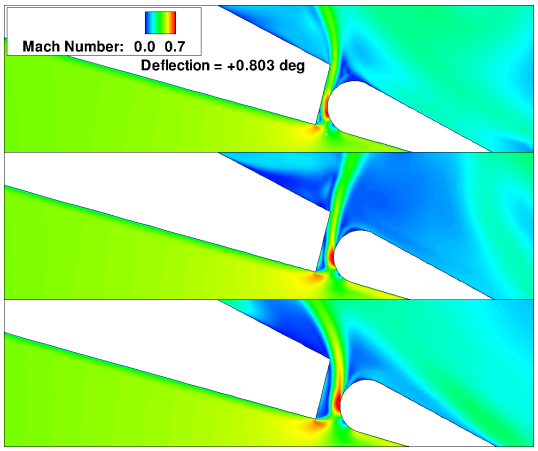

Figure 99: Flapped VR7 airfoil gap Mach flowfield at a flap deflection angle of $\delta = 0.8°$ with $M_\infty = 0.475$, $Re_\infty = 1.51$ million, $k = 0.118$, and $\alpha = 18.5°$ for varying gap sizes.

was observed at 4.7% of the chord, while for cases at an 18.50° angle of attack, transition occurred at 2.2% of the chord (cases 4, 8, and 9). At an 18.50° angle of attack, laminar flow at the leading edge led to a flow reversal bubble, but transition to turbulence provided energy to the flow to overcome the pressure gradient and remain attached before separation occurred further down the upper surface of the airfoil.

CHAPTER IX

CONCLUSIONS

Convergence of numerical solutions of flows about fixed and oscillating airfoils, where the flows include time-accurate flow features and/or motion, has been investigated using a popular two-equation RANS turbulence model and a hybrid RANS-LES turbulence method. Several specific conclusions can be drawn from this analysis.

1. Newton subiterations are routinely implemented with first order temporal algorithms to approach second order time accuracy. For separated flows, it is critical to have a time step size small enough to achieve true second order temporal convergence to capture accurate unsteady physics such as vortex shedding.

2. The time step needed to achieve second order temporal convergence is the same for both the RANS and hybrid RANS/LES turbulence methods, and can be obtained from a static stall computation, permitting efficient determination of the time step for both static and dynamic stall.

3. While the cost of the hybrid RANS/LES turbulence method is higher per iteration (and subiteration) than the RANS turbulence model, it typically converges faster and exhibits less error for the same time step size, so that the overall cost was less for hybrid turbulence approach.

4. The number of subiterations at a given time step for static stall is independent of the angle of attack, and can provide an estimation of the temporal characteristics needed to obtain converged solutions for a range of angles of attack.

5. Comparable numbers of subiterations of the mean and turbulent transport equations are sufficient to resolve the boundary layers in attached flows, but simulations of

separated flows require 2-4 additional turbulent subiterations for accurate boundary layer predictions.

6. Convergence of the turbulent transport equations controls the location of separation and stall onset, but the location of reattachment depends on the convergence of the mean flow equations.

7. Identification of a time step and subiteration combination sufficient to ensure convergence of dynamic stall can be obtained from the linear relation between the number of time steps/cycle $\times$ subiterations for integrated performance coefficients for fully attached flows.

8. Estimates of the accuracy of the numerical simulation (grid, turbulence model, etc.) to predict the integrated force and moment coefficients, and location of the stall onset and flow reattachment can be computed from linear extrapolation of their values with the number of subiterations or time steps/cycle $\times$ subiterations.

9. The significant computational costs associated with dynamic stall simulations can be optimized by a combination of the time step size and the subiterations that resolve the mean and turbulent transport equations.

A series of analyses using different turbulence simulations, including RANS Menter $k\omega$ *SST*, two hybrid RANS/LES methods known as DES-SST and GT-HRLES, and an LES-VLES technique known as KES, have been evaluated in a legacy RANS code, OVERFLOW, for a 5:1:1 cavity in a transonic free stream ($M_\infty = 0.85$). Characteristics of the simulations using time step size and simulation length have been examined. From these simulations, several conclusions can be reached:

1. All four turbulence approaches predict the large feedback vortical structures within the cavity, but only the DES-SST and GT-HRLES methods capture additional flowfield complexity, which may be due to the explicit transport of turbulent dissipation with subgrid-scale modeling.

2. Higher harmonics are apparent in the DES-SST and GT-HRLES simulations, which are not as apparent in the traditional RANS and KES approaches resulting from the large amount of complex vorticity apparent in the flowfield.

3. Verification of subsidence of initial transients and onset of periodicity of the simulations can be determined via the mean of the integrated pressures on the cavity floor with increasing analysis interval.

4. The RANS and KES models over-predict the overall sound pressure levels. The DES-SST method predicts lower sound pressure levels, but the GT-HRLES predictions are the most accurate when correlated with experimental measurements and LES results.

5. Comparisons of 0.5 s simulation interval frequency predictions for DES-SST and GT-HRLES methods demonstrates reproduction of the second and third harmonics much more accurately for GT-HRLES. The fourth harmonic is captured with a similar level of accuracy between the two methods. All predictions fall within error bounds of the analysis. The GT-HRLES modal frequencies are sensitive to time step size and simulation length. This confirms the need for a $0.5s$ simulation interval by Allen [43].

6. The GT-HRLES predictions of the peak modal sound pressure levels for frequencies below 1000 Hz are less sensitive to the time step size and simulation length than modal frequency locations, negating the recommendation of a $0.5s$ simulation interval by Allen [43].

7. The DES-SST and GT-HRLES predictions have similar performance for the 0.5 s analysis interval in terms of sound pressure level predictions. These predictions are comparable to previously published LES predictions for frequencies below 600 Hz for which this study was designed.

8. The GT-HRLES approach was able to predict SPL for the peak frequencies below 400Hz within 1dB and below 600 Hz within about 2 dB. Above 600Hz, the SPL predictions were within 10 dB, indicating the need for a grid with reduced aspect ratios and stretching below 15%, which was used in the present study.

The flow was predicted about an oscillating NACA 0012 airfoil with discrete and integrated flaps. The integrated coefficient hysteresis curves, vorticity, and gap flow were all examined for two cases: low and stalled mean angles of attack. The following conclusions can be made:

1. Flow within the non-contoured gap of an airfoil/flap configuration did not exhibit strong unsteadiness due to the small gap size. Power spectra featured peaks at component oscillation frequencies for all cases along with frequencies in the Strouhal number range of 0.14 to 0.94 for separated flows.

2. The direction of the gap flow was dominated by the flap deflection relative to the airfoil for attached flows. During stall, the flow direction through the gap was always upward.

3. At higher angles of attack, gap jets formed that fed counter-rotating vortices on the upper surface at the mouth of the discrete flap gap. This pattern of vorticity also featured a recirculation region near the airfoil leading edge, and a shedding trailing edge vortex.

4. At low angles of attack, the lift to drag ratio of the discrete flap airfoil was 40% lower than the integrated flap airfoil. The lift was higher for the integrated flap due to increased suction; the drag was higher for the discrete flap due to stagnation of the flow on the flap leading edge.

5. At high angles of attack, the effect of the discrete flap is to delay stall and recovery. The lift to drag ratio increased by 6% compared to an equivalent integrated flap airfoil.

6. Although gap flows can delay stall, non-contoured gaps are not recommended for design due to large associated performance losses at low angles of attack.

The flow about a static VR7 airfoil with a discrete oscillating flap has been predicted using an HRLES turbulence technique. The integrated coefficients were averaged over

several cycles of the flap oscillations to study the effects of a variety of parameters on the aerodynamic response of the airfoil. These parameters included flap scheduling, angle of attack, freestream speed, and airfoil-flap gap size. The following observations have been made:

1. Trailing edge stall present at low flap oscillation frequencies was suppressed as the flap oscillation frequency increased. An increase in the aerodynamic response lag of $6^\circ - 16^\circ$ was observed as stall was suppressed.

2. Higher angles of attack featured unsteadiness with Strouhal numbers in the range of 0.14 to 0.19 where the flap chord is the reference length; this indicates that the discrete flap drives unsteadiness in the flow separation region.

3. Flap oscillations did not affect the transition point location for the range of parameters considered in this study.

4. Interference of the gap flow with the airfoil surfaces was observed with gap sizes that are on the order of the boundary layer thickness. The lag between the aerodynamic response and flap input increased roughly linearly with the size of the gap.

5. A non-contoured gap is not recommended as it may lead to recirculation and non-linear effects that can reduce performance and increase analysis costs. If a discrete non-contoured flap is required, the airfoil-flap gap should be kept as small as possible to maximize effectiveness of the flap and reduce response lag.

CHAPTER X

RECOMMENDATIONS FOR FUTURE WORK

This work has focused on predictions of static and dynamic stall on flapped and unflapped airfoils. Recommended future extensions to the efforts presented here include:

1. Convergence and converged parameters are not well-predicted by the stalled region of the dynamic stall curve. This may be expected due to non-linearities in the stalled regime, but additional investigations with hybrid RANS/LES may provide insight.

2. Further analysis of the unsteady loads associated with the massively separated regions of flow and their interdependency with different turbulence models.

3. This study has considered a non-contoured discrete flap to provide comparison with an experimental dataset with the same configuration. Future studies would benefit from considering contoured flaps with gaps that may reduce losses compared to their non-contoured counterparts.

4. Continued work is recommended to investigate the effect of the application of simultaneous, independent airfoil pitch and flap deflection oscillations.

5. An eventual goal of analysis methods is to be applied in a real-world scenario. The use of the methodology in this thesis to a full rotor would provide invaluable data in a situation featuring yaw, span-wise flow acceleration, and finite flap or finite wing effects.

Bibliography

[1] Henshaw, M., "Verification and Validation Data for Computation Unsteady Aerodynamics: M219 Cavity Case," RTO-TR-26, NATO Research and Technology Organisation, October 2000.

[2] Savory, E., Toy, N., Tahouri, B., and Dalley, S., "Flow Regimes in the Cove Regions Between a Slat and Wing and Between a Wing and Flap of a Multielement Airfoil," *Experimental Thermal and Fluid Science*, vol. 5, no. 3, pp. 307–316, 1992.

[3] Watanabe, S., Kato, H., and Yamamoto, K., "Velocity Field Measurements of a Wing-Flap Configuration via Stereoscopic PIV," in 44^{th} AIAA Aerospace Sciences Meeting and Exhibit, AIAA 2006-0043, (Reno, NV), January 2006.

[4] Thakkar, D. and Ganguli, R., "Active twist control of smart helicopter rotor - A survey," *Journal of Aerospace Sciences and Technologies*, vol. 57, no. 4, pp. 429–448, March-April 2005.

[5] Lackner, M. A., "A Comparison of Smart Rotor Control Approaches Using Trailing Edge Flaps and Individual Pitch Control," *Wind Energy*, vol. 13, no. 2–3, pp. 117–134, March-April 2010.

[6] Hall, S. R. and Anand, R. V. and Straub, F. K. and Lau, B. H., "Active Flap Control of the SMART Rotor for Vibration Reduction," ARC-E-DAA-TN590, NASA, 2011.

[7] Cook, J., Smith, M., Thepvongs, S., and Cesnik, C., "Computational Aeroelasticity of Rotating Wings with Deforming Airfoils," *Journal of the American Helicopter Society*. submitted May 2012, under peer review, see also Cook, J., "Development of an Aeroelastic Methodology for Surface Morphing Rotors," PhD Disseration, Georgia Institute of Technology, Atlanta, GA, 2012.

[8] Cook, J. and Smith, M., "The Stability of Aeroelastic Airfoils with Camber Flexibility," *Journal of Fluids and Structures*. submitted June 2012, under peer review, see also Cook, J., "Development of an Aeroelastic Methodology for Surface Morphing Rotors," PhD Disseration, Georgia Institute of Technology, Atlanta, GA, 2012.

[9] Chandrasekhara, M., Martin, P. and Tung, C., "Compressible Stall Performance of a Variable Droop Leading Edge Airfoil with a Gurney Flap," *Journal of the American Helicopter Society*, vol. 53, no. 1, pp. 18–25, 2008.

[10] Wenzinger, C. and Harris, T., "Wind Tunnel Investigation of an N.A.C.A. 23012 Airfoil with Various Arrangements of Slotted Flaps," TM-664, NACA, 1939.

[11] Gothert, B. and Rober, C., "Systematic Investigations of the Effects of Planform and Gap Between the Fixed Surface and Control Surface on Simple Flapped Wings," TM-1206, NACA, 1949.

[12] Liu, L., Padthe, A., Quon, E., Friedmann, P., and Smith, M., "Unsteady Aerodynamics of Flapped Airfoils and Rotors Using Computational Fluid Dynamics and Approximate Methods," *Journal of the American Helicopter Society*, vol. 56, no. 3, p. 032003, 2011.

[13] Gerontakos, P. and Lee, T., "Unsteady Airfoil with Dynamic Leading- and Trailing-Edge Flaps," *Journal of Aircraft*, vol. 46, no. 3, pp. 1076–1081, 2009.

[14] Petz, R. and Nitsche, W., "Active Separation Control on the Flap of a Two-Dimensional Generic High-Lift Configuration," *Journal of Aircraft*, vol. 44, no. 3, pp. 865–874, 2007.

[15] Carr, L., Chandrasekhara, M., Wilder, M. and Noonan, K., "Effect of Compressibility on Suppression of Dynamic Stall Using a Slotted Airfoil," *Journal of Aircraft*, vol. 38, no. 2, pp. 296–309, 2001.

[16] Deck, S., "Zonal-Detached-Eddy Simulation of the Flow Around a High-Lift Configuration," *AIAA Journal*, vol. 43, no. 11, pp. 2372–2384, 2005.

[17] Khorrami, M., Choudhari, M., Singer, B., Lockard, D., and Streett, C., "In Search of Physics: The Interplay of Experiment and Computation in Slat Aeroacoustics," in 41^{st} AIAA Aerospace Sciences Meeting and Exhibit, AIAA 2003-0980, (Reno, NV), January 2003.

[18] V. Levasseur and P. Sagaut and M. Mallet and F. Chalot, "Unstructured Large Eddy Simulation of the Passive Control of the Flow in a Weapon Bay," *Journal of Fluids and Structures*, vol. 24, no. 8, pp. 1204–1215, 2008.

[19] Khorrami, M., C., Lockard, D., Singer, B., Choudhari, M., and Streett, C., "In Search of Physics: The Interplay of Experiment and Computation in Airframe Noise Research, Part 2," in 41^{st} AIAA Aerospace Sciences Meeting and Exhibit, AIAA 2003-0980, (Reno, NV), January 2003.

[20] Streett, C., Lockard, D., Singer, B., Khorrami, M., and Choudhari, M., "In Search of Physics: The Interplay of Experiment and Computation in Airframe Noise Research, Part 1," in 41^{st} AIAA Aerospace Sciences Meeting and Exhibit, AIAA 2003-0979, (Reno, NV), January 2003.

[21] Makiya, S., Inasawa, A., and Asai, M., "Vortex Shedding and Noise Radiation from a Slat Trailing Edge," *AIAA Journal*, vol. 48, no. 2, pp. 502–509, 2010.

[22] Biber, K., "Stall Hysteresis of an Airfoil with Slotted Flap," *Journal of Aircraft*, vol. 42, no. 6, pp. 1462–1470, 2005.

[23] Venkatakrishnan, L., Sundaram, S., and Viswanath, P., "Hysteresis and Broad Flow Features on a Swept Wing at High Lift," *Journal of Aircraft*, vol. 43, no. 4, pp. 1036–1043, 2006.

[24] Balaji, R., Bramkamp, F., Hesse, M. and Ballmann, J., "Effect of Flap and Slat Riggings on 2-D High-Lift Aerodynamics," *Journal of Aircraft*, vol. 43, no. 5, pp. 1259–1271, 2006.

[25] Nakayamai, A., Kreplin, H. and Morgan, H., "Experimental Investigation of a Flowfield About a Multielement Airfoil," *AIAA Journal*, vol. 28, no. 1, pp. 14–21, 1990.

[26] Zhong, B., Scheurich, F., Titarev, V., and Drikakis, D., "Turbulent Flow Simulations Around a Multi-Element Airfoil Using URANS, DES and ILES Approaches," in 19^{th} AIAA Computational Fluid Dynamics, AIAA 2009-3799, (San Antonio, Texas), June 2009.

[27] Zhong, B., Tang, K., Drikakis, D., and Guo, S., "Numerical Simulations of Turbulent Flows around a High Lift Wing-Body Configuration," in 49^{th} AIAA Aerospace Sciences Meeting and Exhibit including the New Horizons Forum and Aerospace Exhibition, AIAA 2011-1043, (Orlando, FL), January 2011.

[28] Wokoeck, R., Krimmelbein, N., Ortmanns, J., Ciobaca, V. and Radespiel, R., "RANS Simulation and Experiments on the Stall Behaviour of an Airfoil with Laminar Separation Bubbles," in 44^{th} AIAA Aerospace Sciences Meeting and Exhibit, AIAA 2006-0244, (Reno, NV), January 2006.

[29] Sanchez-Rocha, M., Kirtas, M. and Menon, S., "Zonal Hybrid RANS-LES Method for Static and Oscillating Airfoils and Wings," in 44^{th} AIAA Aerospace Sciences Meeting and Exhibit, AIAA 2006-1256, (Reno, NV), January 2006.

[30] Smith, M., Liggett, N., and Koukol, B., "The Aerodynamics of Airfoils at High and Reverse Angles of Attack," *AIAA Journal of Aircraft*, vol. 48, no. 6, pp. 2012–2023, 2011.

[31] Krzysiak, A. and Narkiewicz, J., "Aerodynamic Loads on Airfoil with Trailing-Edge Flap Pitching with Different Frequencies," *Journal of Aircraft*, vol. 43, no. 2, pp. 407–418, March-April 2006.

[32] Lau, B., Obriecht, N., Gasow, T., Hagerty, B., Cheng, K., and Sim, B., "Boeing-SMART Test Report for DARPA Helicopter Quieting Program," TM 2010-216404, NASA, 2010.

[33] Kottapalli, S., "Low Speed and High Speed Correlation of SMART Active Flap Rotor Loads," in American Helicopter Society Aeromechanics Specialists Conference, (San Francisco, CA), pp. 45–81, January 2010.

[34] Kottapalli, S., "Enhanced Correlation of SMART Active Flap Rotor Loads," in 52^{nd} AIAA/ASME/ASCE/AHS/ASC Structures, Structural Dynamics and Materials Conference, AIAA 2011-1874, (Denver, CO), April 2011.

[35] Potsdam, M., Fulton, M., and Dimanlig, A., "Multidisciplinary CFD/CSD Analysis of the SMART Active Flap Rotor," in Proceedings of the 66^{th} Annual Forum of the American Helicopter Society, vol. 3, (Phoenix, AZ), pp. 1991–2012, May 2010.

[36] Jain, R., Yeo, H., and Chopra, I., "Investigation of Trailing-edge Flap Gap Effects on Rotor Performance Using CFD/CSD Coupling," in 50^{th} AIAA Aerospace Sciences Meeting including the New Horizons Forum and Aerospace Exposition, AIAA 2012-1044, (Nashville, TN), January 2012.

[37] McCroskey, W., McAlister, K., Carr, L. and Pucci, S., "An Experimental Study of Dynamic Stall on Advanced Airfoil Sections Volume 2. Pressure and Force Data," TM-84245, NASA, 1982.

[38] Carr, L., "Progress in Analysis and Prediction of Dynamic Stall," *Journal of Aircraft*, vol. 25, no. 1, pp. 6–17, 1998.

[39] Chandrasekhara, M., Wilder, M. and Carr, L., "Competing Mechanisms of Compressible Dynamic Stall," *AIAA Journal*, vol. 36, no. 3, pp. 387–393, 1998.

[40] DiOttavia, J., Watson, K., Cormey, J., Komerath, N. and Kondor, S., "Discrete Structures in the Radial Flow Over a Rotor Blade in Dynamic Stall," in 26^{th} AIAA Applied Aerodynamics Conference, AIAA 2008-7344, (Honolulu, HI), January 2008.

[41] Shelton, A., Abras, J., Jurenko, R. and Smith, M., "Improving the CFD Predictions of Airfoils in Stall," in 43^{rd} AIAA Aerospace Sciences Meetings and Exhibit, AIAA 2005-1227, (Reno, NV), January 2005.

[42] Komerath, N., Ahuja, K. and Chambers, F., "Prediction and Measurement of Flows Over Cavities - A Survey," in AIAA 25^{th} Aerospace Sciences Meetings, AIAA 0087-0166, (Reno, NV), 1987.

[43] Allen, R. and Mendonca, F., "DES Validations of Cavity Acoustics over the Subsonic to Supersonic Range," in 10^{th} AIAA/CEAS Aeroacoustics Conference, AIAA 2004-2862, May 2004.

[44] Syed, S. and Hoffmann, K., "Numerical Investigation of 3-D Open Cavity with and without Cover Plates," in 47^{th} AIAA Aerospaces Sciences Meeting Including The New Horizons Forum and Aerospace Exposition, AIAA 2009-551, 2009.

[45] Tucker, P., Menon, S., Merkle, C., Oefelein, J. and Yang, V., "Validation of High-Fidelity CFD Simulations for Rocket Injector Design," in 44^{th} AIAA/ASME/SAE/ASEE Joint Propulsion Conference & Exhibit, AIAA 2008-5226, (Hartford, CT), July 2008.

[46] Jameson, A., "Time Dependent Calculations Using Multigrid, with Applications to Unsteady Flows Past Airfoils and Wings," in 10^{th} Computational Fluid Dynamics Conference, AIAA 1991-1956, (Honolulu, HI), June 1991.

[47] Rumsey, C., Sanetrik, M., Biedron, R., Melson, N. and Parlette, E., "Efficiency and Accuracy of Time-Accurate Turbulent Navier-Stokes Computations," *Computers & Fluids*, vol. 25, pp. 217–236, February 1996.

[48] Dubuc, L., Cantariti, F., Woodgate, M., Gribben, B., Badcock, K. and Richards, B., "Solution of the Unsteady Euler Equations Using an Implicit Dual-Time Method," *AIAA Journal*, vol. 36, no. 8, pp. 1417–1424, August 1998.

[49] Campbell, C., "Convergence of Newton's Method for a Single Real Equation," NASA-TP-2489, NASA, June 1985.

[50] Pulliam, T., "Time Accuracy and the Use of Implicit Methods," AIAA 1993-3360, NASA, Ames Research Center, Moffett Field, CA, 1993.

[51] Newsome, R., "Navier-Stokes Simulation of Wing Tip and Wing Juncture Interactions for a Pitching Wing," in 25^{th} Fluid Dynamics Conference, AIAA 1994-2259, (Colorado Springs, CO), June 1994.

[52] Walsh, P. and Pulliam, T., "The Effect of Turbulence Model Solution on Viscous Flow Problems," in 39^{th} AIAA Aerospace Sciences Meeting and Exhibit, AIAA 2001-1018, (Reno, NV), January 2001.

[53] Szydlowski, J. and Costes, M., "Simulation of Flow Around a Static and Oscillating in Pitch NACA0015 Airfoil using URANS and DES," in Proceedings of the ASME Heat Transfer/Fluids Engineering Summer Conference 2004, vol. 2 B, (Charlotte, NC), pp. 891–908, 2004.

[54] Gleize, V., Szydlowski, J. and Costes, M., "Numerical and Physical Analysis of the Turbulent Viscous Flow Around a NACA0015 Profile at Stall," in European Congress on Computational Methods in Applied Sciences and Engineering, (Jyvaskyla, Finland), 2004.

[55] Costes, M., Gleize, V. and Szydlowski, J., "Grid Sensitivity Study for the Turbulent Viscous Flow Around a NACA0015 Airfoil at Stall," in 31^{st} European Rotorcraft Forum, (Florence, Italy), pp. 105.1–105.12, 2005.

[56] Costes, M., Gleize, V., Pape, A. and Richez, F., "Numerical Investigation of Laminar/Turbulent Transition Effects on the Dynamic Stall of an Oscillating Airfoil," in AHS Specialists Conference on Aerodynamics, vol. 2, (San Francisco, CA), pp. 761–782, 2008.

[57] Richter, K., Pape, A., Knopp, T., Costes, M., Gleize, V. and Gardner, A., "Improved Two-Dimensional Dynamic Stall Prediction with Structured and Hybrid Numerical Methods," in Annual Forum Proceedings - AHS International, vol. 3, (Fort Worth, TX), pp. 2434–2450, 2009.

[58] Klein, A., Richter, K., Altmikus, A., Lutz, T. and Kramer, E., "Unsteady Criteria for Rotor Blade Airfoil Design," in 35^{th} European Rotorcraft Forum, vol. 1, (Hamburg, Germany), pp. 358–367, 2009.

[59] Morton, S., Steenman, M., Cummings, R., Forsythe, J., Wurtzler, K., Squires, K., Woodson, S. and Spalart, P., "Multidisciplinary Applications of Detached-Eddy Simulation to Separated Flows at High Reynolds Numbers," in Proceedings of the Department of Defense High Performance Computing Modernization Program Users Group Conference, (Williamsburg, VA), pp. 103–111, June 2004.

[60] Menter, F., "Two-Equation Eddy-Viscosity Turbulence Models for Engineering Applications," *AIAA Journal*, vol. 32, no. 8, pp. 1598–1605, August 1994.

[61] Liggett, N. and Smith, M., "Cavity Flow Assessment Using Advanced Turbulence Methods," *Journal of Aircraft*, vol. 48, no. 1, pp. 141–156, 2011.

[62] Michel, R., "Etude de la Transition sur les Profiles d'Aile; Establissement d'un Critère de Determination de Point de Transition et Calcul de la Trainée de Profile Incompressible," 1/1578A, ONERA, 1951.

[63] Schlichting, H. and Gersten, K., *Boundary Layer Theory*. Springer-Verlag Berlin Heidelberg, Eighth ed., 2000.

[64] Smith, A. and Gamberoni, N., "Transition, Pressure Gradient and Stability Theory," Report ES 26388, Douglas Aircraft Company, Long Beach, CA, 1956.

[65] Ingen, J., "A Suggested Semi-Empirical Method for the Calculation of the Boundary Layer Transition Region," Report VTH-74, University of Delft, Department of Aerospace Engineering, Deflt, The Netherlands, 1956.

[66] Buning, P., Chiu, I., Obayashi, S. and Steger, J., "Numerical Simulation of the Integrated Space Shuttle Vehicle in Ascent," in AIAA Atmospheric Flight Mechanics Meeting, AIAA 1988-4359, (Minneapolis, MN), August 1988.

[67] Buning, P., Parks, S., Cham, W. and Renze, K., "Application of the Chimera Overlapped Grid Scheme to Simulation of Space Shuttle Ascent Flows," in Proceedings of the 4^{th} International Symposium on Computational Fluid Dynamics, vol. 1, (Davis, CA), pp. 132–137, 1991.

[68] Meakin, R., "Object X-Rays for Cutting Holes in Composite Overset Structured Grids," in 15^{th} AIAA Computational Fluid Dynamics Conference, AIAA 2001-2537, (Anaheim, CA), June 2001.

[69] Nichols, R., Tramel, R. and Buning, P., "Solver and Turbulence Model Upgrades to OVERFLOW 2 for Unsteady and High-Speed Applications," in 24^{th} Applied Aerodynamics Conference, AIAA 2006-2824, (San Francisco, CA), June 2006.

[70] Wilcox, D., "Reassessment of the Scale-Determining Equation for Advanced Turbulence Models," *AIAA Journal*, vol. 26, no. 11, pp. 1299–1310, November 1988.

[71] Nichols, R., "Comparison of Hybrid Turbulence Models for a Circular Cylinder and a Cavity," *AIAA Journal*, vol. 44, no. 6, pp. 1207–1219, 2006.

[72] Shelton, A., Braman, K., Smith, M. and Menon, S., "Improved Hybrid RANS-LES Turbulence Models for Rotorcraft," *AIAA Journal*, vol. 32, no. 8, pp. 1598–1605, August 1994.

[73] Baurle, R., Tam, C., Edwards, J. and Hassan, H., "Hybrid Simulation Approach for Cavity Flows: Blending, Algorithm, and Boundary Treatment Issues," *AIAA Journal*, vol. 41, no. 8, pp. 1463–1480, August 2003.

[74] Fang, Y. and Menon, S., "A Two-Equation Subgrid Model for Large-Eddy Simulation of High Reynolds Number Flows," in 44^{th} AIAA Aerospace Sciences Meeting and Exhibit, AIAA 2006-0116, (Reno, NV), January 2006.

[75] Y. Fang and S. Menon, "Kinetic-Eddy Simulation of Static and Dynamic Stall," in 24^{th} AIAA Applied Aerodynamics Conference, AIAA 2006-3847, (San Francisco, CA), June 2006.

[76] Chen, K. and Thyson, N., "Extension of Emmons' Spot Theory to Flows on Blunt Bodies," *AIAA Journal*, vol. 9, no. 5, pp. 821–825, 1971.

[77] Cebeci, T., "Essential Ingredients of a Method for Low Reynolds-Number Airfoils," *AIAA Journal*, vol. 27, no. 12, pp. 1680–1688, 1988.

[78] Ekaterinaris, J., Chandresakhara, M. and Platzer, M., "Analysis of Low Reynolds Number Airfoil Flows," *Journal of Aircraft*, vol. 32, no. 3, pp. 625–630, 1995.

[79] Johansen, J., "Prediction of Laminar/Turbulent Transition in Airfoil Flows," RIS-R-987, Riso National Laboratory, Roskilde, Denmark, May 1997.

[80] Gregory, N. and O'Reilly, C., "Low-Speed Aerodynamic Characteristics of NACA0012 Aerofoil Section, Including the Effects of Upper-Surface Roughness Simulating Hoar Frost," 3726, NPL Aeronautics Division, 1970.

[81] McCroskey, W., McAlister, K., Carr, L. and Pucci, S., "An Experimental Study of Dynamic Stall on Advanced Airfoil Sections Volume 1. Summary of the Experiment," TM-84245, NASA, 1982.

[82] Duraisamy, K., McCroskey, W., and Baeder, J., "Analysis of Wind Tunnel Wall Interference Effects on Subsonic Unsteady Airfoil Flows," *Journal of Aircraft*, vol. 44, no. 5, pp. 1683–1690, 2007.

[83] Smith, M., Koukol, B., Quackenbush, T. and Wachspress, D., "Reverse- and Cross-Flow Aerodynamics for High-Advance-Ratio Flight," in 35^{th} European Rotorcraft Forum 2009, vol. 1, (Hamburg, Germany), pp. 392–412, 2009.

[84] Smith, M. J., Wong, T.-C., Potsdam, M., Baeder, J., and Phansee, S., "Evaluation of CFD to Determine Two-Dimensional Airfoil Characteristics for Rotorcraft Applications," *Journal of the American Helicopter Society*, vol. 50, no. 1, pp. 110–119, January 2006.

[85] Mouton, M. A. and Smith, M. J., "The Prediction and Validation of Static and Dynamic Stall," in presented at Heli Japan 2010, Paper T221, November 2010.

[86] Mahmoudnejad, N. and Hoffmann, K., "Numerical Investigation of Unsteady Turbulent Flows over Cavities," in 27^{th} AIAA Applied Aerodynamics Conference, AIAA 2009-3503, (San Antonio, TX), June 2009.

[87] Rossiter, J., "Wind-Tunnel Experiments on the Flow over Rectangular Cavities at Subsonic and Transonic Speeds. Reports and Memoranda 3438," RAE 64037, Aeronautical Research Council, 1964.

[88] Chung, K., "Transonic Cavity-Convex Corner Interaction," *Journal of Aircraft*, vol. 40, no. 6, pp. 1131–1136, 2003.

[89] Burg, J., "Maximum Entropy Spectral Analysis," in Proceedings of the 37^{th} Meeting of the Society of Exploration Geophysicists, (Oklahoma City, OK), 1967.

[90] Burg, J., "A New Analysis Technique for Time Series Data," in Modern Spectrum Analysis (Childers, D., ed.), pp. 42–48, New York, NY: IEEE Press, 1978.

[91] Huang, L. and Ho, C., "Small-Scale Transition in a Plane Mixing Layer," *Journal of Fluid Mechanics*, vol. 210, no. 1, pp. 475–500, 1990.

[92] Larcheveque, L., Sagaut, P., Le, T. and Comte, P., "Large-Eddy Simulation of a Compressible Flow in a Three-Dimensional Open Cavity at High Reynolds Number," *Journal of Fluid Mechanics*, vol. 516, no. 1, pp. 265–301, 2004.

[93] Tam, C., Orkwis, P. and Disimile, P., "Comparison of Baldwin-Lomax Turbulence Models for Two-Dimensional Open Cavity Computations," *AIAA Journal*, vol. 34, no. 3, pp. 629–631, 1996.

[94] Krzysiak, A., "Experimental and Numerical Investigation of Dynamic Stall on Helicopter Airfoils with Influence of Icing Effect," 51/BA/01/P, Warsaw Institute of Aviation, Praha, Czech Republic, December 2001.

[95] Benetka, J., Kladrubsky, M. and Valenta, R., "Mereni Profilu NACA 0012 ve Stebinovem Mericim Prostoru," VZLU R-2909/98, Aeronautical Research and Tests Institute, Praha, Czech Republic, April 1998.

[96] Carr, L., McAlister, K. and McCroskey, W., "Analysis of Development of Dynamic Stall Based on Oscillating Airfoil Experiments," NASA TN D-8382, NASA, January 1977.

[97] Shen, J., Chopra, I., and Johnson, W., "Performance of Swashplateless Helicopter Rotor with Trailing-Edge Flaps for Primary Flight Control," *Journal of the American Helicopter Society*, vol. 55, no. 4, pp. 42005–1–42005–9, October 2010.

[98] Liggett, N. and Smith, M., "The Physics of Modeling Unsteady Flaps with Gaps," *Journal of Fluids and Structures*. submitted June 2012, under peer review.

[99] Liggett, N. and Smith, M., "A Study of the Gap Physics of Airfoils with Unsteady Flaps," *AIAA Journal of Aircraft*. submitted July 2012, under peer review.

[100] Rumsey, C., "Time-Dependent Navier-Stokes Computations of Separated Flows Over Airfoils," in 18^{th} Fluid Dynamics and Plasmadynamics and Lasers Conference, AIAA 1985-1684, (Cincinnati, OH), July 1985.

CHAPTER XI

VITA

Nicholas Liggett was born in Atlanta, Georgia in 1980, and lived there throughout his primary and secondary education. He has always had an interest in the aerospace disciplines, particularly fluid dynamics and propulsion, and attended the Georgia Governor's Honors Program for mathematics during high school. Nicholas received individual undergraduate degrees with honors in aerospace engineering and mechanical engineering in 2004 and a Masters degree in aerospace engineering in 2006 from the Georgia Institute of Technology. He also earned a Doctor of Philosophy in aerospace engineering from the Georgia Institute of Technology in 2012. During undergraduate and graduate school, Nicholas periodically traveled throughout Japan where he met Rina Iwai. They married in 2010 while Nicholas was working on his doctoral thesis. After graduate school, Nicholas accepted a position at Space Exploration Technologies and moved to Los Angeles, California.